Long-range-transported Saharan air layers and their radiative effects determined by airborne lidar measurements

Manuel Gutleben

München 2020

Long-range-transported Saharan air layers and their radiative effects determined by airborne lidar measurements

Manuel Gutleben

Dissertation
an der Fakultät für Physik
der Ludwig–Maximilians–Universität
München

vorgelegt von
Manuel Gutleben
aus Innsbruck, Österreich

München, den 11.09.2020

Erstgutachter: Prof. Dr. Bernhard Mayer
Zweitgutachter: Prof. Dr. Markus Rapp
Tag der mündlichen Prüfung: 19.10.2020

Zusammenfassung

Eine Hauptkomponente des atmosphärischen Aerosols sind luftgetragene Staubpartikel aus der Sahara. Saharastaub wird häufig mit den Passatwinden über den subtopischen Atlantischen Ozean transportiert. Dies erfolgt meist in abgehobenen Schichten, den sogenannten Saharan Air Layers (SALs). Auf dem Weg über den Atlantik beinflussen diese Staubschichten das Strahlungsbudget der Erde. Das geschieht einerseits durch Streuung, Absorption und Emission von Strahlung, und andererseits durch die Interaktionen von Staubpartikeln mit Wolken aufgrund der damit verbundenen Veränderungen von Wolkeneigenschaften. Obwohl diese Prozesse bekannt sind, fehlt fundiertes Wissen über die Charakteristika weit-transportierter SALs. So ist nur wenig über ihre Strahlungseffekte bekannt. Auch ihre Einflüsse auf die atmosphärische Stabilität und die damit verbundene Wolkenbildung sind wenig quantifiziert.

In dieser Arbeit werden Lidarmessungen die während der Feldkampagne mit dem Namen Next-generation Aircraft Remote-Sensing for Validation Studies II (NARVAL-II) im August 2016 durchgeführt wurden mit Hinblick auf diese Einflüsse analysiert. Dabei werden typische Eigenschaften von SALs (i.e. optische Charakteristika von Aerosolen und Wasserdampfprofile) mithilfe des flugzeuggetragenen Lidar-Systems WALES (Water vapor Lidar Experiment in Space) in der Nähe von Barbados untersucht. Das Hauptergebnis dieser Untersuchung stellen Beobachtungen von vergleichsweise hohen Wasserdampfkonzentrationen in SALs im Vergleich zu den umgebenden Luftmassen dar ($\sim$4 g kg^{-1}). Diese erhöhten Konzentrationen können bis in die Sahara zurückverfolgt werden. Es kann deshalb angenommen werden, dass die beobachteten SALs schon am Ursprung ihres Transports befeuchtet wurden.

Um die Strahlungseinflüsse von Staubaerosolen und Wasserdampf in weit-transportierten SALs zu bestimmen, werden die Lidar-Datensätze als Eingangsparameter für Strahlungstransportrechnungen verwendet. Der maximale kurzwellige Strahlungseffekt von Staubpartikeln in den beobacheten SALs liegt bei -40 W m^{-2} an der Erdoberfläche und bei -25 W m^{-2} an der Oberkante der Atmosphäre. Auch zeigt eine Analyse von drei Fallstudien, dass der Großteil des Einflusses auf die Erwärmungsraten durch Wasserdampf und nicht durch Staubaerosol verursacht wird. Wenn man nur die Strahlungseigenschaften der Saharastaubpartikel in den Berechnungen berücksichtigt, befinden sich die maximalen kurzwelligen Erwärmungsraten und langwelligen Kühlraten mitten in den SALs an den Stellen der höchsten Partikelkonzentration (kurzwellig: $+$0.5 K d^{-1}, langwellig: -0.2 K d^{-1}, netto: $+$0.3 K d^{-1}). Bei Einbeziehung der gemessenen Wasserdampfprofile verschieben sich die berechneten Maxima an die Oberkanten der SALs (kurzwellig: $+$2.2 K d^{-1}, langwellig: -6.0 bis -7.0 K d^{-1}, netto: -4.0 bis -5.0 K d^{-1}).

Aufgrund der langwelligen Abstrahlung des Wasserdampfes nehmen die Kühlraten in den SALs mit der Höhe zu. Dies destabilisiert die SALs und wirkt sich bestärkend auf Mischungsprozesse aus. Diese Erkenntnis kann zum ersten Mal direkt erklären weshalb größere Saharastaubpartikel (Durchmesser: $>7\,\mu$m) den Transport über den Atlantik überstehen und diese nicht schon während des Transportes durch gravitationsbedingte Sedimentationsprozesse zu Grunde fallen.

Ein weiterer Effekt ist, dass die langwellige Gegenstrahlung der SALs die Kühlrate der marinen Grenzschicht reduziert - sie wirkt deshalb auf die Wolkenbildung unterdrückend. Um diesen Umstand genauer zu untersuchen, werden abgeleitete makrophysikalische Wolkeneigenschaften aus Lidarmessungen in staubbelasteten und staubfreien Messregionen miteinander verglichen. Um zusätzlich mögliche saisonale Unterschiede zu identifizieren, wird auch der Lidardatensatz der Next-generation Aircraft Remote-Sensing for Validation Studies I (NARVAL-I) im Dezember 2013 analysiert. Dieser wurde über komplett staubfreien Passatwindregionen nahe Barbados aufgenommen. Die abgeleiteten Wolkenoberkantenverteilungen während NARVAL-II zeigen, dass in staubbelasteten Messregionen niedrigere Wolken als in staubfreien Messregionen vorkamen. Auch eine gewisse Saisonalität ist erkennbar. Während sich im Sommer 2016 die meisten Wolkenoberkanten zwischen 0.5 und 1.0 km befanden, konnten im Winter 2013 die meisten Wolkenoberkanten in Höhen zwischen 2.0 und 2.5 km detektiert werden. Außerdem herrschten in staubbelasteten Messregionen horizontal kürzere Wolken als in staubfreien Messregionen vor. Der abgeleitete Bedeckungsgrad beläuft sich auf 14 % in staubbelasteten Gebieten. In den beobachteten staubfreien Gebieten sind die Bedeckungsgrade wesentlich höher: 31 % (Sommer), 37 % (Winter).

Abstract

Saharan mineral dust particles are one of the main constituents of the atmosphere's primary aerosol load. They get frequently transported over the subtropical North Atlantic Ocean in elevated layers, termed Saharan Air Layers (SALs). It is known that SALs impact the Earth's radiation budget by scattering, absorbing and emitting radiation as well as by modifying cloud microphysical properties. However, profound knowledge of characteristics and radiative properties of long-range-transported SALs as well as of impacts which they have on atmospheric stability and the development of clouds, is missing so far.

In this thesis, airborne lidar data collected during the field campaign Next-generation Aircraft Remote-Sensing for Validation Studies II (NARVAL-II) in August 2016 is analyzed and used to address this issue. Typical characteristics of long-range-transported SALs (i.e. optical properties of aerosol particles and vertical profiles of water vapor concentrations) are investigated on the basis of measurements by the airborne lidar system WALES (Water vapor Lidar Experiment in Space) in the vicinity of Barbados. The main finding of this investigation is an increased amount of water vapor in the dust layers compared to the surrounding dry free atmosphere ($\sim$4 g kg^{-1}). It is found that these enhanced concentrations can be retraced to the origins of transport in the central Sahara. This finding is suggesting that the observed SALs already got moistened in the course of dust mobilization processes.

To study the radiative impacts of both mineral dust aerosol particles and observed enhanced water vapor concentrations inside SALs, measured lidar data sets are used as input for radiative transfer calculations of SAL-radiative effects and atmospheric heating rates. The overall short-wave radiative effect of mineral dust particles in SALs has maximum magnitude of -40 W m^{-2} at surface level and -25 W m^{-2} at the top of the atmosphere. An analysis based on three case studies reveals that the observed enhanced amounts of water vapor within SALs have a much stronger impact on heating rate calculations than mineral dust aerosol. Maximum mineral dust short-wave heating and long-wave cooling rates are found at the center of the SALs where dust concentrations are highest (short-wave: $+$0.5 K d^{-1}, long-wave: -0.2 K d^{-1}, net: $+$0.3 K d^{-1}). However, when considering both aerosol concentrations and measured water vapor mixing ratios in radiative transfer calculations, the maximum heating/cooling rates shift to the top of the dust layer (short-wave: $+$2.2 K d^{-1}, long-wave: -6.0 to -7.0 K d^{-1}, net: -4.0 to -5.0 K d^{-1}).

As a consequence of water vapor radiative cooling, calculated net-heating rates inside SALs decrease with height. It results in a destabilization of the dust layers and a consequent

promotion of vertical mixing processes. This finding can for the first time explain why super-micron particles with diameters greater than 7 μm remain inside the SALs during transport and are not removed from the layers by means of Stokes gravitational settling.

Furthermore, long-wave counter radiation of SALs is found to reduce cooling at the tops of the subjacent marine boundary layers. Consequently, less convective mixing processes can occur and cloud development might get suppressed. To investigate whether this is the case, a comparison of lidar-derived cloud macrophysical properties in dust-laden and dust-free trade wind regimes is conducted. Lidar data collected over completely dust-free subtropical regions near Barbados during the Next-generation Aircraft Remote-Sensing for Validation Studies I (NARVAL-I) in December 2013 is additionally analyzed to identify possible seasonal differences of these properties (winter versus summer). The derived cloud top height distributions during NARVAL-II indicate that shallower clouds have been present in the dust-laden trades compared to dust-free summer trades. Additionally, a clear seasonality can be identified. While during the summer season most cloud tops were observed in altitudes ranging from 0.5 to 1.0 km, most cloud tops in winter season were identified between 2.0 and 2.5 km altitude. Moreover, it is found that regions comprising elevated SALs showed a larger fraction of horizontally small clouds compared to dust-free regions. The cloud fraction in the observed dust-laden summer trades is 14 %. In the dust-free trades the cloud fraction is significantly higher: 31 % (summer) and 37 % (winter).

Publications

Parts of the results presented in this thesis have been published in the following peer-reviewed articles:

2019

- **Cloud macro-physical properties in Saharan-dust-laden and dust-free North Atlantic trade wind regimes: a lidar case study**,
  Gutleben Manuel, Groß Silke, and Wirth Martin,
  Atmos. Chem. Phys., 19, 10659-10673, doi: 10.5194/acp-19-10659-2019.

- **Impacts of water vapor on Saharan air layer radiative heating**,
  Gutleben Manuel, Groß Silke, Wirth Martin, Emde Claudia and Mayer Bernhard,
  Geophys. Res. Lett., 46(14), 14854-14862, doi: 10.1029/2019GL085344.

- **Investigating the liquid water path over the tropical Atlantic with synergistic airborne measurements**,
  Jacob Marek, Ament Felix, *Gutleben Manuel*, Konow Heike, Mech Mario, Wirth Martin, and Crewell Susanne,
  Atmos. Meas. Tech., 12, 3237-3254, doi: 10.5194/amt-12-3237-2019.

2020

- **Radiative effects of long-range-transported Saharan air layers as determined from airborne lidar measurements**,
  Gutleben Manuel, Groß Silke, Wirth Martin, and Mayer Bernhard,
  Atmos. Chem. Phys., 20, 12313–12327, doi: 10.5194/acp-20-12313-2020.

Parts of the results shown in this thesis are presented in articles that are currently under review for publication:

- **Synergy of active- and passive remote sensing: an approach to reconstruct three-dimensional cloud macro- and microphysics**,
  Höppler Lucas, Gödde Felix, *Gutleben Manuel*, Kölling Tobias, Mayer Bernhard, and Zinner Tobias,
  Atmos. Meas. Tech. Discuss., doi: 10.5194/amt-2020-49.

- **EUREC^{4}A**,
  Stevens B., and Coauthors (*Gutleben M.*),
  Earth Syst. Sci. Data Discuss., doi: 10.5194/essd-2021-18.

Contents

Chapter 1

Introduction

In the year 2019 the average temperature across the Earth's land and ocean surfaces was on average 0.95°C higher than the average temperature of the 20th century (*NOAA National Centers for Environmental Information*, 2020). This marks the second highest average surface temperature in the period from 1880 to 2019 after the record-setting year 2016. Changes in surface temperatures are closely linked to changes in radiative forcings, which govern the ratio of incoming short-wave solar radiation to outgoing long-wave thermal radiation. Outgoing terrestrial radiation gets absorbed in the atmosphere by aerosols, clouds and greenhouse gases (e.g. H_2O, CO_2 or CH_4). Any increase of the atmospheric greenhouse gas concentration (e.g. due to increasing anthropogenic emissions) is consequently leading to a warming of the atmosphere and higher surface temperatures. Whereas greenhouse gases mainly contribute to the reduction of outgoing thermal radiation, atmospheric aerosols can influence both the flux of outgoing thermal radiation and the flux of incoming solar radiation (i.e. by scattering and absorption). Thus, they can either have a warming or a cooling effect.

Aerosol particles are ubiquitous in the troposphere and their size ranges from a few nanometers to several micrometers. They can be classified as primary or secondary particles. Primary aerosols are particles that are directly injected into the atmosphere, i.e. by wind-driven suspension (e.g. sea spray, mineral dust, pollen or spores), by natural and anthropogenic biomass burning or fossil fuel combustion (e.g. carbonaceous particles like black carbon) and via volcanic eruptions (e.g. sulfates). Secondary aerosols are formed from the gas-to particle-conversion of volatile organic compounds or from gaseous precursors via chemical reactions, e.g. SO_2, H_2S, NO_x.

Once injected into the atmosphere, aerosols can be transported over long distances. For this reason, aerosol particles can be found almost all around the globe (Figure 1.1). Prominent examples for long-range aerosol transport are for instance the perpetual transport of Saharan dust across the Atlantic Ocean or the transport of volcanic particles to Europe following the eruptions of the Icelandic Eyjafjallajökull volcano in 2010 (which led to a partial shut-down of European air traffic). These examples illustrate that aerosols impact the Earth's climate and radiation budget not only at source regions, but also very far away of them.

Despite of the fact, that over the past decades climate science became one of the main

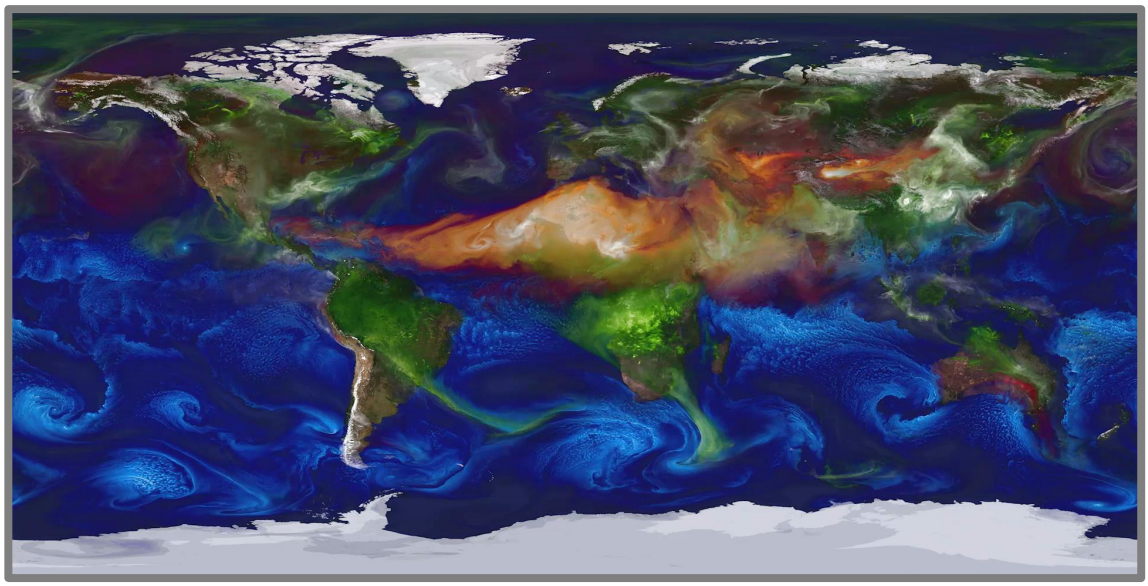

Figure 1.1: GEOS-5[2]/GOCART[3] simulation of the global distribution of mineral dust (orange), soot and smoke from biomass burning (green) sea spray (blue) and sulfates of volcanic or anthropogenic origin (white). (source: NASA/Goddard Space Flight Center - https://svs.gsfc.nasa.gov/30017).

fields of research in atmospheric science, aerosols and their precursors still contribute the largest uncertainty to the total radiative forcing (*IPCC*, 2013[1]; Figure 1.2). While black carbons, which are strongly absorbing aerosols, are estimated to have a positive contribution to the total aerosol radiative forcing, other aerosol types like sulfates, nitrates or mineral dust particles are expected to have a negative contribution. However, the uncertainty of these estimates is large enough that up to now it is still not completely certain whether the overall aerosol radiative forcing due to radiation interactions has a negative or positive sign (IPCC estimate: -0.45 [-0.95 to +0.05] $\mathrm{W\,m^{-2}}$). In addition to that, also the radiative forcing of cloud adjustments due to aerosols is ill quantified and shows an even larger uncertainty than the aerosol radiative forcing itself (IPCC estimate: -0.45 [-1.2 to 0.0] $\mathrm{W\,m^{-2}}$).

One of the main contributors to the uncertainty in aerosol radiative forcing is mineral dust aerosol. The IPCC estimates the mineral dust radiative forcing to be slightly negative. However, the uncertainty of the estimation is so high that even net positive values can not be completely excluded (-0.1 [-0.3 to +0.1] $\mathrm{W\,m^{-2}}$). Such large uncertainties arise from the

[1] Intergovernmental Panel on Climate Change
[2] NASA Goddard Earth Observing System Model-5
[3] Goddard Chemistry Aerosol Radiation and Transport Model

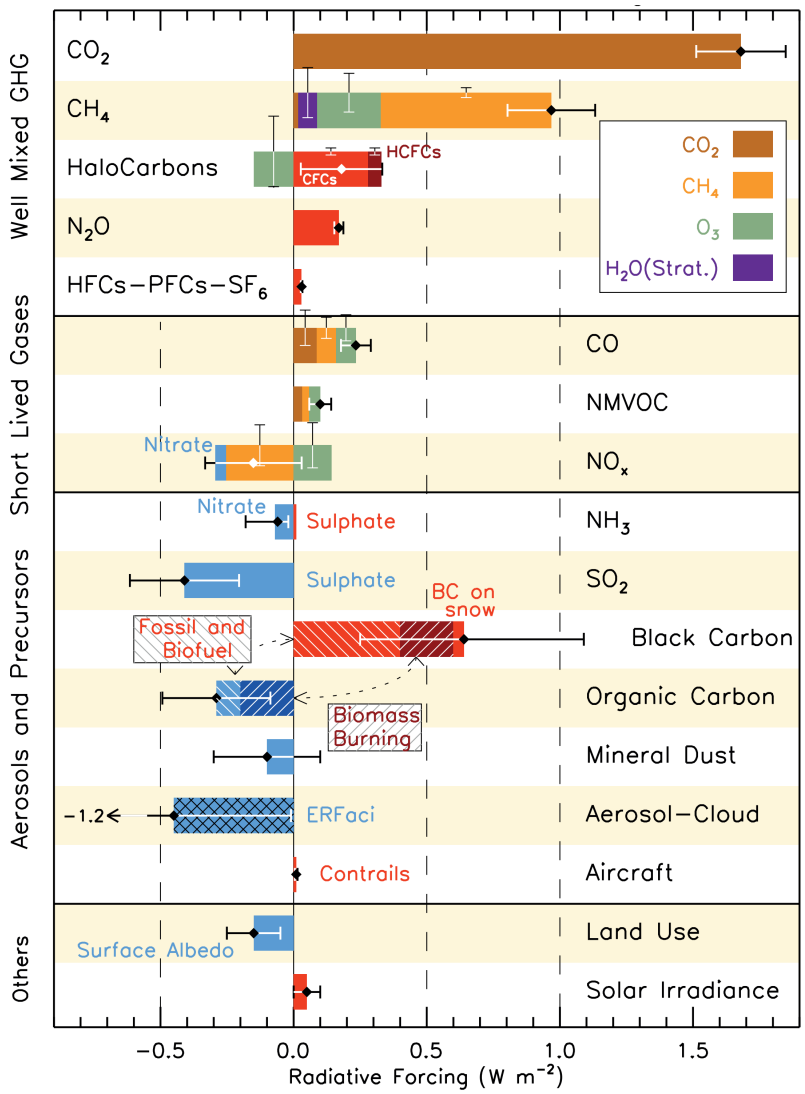

Figure 1.2: Radiative forcing estimates for the period 1750-2011 based on emitted compounds (gases, aerosols or aerosol precursors) and other changes. Diamond symbols indicate the net individual contributions. Bars mark the respective uncertainties (5 to 95 % confidence range). Red (positive forcing) and blue (negative forcing) colors are used for emitted components which affect few forcing agents, whereas several colors are used for emitted components affecting many compounds. Vertical bars indicate the relative uncertainty of the radiative forcing induced by each component. Their length is proportional to the thickness of the bar such that the full length would be equal to the bar thickness for a ±50 % uncertainty. The abbreviations NVOC and ERFaci represent non-methane volatile compounds and the effective radiative forcing due to aerosol-cloud interactions. Adapted from *IPCC* (2013).

lack of understanding regarding impacts that mineral dust aerosols have on global climate. Attributes like their spatial distribution, their chemical composition, their shape or their ability to modify the occurrence and lifetime of clouds have to be better understood to minimize these uncertainties (see Section 1.2).

1.1 Mineral dust aerosol and its long-range transatlantic transport

Mineral dust aerosols are eroded soil particles that are suspended into the atmosphere by reason of strong surface winds and mechanical processes. They are mainly generated via disaggregation of larger particles following saltation and creeping, particularly in arid regions with little vegetation (e.g. *Zhao et al.*, 2006). After being entrained into the atmosphere, the dust particles can be transported over long distances, e.g. from Asia towards Europe (*Grousset et al.*, 2003) or from North Africa towards the Americas (*Prospero and Carlson*, 1972) and Europe (*Ansmann et al.*, 2003). This is why mineral dust is representing one of the main contributors to the global aerosol loading and is estimated to contribute between 25% to 30 % to the Earth's total aerosol optical depth (*Tegen et al.*, 1997; *Kinne et al.*, 2006). Estimated global annual dust emissions from model calculations range from 1000 to 4000 Tg a^{-1} (*Huneeus et al.*, 2011). Although emissions of sea salt exceed those emissions, mineral dust is generally known as the main contributor to the atmospheric aerosol mass burden (*Cakmur et al.*, 2006). This paradox can be explained by shorter atmospheric residence times of sea salt due to more effective removal processes (*Textor et al.*, 2006).

An analysis of ice cores has revealed that the global dust burden has been significantly larger in the past than in the present (*Fischer et al.*, 2007). In future, dust emission rates will presumably differ as well. Modifications of vegetation and soil patterns as a consequence of climate change and land use will likely lead to different magnitudes of dust emissions. However, up to now, it is not clear whether these changes in emission will be stronger or weaker so that the future climate impact of aeolian mineral dust still remains unclear (*Woodward et al.*, 2005; *Mahowald et al.*, 2006).

Aeolian dust particles can either be generated naturally or anthropogenically. Natural emission is predominating on global scale. However, recent satellite observations have indicated that anthropogenic contributions (e.g. land use and road dust) to the total global dust emissions could be as high as 20 % to 25 % (*Ginoux et al.*, 2012). Most of the Earth's natural dust sources can be found in the Northern Hemisphere inside a so-called dust-belt (*Prospero*, 2002) which extends from North Africa to China. It comprises several deserts, e.g. the Saharan Desert, the Arabian Desert, the Gobi Desert or the Taklamakan Desert.

The Sahara, which extends over approximately $9 \cdot 10^5$ km^2, is not only the planet's greatest desert but also its greatest dust source. From an intercomparison of a total of 15 global aerosol models *Huneeus et al.* (2011) estimate nowadays dust emission of North Africa to range from 400 to 2200 Tg a^{-1} (which would approximately equal to 8-44 times the water volume of Lake Constance). They also estimate that North African dust emissions contribute approximately

50 % to the Earth's total dust emissions. Asia and the Middle East follow with 10 % each.

Especially in the northern hemispheric summer months from June to August, strong surface heating over North Africa is causing a pronounced thermal low pressure system, known as the Saharan Heat Low (SHL). The SHL comes along with a deep and well-mixed planetary boundary layer, the so-called Saharan Atmospheric Boundary Layer (SABL), which is often observed to reach from surface up to 6 km altitude ($\sim$ 500 hPa) (e.g. *Messager et al.*, 2009). Mobilization processes like low-level nocturnal jets or convective activity (*Schepanski et al.*, 2009) can mix Saharan dust particles into the SABL. In this way deep-reaching dust layers, which can cover the whole vertical extent of the SABL, are formed.

Saharan mineral dust layers can be transported far away from their origin. Transportation routes depend on the large-scale synoptic situation as well as the location of mobilization and can lead over the Mediterranean Sea towards Central and Eastern Europe (e.g. *Ansmann et al.*, 2003; *Papayannis et al.*, 2008; *Wiegner et al.*, 2011) or over the Atlantic Ocean to the Amazon region, the Caribbean and North America (e.g. *Prospero and Carlson*, 1972; *Jickells*, 2005; *Prospero et al.*, 2010). Only 15 % of the total emitted dust load is transported north- and eastwards towards the Mediterranean and the Middle East (e.g. *Shao et al.*, 2011). Almost 85 % of the total emitted dust is transported south- and westwards towards the Sahel, the Gulf of Guinea and the Atlantic Ocean.

An easterly flow, termed the African Easterly Jet (AEJ) is prevailing over North Africa (15° - 20° N) in the months from June to October and plays a major role for westward North African dust transport as it advects dust-laden air masses from the Saharan desert towards the Atlantic Ocean. The AEJ is a thermal wind that is generated by strong differences in surface temperature and moisture between the dry and hot SHL and the cool and moist Gulf of Guinea in the South. *Cook* (1999) showed that soil moisture gradients between the Sahara and equatorial Africa are additionally necessary for the formation and maintenance of the AEJ. Barotropic and baroclinic instabilities as well as atmospheric convection cause subtropical disturbances of the AEJ, termed African Easterly Waves (AEWs). Those AEWs can modulate Saharan dust outbreaks in a way that transatlantic dust transport can sometimes be observed to follow wave-like patterns (*Burpee*, 1972; *Jones et al.*, 2003; *Knippertz and Todd*, 2010).

When advected dust layers arrive at the Atlantic coast, they get undercut by cooler and moister marine air and form elevated layers, so-called Saharan Air Layers (SALs; *Prospero and Carlson*, 1972; *Carlson and Prospero*, 1972). Visible as giant dust outbreaks off the West African coast, SALs can easily be detected from space (Figure 1.3). Especially in the summer months SALs remain relatively undisturbed and can be transported over thousands of kilometers towards the Caribbean or the Americas (*Karyampudi et al.*, 1999). Thus, Saharan mineral dust layers cannot be understood as a local phenomena close to their source regions. They have an impact on the radiation budget as well as on the formation and physical properties of clouds over large areas far away from their origin.

Saharan dust transport over the Atlantic Ocean also follows the seasonal oscillation of the Intertropical Convergence Zone (ITCZ) and the AEJ (*Tsamalis et al.*, 2013; *Meng et al.*, 2017). During northern hemispheric winter dust sources in the southern Sahara and the Sahel zone are particularly active. During this season the ITCZ and the AEJ are in their southernmost

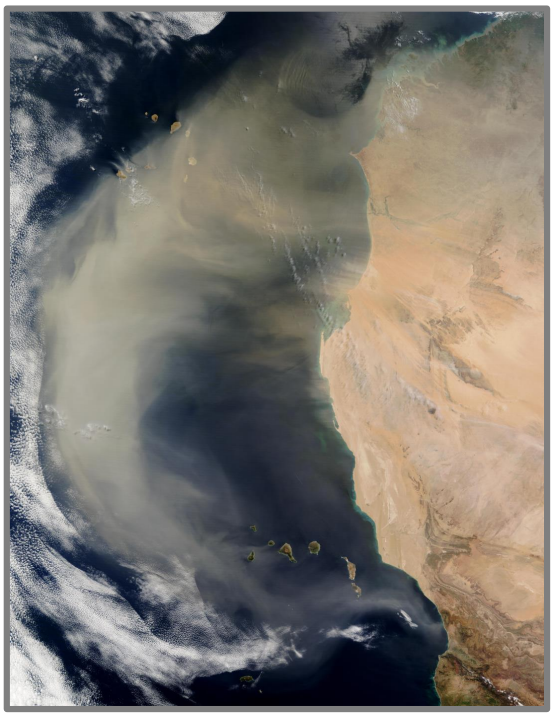

Figure 1.3: Saharan dust outbreak off the West African coast as imaged by MODIS (Moderate-resolution Imaging Spectroradiometer) aboard the Terra satellite on 2 March 2003 (source: NASA Worldview - https://worldview.earthdata.nasa.gov).

position and North African dust aerosols are primarily transported southwestwards by the north-easterly Harmattan winds. As a consequence, the main transportation route of Saharan dust particles from November to March leads over the Gulf of Guinea towards South America. However, during northern hemispheric summer, the ITCZ and the AEJ move northwards and the Sahel zone gets more vegetated. As a result, more and more dust in the northern Sahara is mobilized and gets advected westwards with easterly trade winds. Hence, the main dust transportation route from April to October leads over the Canary and Cape Verde islands towards the Caribbean and North America (see Figure 1.4).

SALs are characterized by two pronounced inversions at their top and their bottom. Both help to maintain the structure during long-range transport. While the lower inversion is caused by the strong vertical gradients of temperature between the hot SAL-base and the subjacent cooler marine air below (*Prospero and Carlson*, 1972; *Dunion and Velden*, 2004), the upper inversion forms due to the predominant large-scale subtropical subsidence in the upper troposphere (*Gamo*, 1996). During transatlantic transport the top of the SAL usually decreases by 1-2 km and the SAL base increases by several hundred meters, so that the layer thins and finally dissipates (e.g. *Adams et al.*, 2012).

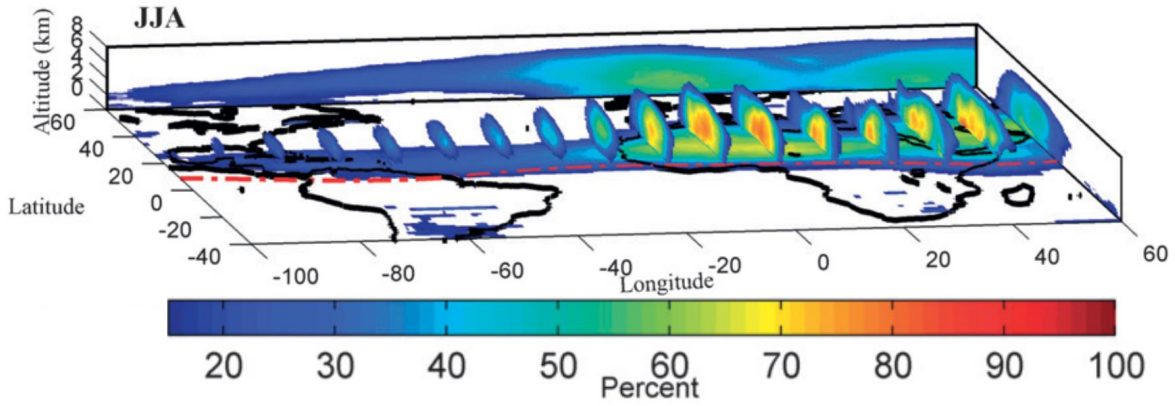

Figure 1.4: Relative frequency of mineral dust occurrence as inferred from the CALIOP (Cloud Aerosol LIdar with Orthogonal Polarization) Feature Mask algorithm in the months from June to August (JJA) and the period from 2006 to 2010. The dashed red line indicates the position of the Intertropical Convergence Zone (ITCZ). Adopted from *Adams et al.* (2012).

1.2 Impacts of transported Saharan dust layers

Saharan mineral dust particles that are transported across the Atlantic Ocean can affect the Earth's climate system in many different ways (Figure 1.5). They interact with radiation and impact the Earth's energy budget, they have an effect on cloud development and the formation of ice particles and they play an important role in the biogeochemistry of oceans and soils. Furthermore, dust particles can affect human health. The following paragraphs discuss all of these impacts. Particular attention is paid to the atmospheric and climatic impacts:

Human Health: Especially in regions of heavy dust pollution the inhalation of fine dust particles is often observed to lead to certain physiological responses including respiratory, cardiovascular and cardiopulmonary diseases or asthma (*de Longueville et al.*, 2012). Dust particles can additionally affect health by transporting dangerous pathogens like, bacteria, fungus or viruses (*Griffin*, 2007).

Biogeochemistry: Mineral dust particles play a major role in ocean and soil biogeochemistry. Due to their high iron and phosphorus content they provide important nutrients, e.g. for plankton growth and the consequent production of atmospheric oxygen (e.g. *Martin et al.*, 1991; *Jickells*, 2005) or soil fertilization (e.g. *Okin et al.*, 2008). Especially in the Amazon basin, settling long-range-transported mineral dust is an important fertilizer which promotes

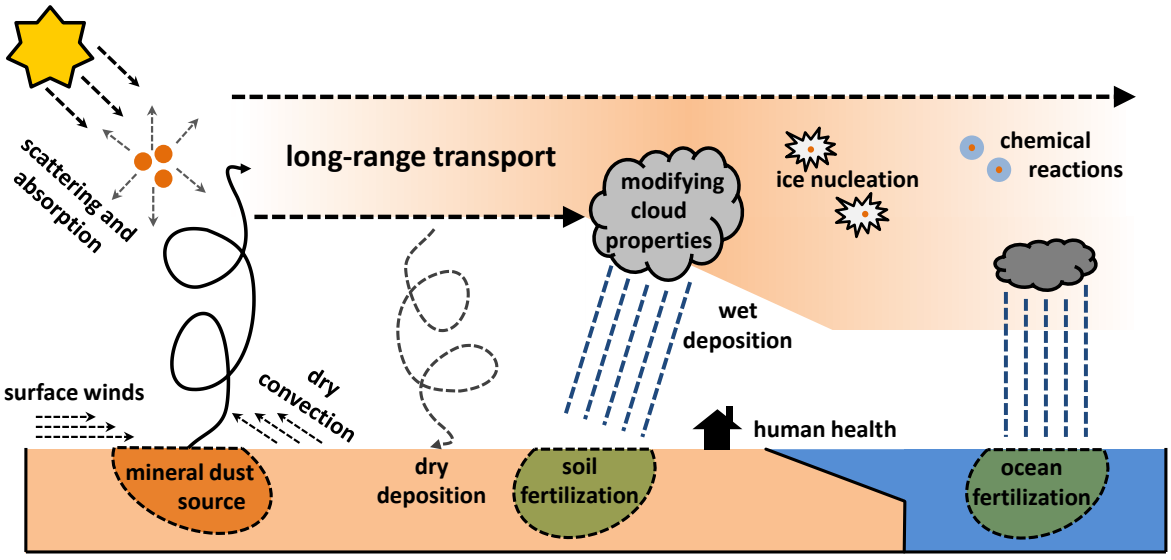

Figure 1.5: Schematic illustration of SAL-impacts on the climate system.

the growth of the rain forest. *Yu et al.* (2015) estimate annual Saharan dust deposition rates of $28 \pm 20\,\mathrm{Tg\,a^{-1}}$ and $29 \pm 21\,\mathrm{kg\,ha^{-1}\,a^{-1}}$ in the Amazon basin. In the course of heterogeneous uptake and chemical reactions, dust particles can remove reactive gases like HNO_3 or HO_2 but also SO_2 from the atmosphere (e.g. *Bian and Zender*, 2003; *Bauer and Koch*, 2005). When being deposited on snow surfaces, dust particles can also alter surface albedo and shorten the annual snow cover duration (*Painter et al.*, 2007). However, due to the lack of snow at low latitudes this effect rather applies for dust transport towards Europe and the snow-covered Alps and not for the transatlantic transport towards the Caribbean and the Amazon region.

Interaction with radiation and the modification of cloud properties: As already pointed out in the previous chapters, mineral dust particles play immense roles for the atmospheric radiation budget and cloud evolution. Like any other aerosol, SAL mineral dust particles can directly interact with radiation via scattering and absorption. On the one hand, dust particles scatter incoming solar radiation back to space, which results in less radiation reaching lower atmospheric levels (direct effect; e.g. *Biagio et al.*, 2020). Thus, SALs can have a cooling effect during daytime, which can be strong enough that even sea surface temperatures decrease (*Foltz and McPhaden*, 2008). On the other hand, dust particles absorb both solar radiation and terrestrial radiation, thus having a warming effect similar to greenhouse gases. As a consequence, atmospheric temperature and atmospheric stratification can be modified, which in turn impacts the evolution of clouds. However, this so-called semi-direct effect of transported dust aerosols is still poorly understood as only a view observational studies (which

mainly analyze data from satellites or models) have been conducted (e.g. *Amiri-Farahani et al.*, 2017).

In addition to the direct and semi-direct effect, SAL-particles can affect the occurrence and development of clouds by modifying cloud microphysical properties. These effects are termed indirect effects. SAL particles can for example act as so-called cloud condensation nuclei (CCN) - meaning that water vapor can condense at the surface of the particles and liquid droplets are formed (e.g. *Karydis et al.*, 2011; *Bègue et al.*, 2015). Sean Twomey first discovered that clouds which develop in regions with high aerosol loading show higher cloud droplet number concentrations (and thus higher short-wave albedo) than clouds that develop in aerosol-free regions. The higher cloud top albedo leads to enhanced reflection of short-wave radiation back to space and to subsequent climate cooling. Named after its discoverer, this effect is nowadays referred to as Twomey effect (*Twomey*, 1974, 1977).

The ability of particles to act as a CCN, however, depends on their size and and affinity for water uptake (hygroscopicity). Due to their chemical composition and particle size distribution, fresh Saharan mineral dust aerosol is known to be only little hygroscopic (*Kumar et al.*, 2011; *Walser*, 2017). Despite their weak hygroscopicity, recent studies have shown that under certain conditions mineral dust particles are indeed able to act as CCN. Pre-adsorbed multi-layers of water on the surfaces of dust particles can trigger CCN activity (*Sorjamaa and Laaksonen*, 2007; *Kumar et al.*, 2009; *Laaksonen*, 2015; *Hatch et al.*, 2019). Mixing-processes with hygroscopic material (e.g. ammonium sulfate) are another possibility how SALs can turn into effective reservoirs of CCN (*Walser*, 2017). However, a study by *Denjean et al.* (2015) showed that even after long-range transport to the Caribbean the hygroscopic properties of SAL-particles do not change significantly. Only minor portions of mineral dust were mixed with sulfate or chloride (13 % to 24 %) or aggregated with sea salt (3 % to 6 %). In spite of everything discussed above, many recent studies reported increased number concentrations of cloud droplets during dusty times compared to dust-free times in the Caribbean. Hence, long-range-transported SALs must play a significant role for cloud evolution across the Atlantic Ocean, but a lot of questions remain to be answered.

In addition to their ability of acting as CCN, SAL particles have also been identified to play an important role for ice formation in mixed-phase and cirrus clouds (e.g. *Ansmann et al.*, 2008; *Boose et al.*, 2016; *Twohy et al.*, 2017). Water droplets are known not to freeze instantaneously at freezing point. In a pristine atmosphere they freeze at temperatures lower than -38°C (homogeneous freezing; *Pruppacher and Klett*, 2010). Mineral dust particles, however, can act as ice nucleating particles (INPs) and are able to trigger the formation of ice crystals at higher temperatures (-10 to -35°C - heterogeneous freezing; e.g. *Hoose and Möhler*, 2012; *DeMott et al.*, 2015; *Villanueva et al.*, 2020). For example, *Seifert et al.* (2010) have shown that air masses that contain mineral dust comprise 25 % to 30 % more ice-containing clouds (cloud top temperatures from -10°C to -20°C) than dust-free air masses.

Besides the direct and indirect effect of the dust particles, the SAL itself was observed to have a suppressing effect on deep convection and tropical cyclone development. *Dunion and Velden* (2004) used Geostationary Operational Environmental Satellite (GOES) infrared imagery to study the structural and dynamical characteristics of the SAL and its influence on

North Atlantic cyclone evolution. *Wong and Dessler* (2005) used MODIS (Moderate Resolution Imaging Spectroradiometer) satellite data to study the effect of the SAL on deep convection. Both studies found a suppressing effect of the SAL on deep convection and tropical cyclone activity. *Wong and Dessler* (2005) suggest that the convection barrier increases with SAL optical depth, especially over the eastern North Atlantic Ocean. They argue that the warmer air associated with the SAL raises the lifting condensation level as well as the level of free convection and therefore increases the energetic barrier to convection. However, vertically resolved observations of suppressed marine cloudiness below long-range-transported layers of Saharan dust over the Atlantic Ocean are missing so far and the external forcing of dust on the development of clouds introduces one of the greatest uncertainties to nowadays climate predictions.

Over the past century many field campaigns contributed to a better understanding of long-range-transported SALs over the subtropical North Atlantic Ocean. For example BOMEX[1] and GATE[2] - the first two major field studies that concentrated on long-range-transported Saharan mineral dust - have already been conducted in the summers of 1969 and 1974 and provided first measurements of mineral dust concentrations and the spatial distribution of mineral dust over the Central and North Atlantic Ocean (*Prospero and Carlson*, 1972; *Polavarapu and Austin*, 1979). The most extensive measurement series in the last decades has probably been performed within the SAMUM[3] campaigns in 2006 and 2008 (*Heintzenberg*, 2009; *Ansmann et al.*, 2011) and the SALTRACE[4] mission in 2013 (*Weinzierl et al.*, 2017). Within this series of closure experiments, which included airborne and ground-based in situ and remote sensing measurements as well as modeling efforts, microphysical, optical and chemical properties of the SAL were investigated at the beginning of its long-range transport near the source regions (Morocco and Cape Verde) as well as after its transatlantic transport in the vicinity of Barbados (*Groß et al.*, 2015; *Haarig et al.*, 2018; *Toledano et al.*, 2019).

In situ measurements of long-range-transported Saharan dust during SALTRACE did not indicate significant changes of dust optical and microphysical properties compared to dust near source regions (*Groß et al.*, 2015). Moreover, it was found that after long-range transport SALs contain larger particles than expected from Stokes gravitational settling theory ($> 7\,\mu$m; *Weinzierl et al.*, 2017). *Gasteiger et al.* (2017) suggested that vertical mixing processes within the SALs may counteract Stokes gravitational settling during transport and facilitate an almost undisturbed transport across the Atlantic Ocean. They assumed that radiative effects may be the main driver for SAL mixing. However, previous studies with focus on Saharan dust radiative effects rather concentrated on source regions and areas at the origin of dust transport (*Kanitz et al.*, 2013; *Li et al.*, 2004; *Mallet et al.*, 2009; *Zhu et al.*, 2007). As a consequence,

[1] Barbados Oceanographic and Meteorological Experiment
[2] GARP (Global Atmospheric Research Program) Atlantic Tropical Experiment
[3] Saharan Mineral Dust Experiments, Morocco and Cape Verde
[4] Saharan Aerosol Long-range Transport and Aerosol-Cloud-Interaction Experiment

profound understanding on radiative transfer in long-range-transported SALs is missing so far and radiatively driven mixing processes in the interior of the SAL are not yet understood.

In general, model simulations suggest that after long-range transport radiative transfer calculations are very sensitive to the water vapor profile (*Wong et al.*, 2009). Especially in long-range-transported SAL regimes a correct parametrization of the water vapor profile in radiative transfer models would therefore be of high importance, since SALs were found to take up moisture over the Saharan desert (*Marsham et al.*, 2008) which often gets further transported across the Atlantic Ocean (*Jung et al.*, 2013). However, studies focusing on radiative heating rate calculations, which employ simultaneous measurements of water vapor and aerosol profiles, have not yet been performed. Prior studies lack water vapor measurements and had to take its vertical distribution from model simulations or standard atmospheric profiles.

This thesis focuses on data collected in the framework of the NARVAL-II[1] research campaign near the Caribbean island of Barbados in August 2016 (see Section 2.3). During NARVAL-II airborne remote sensing measurements over long-range-transported SALs were carried out. The remote sensing payload allowed for simultaneous measurements of aerosol optical properties and water vapor. Therefore, it enables a detailed investigation of SAL properties and of the role that water vapor potentially plays on radiation, particle mixing, atmospheric stability and the evolution of clouds.

1.3 Lidar for the investigation of transported Saharan mineral dust

The previous section highlighted the need for a better understanding of the radiative impacts of long-range-transported SALs on cloud development and particle mixing. Lidar (light detection and ranging) systems represent one of the most suitable systems to close these gaps in knowledge. They facilitate measurements of both dust and cloud properties and enable the observation of their spatial distribution. The main advantage of lidar is the possibility of measurements with high spatial resolution in the vertical, which enables simultaneous observations of SALs and clouds in one single vertical lidar profile.

In contrast to passive techniques for cloud and aerosol remote sensing (e.g. sun photometers or imagers), lidar technique provides direct measurements of aerosol optical properties. With passive remote sensing techniques it is not possible to measure aerosol optical properties directly, but retrievals from measured quantities with certain assumptions have to be applied. Especially, advanced lidar techniques like High Spectral Resolution Lidar (HSRL) or Raman lidar facilitate direct measurements of particle extinction coefficients (α_p) and aerosol optical depth (τ) without the need for any assumptions (see Chapter 2). Polarization-sensitive lidar systems additionally provide measurements of the linear particle depolarization ratio, δ_p - a key quantity for the differentiation of different aerosol species along the lidar beam (*Burton et al.*, 2012; *Groß et al.*, 2013).

[1] Next-generation Aircraft Remote sensing for VALidation studies-II (*Stevens et al.*, 2019)

The installation of lidar instruments on moving platforms, like satellites, ships or aircraft, enables additional spatial coverage and allows measurements at remote locations all around the globe. Spaceborne lidar systems, like CALIOP (Cloud Aerosol LIdar with Orthogonal Polarization; *Winker et al.*, 2010), follow a fixed orbit and are thus limited in spatial flexibility. This drawback can be avoided by mounting lidar instruments on aircraft which are capable of flying long ranges and which have great ceiling altitudes. In this way, highly resolved measurements over large areas and remote locations around the globe can be conducted in the course of just one single research flight. This is why airborne lidar instruments are valuable tools for the investigation of clouds and long-range-transported Saharan dust layers over the western subtropical North Atlantic Ocean.

1.4 Thesis objective and outline

The objective of this work is to characterize long-range-transported SALs with regard to their optical and meteorological characteristics as well as their radiative effects. Therefore, airborne lidar measurements over long-range-transported SALs are investigated with the aim to characterize their properties and to quantify their impacts on atmospheric heating and the radiation budget at surface level and top of the atmosphere. Measurements of the polarization-sensitive airborne lidar system WALES (from WAter vapor Lidar Experiment in Space; *Wirth et al.*, 2009) during the NARVAL-II field campaign (*Stevens et al.*, 2019) in the Caribbean are analyzed and used for radiative transfer calculations with the software package libRadtran (library for Radiative transfer; *Mayer and Kylling*, 2005; *Emde et al.*, 2016).

Using this approach, this work aims at answering the following research questions:

(R1) What are typical optical and meteorological characteristics of long-range-transported SALs?

(R2) What are the radiative effects of long-range-transported SALs?

The posed questions raise further reaching research questions, which shall also be addressed and discussed in this work:

(R3) How can SAL-radiative properties impact atmospheric stability?

(R4) Do SALs have an effect on shallow marine cloud occurrence and cloud macrophysical properties (i.e. cloud top heights, cloud lengths and cloud gap lengths)?

The lidar technique, its physical background and different types of atmospheric lidar systems are described in Section 2.1 The airborne lidar system WALES, which combines many of the described techniques is introduced in Section 2.2. In Section 2.3 the aims and goals as well as an overview of all conducted research flights and the aircraft setup during the NARVAL-II field campaign are presented. The lidar-based setup of the conducted radiative transfer calculations and a description of the used radiative transfer model are introduced in Section 2.4.

Chapter 3 starts with an analysis of the characteristics of observed SALs (Section 3.1.1 & Section 3.1.2) and discusses their optical and meteorological properties by means of a detailed analysis of dropsondes and lidar measurements during RF6 (Section 3.1.3). The chapter continues with results of radiative transfer calculations that were conducted for three representative case studies during NARVAL-II in Section 3.2. Results from radiative heating calculations of long-range-transported SALs are presented (Section 3.2.2) and the dust-radiative effects of transported SALs are quantified (Section 3.2.3).

Chapter 4 discusses the impacts of SAL radiative properties on SAL-stratification, the MBL and the evolution of convection (Section 4.1.1 & Section 4.1.2). Furthermore, differences of cloud macrophysical properties between dust-laden and dust-free trade wind regimes are analyzed and discussed in Section 4.2.

The thesis concludes with a roundup of the results and an identification of open research questions which should be addressed in future studies in Chapter 5.

1.5 Data sources and software routines

The heart of this work is data collected by the airborne lidar system WALES in the framework of the NARVAL-II field campaign. During NARVAL-II WALES was operated by Martin Wirth, Silke Groß, Axel Amediek and Andreas Fix. Initial data processing and a data quality analysis was performed by Martin Wirth. Backward trajectory calculations were performed using the freely available Hybrid Single Particle Lagrangian Integrated Trajectory Model (HYSPLIT; *Stein et al.*, 2015) software package with National Centers for Environmental Prediction Global Data Assimilation System (NCEP GDAS) input data. Dakar radiosonde data were obtained from the freely accessible repository of the University of Wyoming (`https://www.uwyo.edu/atsc/`). Radiative transfer calculations have been performed utilizing the libRadtran software package (*Mayer and Kylling*, 2005; *Emde et al.*, 2016) and the OPAC (Optical Properties of Aerosols and Clouds; *Hess et al.*, 1998; *Koepke et al.*, 2015) library for aerosol optical properties.

Chapter 2

Methods

This chapter starts with a description of the lidar technique and its physical background (Section 2.1). Moreover, different types of atmospheric lidar systems are presented. The airborne lidar system WALES combines many of the described techniques in one synergistic setup and is introduced in Section 2.2. The results of this work are based on airborne WALES lidar measurements during the NARVAL-II research campaign series over the subtropical North Atlantic Ocean. In Section 2.3 aims and goals as well as all research flights and the aircraft setup during NARVAL-II are introduced to the reader. Data sets obtained during this campaign are used for radiative transfer calculations. The lidar-based setup of those calculations and a description of the used radiative transfer model are presented in Section 2.4.

2.1 Lidar in atmospheric sciences

The very first approaches to use the lidar (light detection and ranging) principle for measurements in atmospheric sciences dates back to the 1930s, several decades before the invention of lasers (*Synge*, 1930; *Tuve et al.*, 1935; *Hulburt*, 1937; *Johnson et al.*, 1939). Back then and until the 1960s it was tried to derive air densities, aerosol optical properties and cloud base heights by analyzing scattered light from search light beams at scanning distant receivers (*Elterman*, 1951, 1966). Thirty years later, first laser systems - mankind's first coherent light sources (*Maiman*, 1960) - have been developed. Especially after the invention of the Q-switched or giant-pulse laser (*McClung and Hellwarth*, 1962), lidar technique in atmospheric science aroused great interest. Various atmospheric lidar systems have been engineered, e.g. for measuring trace gas concentrations, wind speeds and directions as well as for determining meteorological parameters like temperature or air density. Moreover, lidar systems became mobile instruments and depending on the research question they were mounted onto different platforms (e.g. ships, satellites, aircraft, balloons).

This is why nowadays atmospheric lidar systems are used for a broad range of applications. Ceilometer networks, for example, provide information on measured cloud base heights around the globe and help to improve operational weather forecasts. Spaceborne lidar systems like

ALADIN[1], MERLIN[2], ATLID[3] or CALIOP facilitate or will facilitate measurements of the global distribution of wind fields, clouds, aerosols and methane and help to understand the Earth's climate system. Airborne lidar systems are employed to determine boundary layer heights or the dispersion of exhaust-gas plumes to better understand effects of anthropogenic pollution. And finally, as a last example, lidar is used in aviation meteorology to detect wake vortices or turbulence and helps to make air travel safer.

2.1.1 Lidar setup and lidar equation

Since lidar is an active remote-sensing technique, a basic lidar setup consists of a transmitter and a receiver (see Figure 2.1). The main part of the transmitter is a laser system which emits short light pulses with power P_0 into the atmosphere. A frequently used type of laser for atmospheric applications is the Nd:YAG (Neodymium-doped Yttrium Aluminum Garnet; $Nd:Y_3Al_5O_{12}$) laser. It emits monochromatic light at 1064 nm. Depending on the research question the light can be frequency-doubled (532 nm) or -tripled (355 nm) using second or third harmonic generators, but also tuned to specific wavelengths using non-linear crystals.

The emitted laser beam has a certain divergence θ_t. Compared to other active remote sensing techniques like radar (radio detection and ranging) or sodar (sound detecting and ranging) where characteristic beam divergences are in the order of several degrees, θ_t of a typical atmospheric lidar is relatively small and just amounts to several μrad. Due to θ_t, P_0 of the emitted laser pulse gets evenly distributed onto a segment of a sphere and the intensity I_t at a certain distance r from the laser can be described as,

$$I_t = \frac{P_0}{\pi\, r^2\, (\frac{\theta_t}{2})^2} = \frac{4\, P_0}{\pi\, r^2\, \theta_t^2}. \tag{2.1}$$

The emitted laser pulse has a certain length τ_L and therefore illuminates a volume,

$$V = \frac{c\,\tau_L}{2}\,\pi\left(\frac{r\,\theta_t}{2}\right)^2, \tag{2.2}$$

where c is the speed of light. Parts of the received power in the illuminated volume are scattered by molecules and aerosol particles in the form of a new spherical wave towards all directions. Its power P_V can be described as,

$$P_V = \beta'\, V\, I_t = \beta'\,\frac{c\,\tau_L}{2}\,P_0. \tag{2.3}$$

Here β' is the volume scattering cross section of the illuminated volume. The part of the light which is scattered in backward direction (180°) is collected by a telescope at the lidar instrument. At the telescope the received light shows an intensity of,

[1] Atmospheric LAser Doppler INstrument (*Schillinger et al.*, 2003)
[2] MEthane Remote sensing LIdar missioN (*Ehret et al.*, 2017)
[3] ATmospheric LIDar (*Illingworth et al.*, 2015)

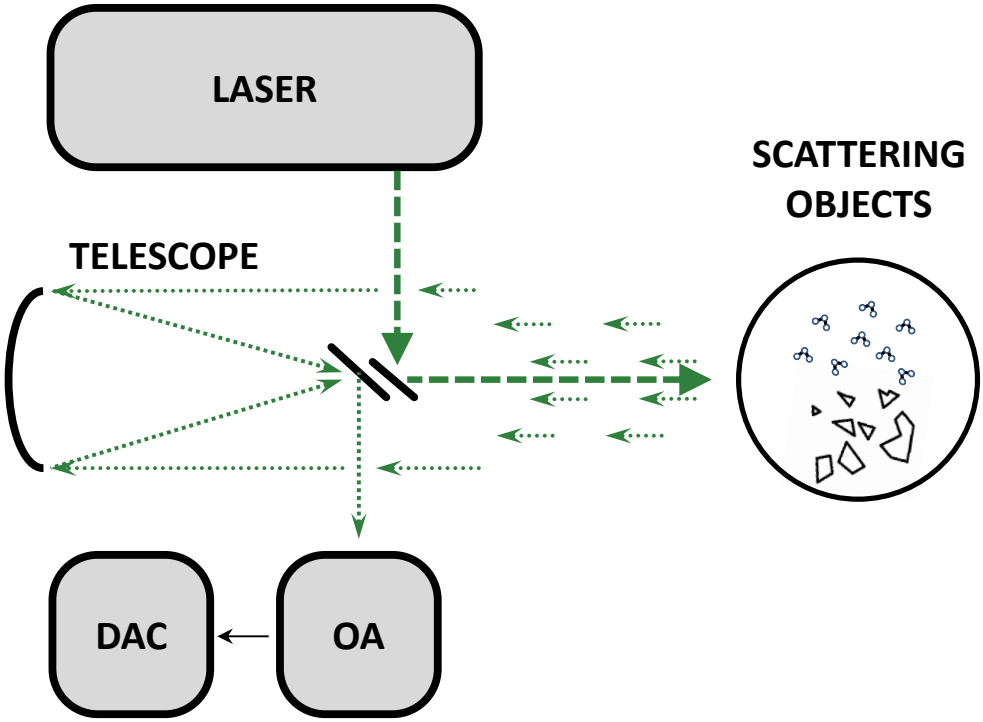

Figure 2.1: Schematic setup of a basic lidar system. Laser pulses are emitted into the atmosphere where they get scattered and absorbed by molecules and particles. Backscattered photons are collected by the telescope, detected by an optical analyzer (OA) and logged by a data acquisition computer (DAC).

$$I_r \;=\; \frac{P_V}{4\pi\, r^2}. \tag{2.4}$$

Thus, the telescope with area A receives the power,

$$P_{tel} \;=\; I_r\, A \;=\; \frac{P_V\, A}{4\pi\, r^2} \;=\; \frac{\beta' \,\frac{c\tau_L}{2}\, P_0\, A}{4\pi\, r^2}. \tag{2.5}$$

From the time-difference between the emission of the laser pulse (t_0) and the detection of the backscattered light (t) at the telescope the distance r to the scattering objects can be determined,

$$r \;=\; \frac{c\,(t - t_0)}{2}. \tag{2.6}$$

A time-difference of 10 μs, for example, corresponds to a distance of 1.5 km from the lidar system.

The received optical power is in a next step converted to electrical power by an optical analyzer (OA) and stored by a data acquisition computer (DAC). Since only very small fractions of the emitted photons are scattered in backward direction, the OA usually contains avalanche photo diodes (APDs) or photo-multipliers (PMs) for signal-amplification and the conversion of optical signals to electrical signals. The DAC stores the number of photon-counts per preset time interval Δt_r after the emission of the laser pulse. Thus, the range resolution ΔR of the lidar system, depends on the length of Δt_r and is given as,

$$\Delta R \;=\; \frac{c\,\Delta t_r}{2}. \tag{2.7}$$

For instance, a chosen time interval of 100 ns results in a range resolution of 15 m (for $\tau_L < \Delta R$). The performance of the system for the power conversion is summarized by a so-called systems constant C. Using the volume backscatter coefficient for isotropic scattering processes $\beta = \beta'/4\pi$ yields,

$$P_r \;= C\; P_{tel} \;=\; C\; P_0\; A\; \frac{1}{r^2}\; \beta(r)\; \frac{c\,\tau_L}{2}. \tag{2.8}$$

The additional consideration of the attenuation to and from the scattering volume (Lambert-Beer Law) forms the so-called lidar equation,

$$P_r \;=\; P_0\; A\; C\; \frac{1}{r^2}\; \beta(r)\; \frac{c\,\tau_L}{2}\; e^{-2\int_0^r\; \alpha(r')dr'}. \tag{2.9}$$

It relates the received power at the lidar instrument to the optical atmospheric processes and system parameters.

Both particles and molecules contribute to the extinction and backscatter coefficient α and β,

$$\alpha \;=\; \alpha_m \;+\; \alpha_p; \;\; \beta \;=\; \beta_m \;+\; \beta_p, \tag{2.10}$$

where α_m and β_m denote molecular extinction and backscatter coefficients and α_p and β_p specify particle extinction and backscatter coefficients. Thus, Equation 2.9 comprises four unknown variables, i.e. β_p, β_m, α_p and α_m, which need to be determined to solve it. α_m can be calculated from atmospheric pressure and temperature profiles (e.g. radiosonde data) and is linked to β_m via the Rayleigh phase function $\boldsymbol{P_m(\theta)}$,

$$\frac{\alpha_m}{\beta_m} \;=\; \frac{\int^{4\pi} \boldsymbol{P_m(\theta)}\; d\Omega}{\boldsymbol{P_m(\theta)}_{\boldsymbol{\theta=\pi}}} \;=\; \frac{8}{3}\pi\; sr \;=\; S_m. \tag{2.11}$$

Here, S_m is the so-called molecular lidar ratio, θ the scattering angle and Ω the solid angle. The application of this relation still leaves two unknown variables in equation Equation 2.9. Relating β_p and α_p to each other by introducing a lidar ratio for atmospheric particles S_p would reduce the number of unknowns to one and the equation could in principle be solved (*Klett*, 1981). However, other than for β_m and α_m, there is no general relation between β_p and α_p, as both variables are very sensitive to the shapes and the refractive indices of the

scattering particles. This is why for simple backscatter lidar systems S_p has to be assumed and is commonly taken from aerosol/cloud-databases or in situ measurements. Moreover, S_p is only constant for a single particle type (e.g. ice crystals or mineral dust aerosol). Considering the vast variety of particle species in the atmosphere, the assumption of S_p is a major error source for the retrieval of α_p and a huge disadvantage of simple backscatter lidar systems.

Methods that measure β_p and α_p independently from each other overcome this problem and reduce the uncertainties in the retrieval of α_p. As of today two methods are frequently used in atmospheric science, i.e. the Raman lidar technique and the High Spectral Resolution Lidar technique (HSRL) which is discussed in Section 2.1.2. Raman lidar systems make use of inelastic molecular scattering (also called Raman scattering; *Raman and Krishnan*, 1928) to determine atmospheric extinction, trace gas concentrations or atmospheric temperatures. Due to the fact that inelastic backscattered lidar signals are affected by particle extinction but not by particle backscatter, α_p can be determined without making assumptions on S_p. However, the retrieval of α_p using Raman lidar measurements is limited mostly to the nighttime, since signals from Raman scattering are by at least two magnitudes smaller than signals from elastic scattering and solar noise cannot be suppressed using bandwidth-filters. Additionally, long integration times of a few hours are needed to improve the signal-to-noise-ratio. As a consequence, Raman lidar is inappropriate for applications on fast moving platforms (e.g. aircraft or satellites). This is why in this study the HSRL method is used for the direct determination of α_p.

2.1.2 High Spectral Resolution Lidar

The High Spectral Resolution Lidar (HSRL) technique utilizes the different scattering properties of molecules and particles in the atmosphere to determine α_p. Lidar return signals usually show Doppler frequency shifts that are caused by photons which are scattered from moving molecules and aerosols. Whereas the velocity of particles in the atmosphere is defined by wind and turbulence and takes typical values around $10\,\mathrm{m\,s^{-1}}$, molecular velocity is defined by random thermal motion and can be as high as $300\,\mathrm{m\,s^{-1}}$. As a reason, the frequency shift caused by scattering aerosols (FWHM ≈ 0.1 GHz, Mie scattering) is very small compared to the shift caused by molecules (FWHM ≈ 1.5 GHz). This is highlighted in the distribution of the lidar return signal shown in Figure 2.2 (a), which is characterized by broad wings that are caused by scattering from molecules (due to the strong Doppler broadening) and a spike near the emitted laser-frequency that is caused by particle-scattering. HSRL technique exploits these different scattering characteristics and utilizes narrow-bandwidth filters (usually atomic or molecular notch filters; *Groß et al.*, 2012) of approximately 1 GHz width to distinguish between them (Figure 2.2 (b)). Therefore, the backscattered signal is split up into two channels using a beamsplitter in front of the detection devices. The first channel detects the total backscattered return signal with power P_{tot},

$$P_{tot}(r) = C_{tot}\,\frac{\beta_{tot}(r)}{r^2}\,e^{-2\int_0^r \alpha(r')\,dr'}, \qquad [\alpha = \alpha_m + \alpha_p]. \tag{2.12}$$

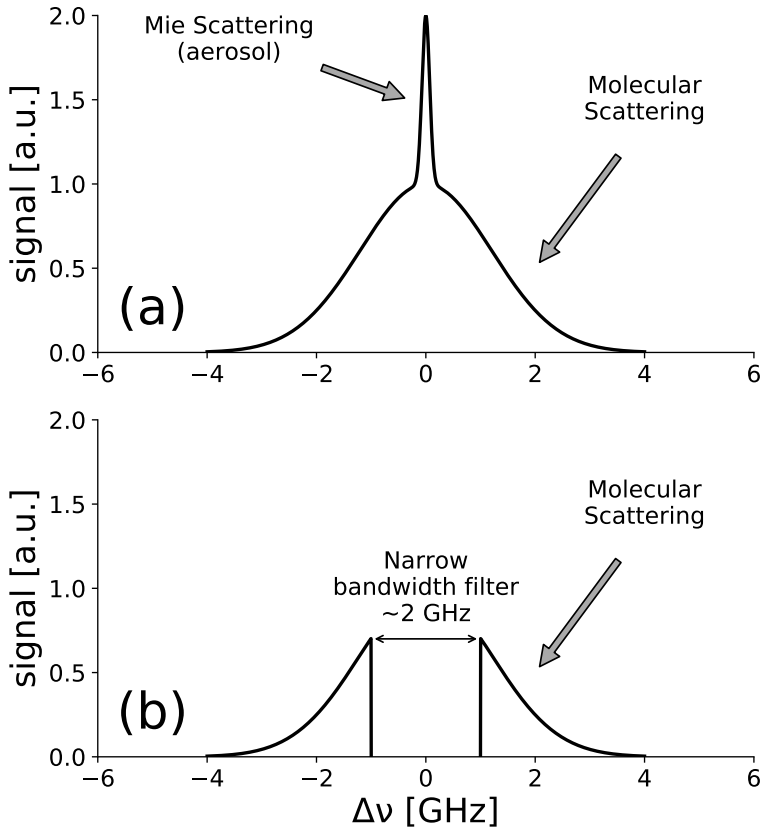

Figure 2.2: (a) Idealized illustration showing the frequency offset ($\Delta\nu$) of the emitted laser-wavelength in a lidar return signal from a mixture of aerosols and molecules. (b) Filtered molecular signal after the application of a narrow-bandwidth filter.

In the second channel the narrow-bandwidth filter is mounted in front of the receiving optics and only photons which were scattered from molecules can reach the detector. Due to these direct measurements of β_m the lidar equation for the molecular part of the return signal,

$$P_m(r) = C_m \, \frac{\beta_m(r)}{r^2} \, e^{-2\int_0^r \alpha(r')\, dr'}, \qquad [\alpha = \alpha_m + \alpha_p]. \tag{2.13}$$

can easily be solved for α_p. Here, the instrument parameter C_m accounts for both the systems characteristics and the fact that parts of the molecular signal also get rejected by the filter. Since the transmission-term $exp[-2\int_0^r \alpha(r')\ dr']$ is the same for both HSRL-channels, β_{tot} can easily be calculated by solving Equation 2.12. Additionally, the backscatter ratio $\boldsymbol{R}$ can be determined,

$$\boldsymbol{R} \;=\; \frac{\beta_{tot}}{\beta_m} \;=\; \frac{\beta_p + \beta_m}{\beta_m}. \tag{2.14}$$

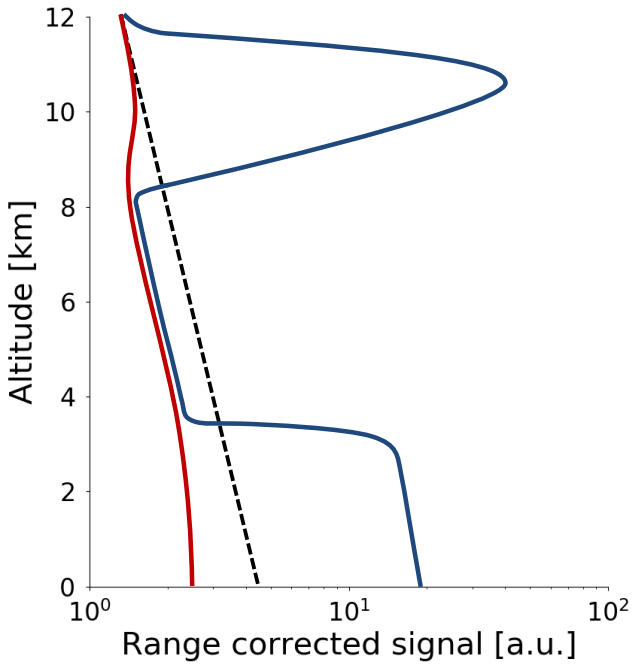

Figure 2.3: Illustration of range-corrected signals as measured by a downward-looking HSRL (blue: total backscatterd signal including scattering from molecules, from a cirrus cloud in 10 km altitude and from aerosol particles in the planetary boundary layer below 4 km altitude; red: measured backscattered signal after the removal of the part caused by cloud and aerosol particles using a narrow-bandwidth filter; black, dashed: calculated molecular backscatter signal for a pure atmosphere without any cloud or aerosol particles). Adapted from *Groß et al.* (2012).

Figure 2.3 illustrates how an exemplary signal of a two-channel HSRL-setup would look like. HSRL-systems are complex systems and are difficult to engineer. However, they provide a much stronger molecular signal than Raman lidar systems. As solar noise can easily be blocked by the application of narrow-bandwidth filters, HSRL systems can be operated during both nighttime and daytime with short integration times. This feature makes HSRL a suitable system for airborne and spaceborne research.

2.1.3 Differential Absorption Lidar

Atmospheric lidar systems can not only be used for the investigation of aerosols and clouds, but can also be utilized to determine atmospheric trace gas concentrations (e.g. H_2O, SO_2, NO, NO_2, O_3, CH_4, CO_2, etc.). Raman lidar systems, for example, analyze the backscattered signals of inelastic molecular scattering to deduce atmospheric concentrations of trace gases.

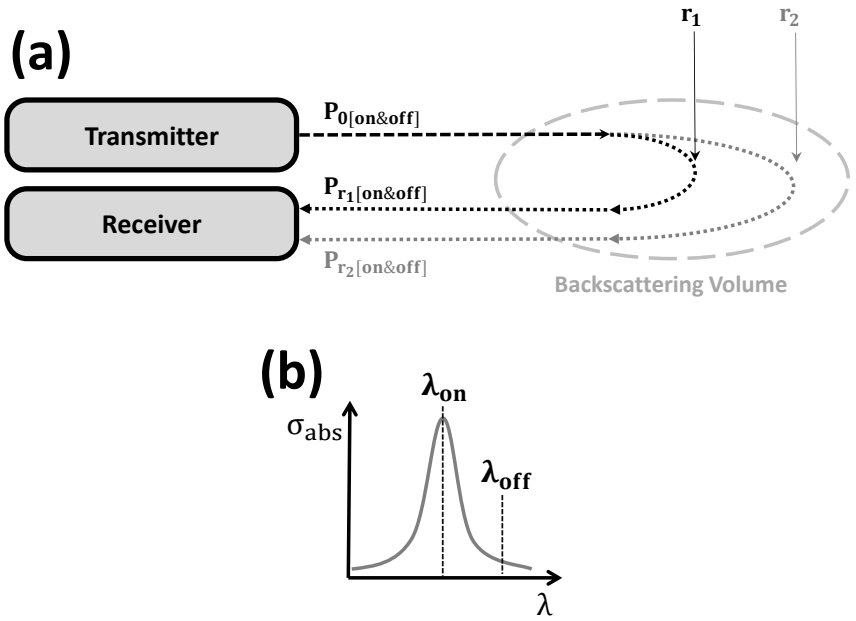

Figure 2.4: (a) Concept of a Differential Absorption Lidar system. The transmitter emits both online and offline lidar pulses with powers $P_{0[on]}$, $P_{0[off]}$ and wavelengths λ_{on}, λ_{off} into the atmosphere. From the differences in received powers, which are caused by the differing absorption properties of λ_{on} and λ_{off} in the atmosphere (see (b), where σ_{abs} indicates the absorption cross section of the desired trace gas), the number concentration of the trace gases can be derived.

However, due to the small Raman cross sections, the technique is limited to the investigation of trace gases with high atmospheric concentrations, e.g. H_2O. Small ratios of signal-to-noise have to be compensated by the application of big telescopes and long integration times, hence prohibiting the use of Raman lidar systems on aircraft.

In this work another technique for measurements of atmospheric water vapor is used: the so-called DIfferential Absorption Lidar (DIAL) technique. DIAL systems can be used to detect trace gases along the lidar beam with short integration times (a few seconds) and high sensitivity. They are based on different molecular absorption properties of the desired gas at two wavelengths, i.e. an online wavelength λ_{on}, where the absorption cross section σ_{abs} of the gas is large, and an offline wavelength λ_{off} where σ_{abs} is relatively small (see Figure 2.4). Both wavelengths have to be very near to each other, as absorption of other gas-species should be the same at both wavelengths. In an ideal scenario the difference in the atmospheric extinction coefficients at both wavelengths can then be related to the difference in σ_{abs} (which is well known from laboratory measurements),

$$\Delta\alpha = n\Delta\sigma_{abs}, \tag{2.15}$$

with n being the number density of the trace gas. The lidar equations for both wavelengths

are,

$$\begin{aligned} P_{on}(r) &= P_{0[on]}\, C_{on}\, \frac{A}{r^2}\, \beta_{on}(r)\, \frac{c\Delta T}{2}\, e^{\int_0^r n[\sigma_{scat}(\lambda_{on},r')\sigma_{abs}(\lambda_{on},r')]dr'}, \\ P_{off}(r) &= P_{0[off]}\, C_{off}\, \frac{A}{r^2}\, \beta_{off}(r)\, \frac{c\Delta T}{2}\, e^{\int_0^r n[\sigma_{scat}(\lambda_{off},r')\sigma_{abs}(\lambda_{off},r')]dr'} \end{aligned} \tag{2.16}$$

with $\sigma_{abs}(\lambda_{on}, r)$ and $\sigma_{abs}(\lambda_{off}, r)$ being the molecular absorption cross sections for the online and the offline wavelength. Assuming that the atmospheric backscatter coefficients ($\beta_{on}(r)$, $\beta_{off}(r)$) and scattering cross sections ($\sigma_{scat}(\lambda_{on}, r)$, $\sigma_{scat}(\lambda_{off}, r)$) are identical for both wavelengths the lidar equations can be rewritten to,

$$ln\left(\frac{P_{on}(r)}{P_{off}(r)}\right) = ln\left(\frac{P_{0[on]}\, C_{on}}{P_{0[off]}\, C_{off}}\right) - 2\int_0^r n[\sigma_{abs}(\lambda_{on}, r') - \sigma_{abs}(\lambda_{off}, r')]dr'. \tag{2.17}$$

Differentiation yields the so-called DIAL-equation,

$$n(r) = \frac{1}{2\,\Delta\sigma_{abs}}\, \frac{d}{dr}\, ln\left(\frac{P_{on}(r)}{P_{off}(r)}\right), \tag{2.18}$$

which allows to directly determine the number concentration of the trace gas from the ratio of the online and offline signal. Equation 2.18 does not contain any instrument constants. This makes DIAL a self-calibrating measurement technique. Remaining uncertainties arise from the facts that in reality β and σ_{scat} are not completely the same for both wavelengths and that there may be interfering gases in addition to the gas of interest.

2.1.4 Depolarization Lidar

The third lidar technique used in this work is the depolarization lidar technique. It exploits the polarization-characteristic of light as an electromagnetic wave. At any time the electromagnetic field of an electromagnetic wave oscillates along the electric and the magnetic field vectors which have a specific orientation in space. Polarization describes the orientation of these oscillations. Light is called linearly polarized, if the planes of oscillations for both vectors does not change with time. However, light can also be of circular polarization if the vectors rotate with constant rate as the wave travels.

When polarized light gets scattered by atmospheric particles its degree of polarization can change (depolarization). Whereas scattering at spherical particles of homogeneous content does not change the polarization of the wave (Lorentz-Mie theory), scattering at aspherical particles or particles of inhomogeneous content may introduce a depolarized component to the scattered wave. The strength of the depolarization does not only depend on the shape and content of the scattering particle but also on its relative size compared to the wavelength λ of the light. The relation between particle radius r and λ can be described using the non-dimensional size parameter,

$$\tilde{x} = \frac{2\pi r}{\lambda}. \tag{2.19}$$

For $\tilde{x} >$ (50-100) (e.g. $\lambda = 532$ nm and $r >$ 4.2-8.5 μm) depolarization can be retraced using ray-tracing methods in the domain of geometric optics of the particles. It has been shown that reflections and refractions inside the scattering particles together with their degree of complexity determine the orientation of the plane of oscillation in the backscattered light (*Liou and Lahore*, 1974). Other techniques like the T-Matrix method, the finite domain method or the discrete dipole approximation have to be applied to investigate depolarizing effects from inhomgeneous particles with radii comparable to λ ($\tilde{x} \approx 2\pi$). Large variations of scattering parameters with changing sphere size have been found by employing such techniques (*Sassen*, 2005).

Principle

A depolarization lidar system utilizes polarization optics to quantify the degree of depolarization introduced by the above mentioned processes at scattering particles. The system emits linearly polarized light into the atmosphere and analyzes the backscattered light in terms of its polarization to measure the volume linear depolarization ratio δ_v and the particle linear depolarization ratio δ_p.

δ_v is defined as the ratio of the total cross-polarized to the total parallel-polarized backscatter coefficient but also as the ratio of the respective received power-components ($P_\parallel, P_\perp$):

$$\delta_v = \frac{\beta_\perp}{\beta_\parallel} = \frac{P_\perp}{P_\parallel}. \tag{2.20}$$

δ_p is defined as the ratio of the parallel- and cross-polarized backscatter coefficient due to particle scattering and can be determined using HSRL or Raman lidar together with depolarization detection techniques:

$$\delta_p = \frac{\beta_{p\perp}}{\beta_{p\parallel}}. \tag{2.21}$$

To determine δ_v and δ_p, the received backscattered power (P) is separated into $P_\parallel$ and $P_\perp$ using a polarizing beamsplitter cube (PBSC; Figure 2.5). The lidar equation can then be split up:

$$P = P_\parallel + P_\perp = P_0\, A\, C_\parallel \frac{\beta_\parallel}{r^2}\, e^{-2\int_0^r \alpha_\parallel(r')dr'} + P_0\, A\, C_\perp \frac{\beta_\perp}{r^2}\, e^{-2\int_0^r \alpha_\perp(r')dr'}. \tag{2.22}$$

Here $C_\parallel$ and $\alpha_\parallel$ mark the parallel polarized components and $C_\perp$ and $\alpha_\perp$ the cross polarized components of the system parameter and the extinction coefficient. The power components that are parallel (p) and perpendicular (s) to the incident plane of the PBSC are,

$$\begin{aligned} P_s(\varphi) &= P_\parallel \sin^2(\varphi) + P_\perp \cos^2(\varphi), \\ P_p(\varphi) &= P_\parallel \cos^2(\varphi) + P_\perp \sin^2(\varphi), \end{aligned} \tag{2.23}$$

with φ being the angle between the plane of the PBSC and the plane of polarization of the laser beam. The PBSC transmits and reflects the two components according to its own

transmittances (T_p, T_s) and reflectances (R_p, R_s). In the subsequent channels the signals get amplified and recorded. The reflected power component (P_R) and the transmitted power component (P_T) can then be described as follows,

$$\begin{aligned} P_R(\varphi) &= P_p(\varphi)\, R_p\, V_R + P_s(\varphi)\, R_s\, V_R, \\ P_T(\varphi) &= P_p(\varphi)\, T_p\, V_T + P_s(\varphi)\, T_s\, V_T, \end{aligned} \tag{2.24}$$

where V_T and V_R include the receiver's optical loss and electronic amplification. Introducing the relative amplification factor $V_\star = V_R/V_T$ as well as the signal ratio $\delta_\star = P_R(\varphi)/P_T(\varphi)$ and using δ_v together with Equation 2.23 and Equation 2.24 yields,

$$\delta_\star(\varphi) = V_\star \frac{[1+\delta_v \tan^2(\varphi)]R_p + [\tan^2(\varphi) + \delta_v]R_s}{[1+\delta_v \tan^2(\varphi)]T_p + [\tan^2(\varphi) + \delta_v]T_s}. \tag{2.25}$$

Here, $V_\star$ has to be determined via calibration measurements (see Section 2.1.4). Once $V_\star$ is determined, δ_v can be calculated. For $\varphi = 0°$, δ_v is given as,

$$\delta_v = \frac{\beta_\perp}{\beta_\parallel} = \frac{P_\perp}{P_\parallel} = \frac{P_s}{P_p}. \tag{2.26}$$

As the received parallel-polarized signal is much stronger than the cross-polarized signal and due to the fact that for commercial PBSCs R_s is usually much closer to 1 than T_s, it is beneficial to use an alignment of $\varphi = 90°$ to reduce cross-talk:

$$\delta_v = \frac{P_\perp}{P_\parallel} = \frac{P_p}{P_s}. \tag{2.27}$$

δ_v can then be determined with high accuracy using $\delta_\star$ and $V_\star$ from calibration measurements together with Equation 2.20 and Equation 2.23,

$$\delta_v = \frac{R_s - T_s \frac{\delta_\star}{V_\star}}{T_p \frac{\delta_\star}{V_\star} - R_p}. \tag{2.28}$$

Following *Biele et al.* (2000) and using the backscatter ratio $\boldsymbol{R}$ (Section 2.1.2) δ_p can also be derived:

$$\delta_p = \frac{\beta_{\perp p}}{\beta_{\parallel p}} = \frac{(1+\delta_m)\,\delta_v\,\boldsymbol{R} - (1+\delta_v)\,\delta_m}{(1+\delta_m)\,\boldsymbol{R} - (1+\delta_v)}. \tag{2.29}$$

Here, δ_m is the volume linear depolarization ratio of air molecules, which can be calculated with high accuracy (*Behrendt and Nakamura*, 2002).

Calibration

To calibrate the depolarization retrieval, $V_\star$ has to be determined via calibration measurements. For $\varphi = 0°$, Equation 2.25 can be rewritten to,

$$V_\star = \frac{[T_p + \delta_v\, T_s]}{[R_p + \delta_v\, R_s]}\, \delta_\star(0°). \tag{2.30}$$

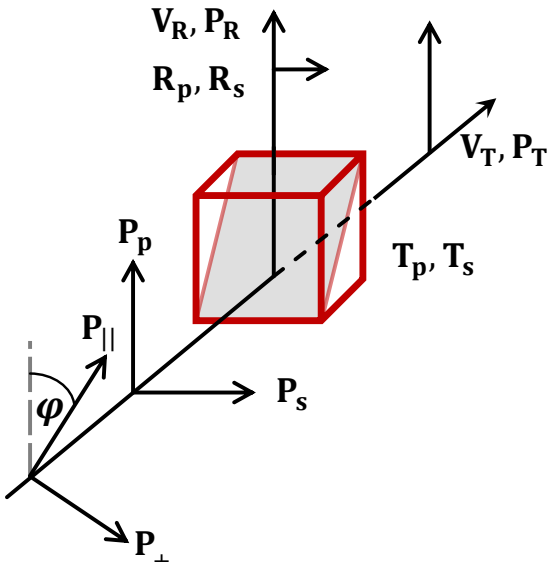

Figure 2.5: Schematic overview of the signal power components in a receiving unit comprising a PBSC. Shown are reflectivities R_p and R_s as well as transmittances T_p and T_s for linearly polarized light parallel (p) and perpendicular (s) to the incident plane of the PBSC. $P_\perp$ and $P\|$ indicate the received perpendicular and parallel power components. P_p and P_s are the power components that are parallel and perpendicular to the plane of the PBSC. P_R and P_T represent the measured powers in the reflected and transmitted path. V_R and V_T are the corresponding amplification factors which include the optical transmittances. φ marks the angle between the plane of the PBSC and the plane of polarization of the laser beam. Reproduced after *Freudenthaler et al.* (2009).

Due to the fact that the linear depolarization for air molecules is well known, an aerosol-free range gate can be used to solve Equation 2.30 and to determine $V_\star$ ($\delta_m = \delta_v$). However, already a small amount of depolarizing particles in the assumed aerosol-free range gate leads to huge errors in calculated $V_\star$.

A more reliable calibration method uses the fact that $\tan^2(\pm 45°) = 1$. It turns Equation 2.30 to,

$$V_\star = \frac{T_p + T_s}{R_p + R_s}\,\delta_\star(\pm 45°). \tag{2.31}$$

Here, $V_\star$ is independent of δ_v, but only a small angular derivation from $\varphi = 45°$ leads to large errors in $V_\star$.
Freudenthaler et al. (2009) showed that errors caused by misalignments of the PBSC with respect to the incident laser polarization plane can be minimized by making two subsequent measurements at $\varphi = -45°$ and $\varphi = +45°$. The receiver optics are therefore rotated by 90°

between the two measurements and the calibration errors are compensated very well:

$$V_\star = \frac{T_p + T_s}{R_p + R_s} \sqrt{\delta_\star(+45°) \cdot \delta_\star(+45°)}. \tag{2.32}$$

2.2 The airborne lidar system WALES

The WALES lidar instrument is an airborne demonstrator for a planned but so far not conducted spaceborne lidar mission which aims to measure vertically highly resolved profiles of water vapor around the globe. The system combines all of the three described lidar techniques discussed in Section 2.1, i.e. the DIAL, the depolarization lidar and the HSRL technique.

2.2.1 System design

WALES is capable of simultaneous measurements of both aerosol optical properties and water vapor distributions from aircraft to ground level. The DIAL module is designed as a four-wavelength/three-absorption line measurement scheme which guarantees highly sensitive measurements of water vapor in the 935 nm absorption band at all tropospheric and lower-stratospheric levels. The HSRL-module operates at 532 nm and ensures direct measurements of particle extinction along the lidar beam. In the following the transmitter and receiver setups are described. A schematic illustration of the setups is shown in Figure 2.6 and a detailed description of the whole system can be found in *Esselborn et al.* (2008) and *Wirth et al.* (2009). A list of the most important performace parameters can be found in Table 2.1.

Transmitter: The WALES transmitter consists of two identical laser systems which operate temporally interleaved. This setup allows for high pulse repetition rates of 200 Hz. The centerpieces of both transmitters are Q-switched Nd:YAG ring-lasers in master oscillator/power amplifier configuration with repetition rates of 100 Hz and pulse lengths of 8 ns. The master lasers are amplified by a factor of 10^4, show pulse energies of 400 mJ and are integrated to pressure-tight and temperature-tunable housings to ensure pressure and thermal stability. For HSRL and DIAL operations parts of the emitted radiations are frequency doubled to 532 nm (200 mJ pulse energy) using a second-harmonic generator (SHG) with potassium titanyl phosphate (KTP; $KTiOPO_4$) acting as nonlinear material.

Parts of the frequency-doubled radiations are in a next step directed to the DIAL module of WALES to pump injection seeded optical parametric oscillators (OPOs; *Mahnke et al.*, 2007) in four-mirror configurations with two KTP-crystals serving as nonlinear material. The crystals are mounted on rotation stages for coarse wavelength setting. Additionally, each crystal is mounted on a piezo-transducer-driven flexure stage for fine tuning and rapid switching of the phase matching angle. This assembly enables fast switching between the four DIAL-wavelengths on a shot-to-shot basis. Both OPOs use injection seeding for narrow-band operation. Therefore, they are seeded by four independent distributed feedback (DFB) laser diodes with output-powers of 35 mW. To ensure absolute frequency stability the DFB-laser radiation for the

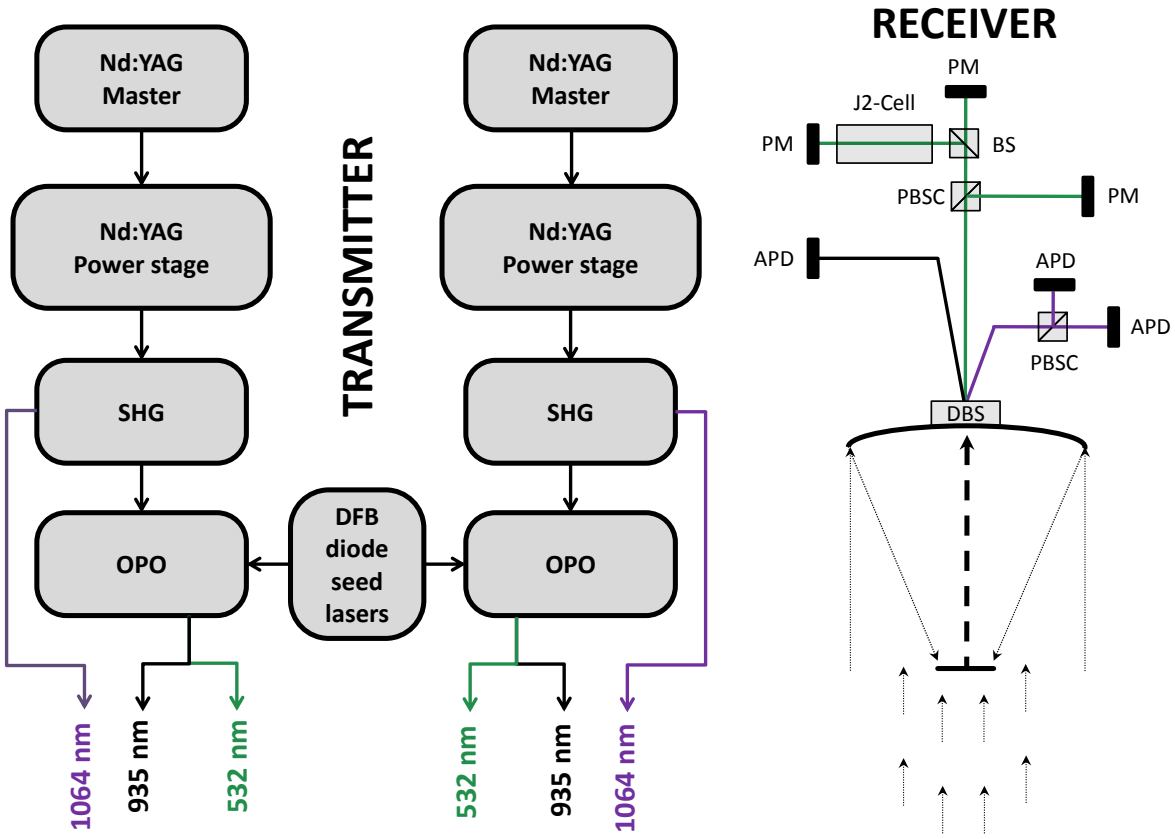

Figure 2.6: Layout of the WALES transmitter and receiver.

strongest H_2O-absorption line is transmitted through a multi-pass absorption cell filled with 80 hPa of pure water vapor. The other DFB-diodes are stabilized using a wavemeter which is continuously re-calibrated against the first DFB-diode. For airborne HSRL-measurements of particle extinction a long-term frequency stability of better than 1 MHz is necessary. The 532 nm-lasers are therefore frequency-stabilized to the iodine line by transmitting a part of the radiation through an iodine cell. To guarantee the pulse repetition rate of 200 Hz the time lag between the outgoing pulses of both lasers is in a final step set to 5 ms.

Receiver: The receiver operates in a monostatic setup and consists of a 48 cm Cassegrain telescope mounted in near-nadir direction, an optical detection unit and the data acquisition computer. For depolarization calibration (see Section 2.1.4) the whole detection unit can be rotated around the optical axis of the telescope. The telescope directs incoming radiation towards dielectric beamsplitters (DBSs) which separate the incoming wavelengths to three different channels, i.e. the 532 nm, the 935 nm and the 1064 nm-channel. Bandwidth inter-

ference filters of 1 nm suppress solar background. Both the 532 nm and 1064 nm-channels are equipped with PBSCs which separate cross-polarized light from parallel-polarized light. In the 532 nm HSRL-channel half of the parallel-polarized radiation (a beamsplitter (BS) is used to split up the light) is additionally sent through an iodine-cell to separate the molecular-part of the signal from the total signal. At the end of all optical channels the signals are amplified and detected using photo-multipliers (PMs; 532 nm) and avalanche photo diodes (APDs; infrared channels).

Table 2.1: Performance parameters of the WALES system.

Transmitter		***Receiver***	
Pulse repetition per laser	100 Hz	⌀ Cassegrain telescope	0.48 m
Pump laser pulse energy at 1064 nm	400 mJ	Full overlap distance	800 m
Pump laser pulse energy at 532 nm	220 mJ	Detector 532 nm	PM
Pulse length at 1064 nm	8.0 ns	Detector 1064 nm & 935 nm	APD
Pulse length at 532 nm	5.2 ns		
Pulse length at 935 nm	7.5 ns		
WALES system output at 1064 nm	120 mJ	***System parameters***	
WALES system output at 532 nm	45 mJ	Weight	450 kg
WALES system output at 935 nm	75 mJ	Power consumption	2000 W
Beam divergence	1 mrad	Vertical resolution	15 m

2.2.2 Data attributes and error estimates

WALES operates in downward-looking direction with a 2-3° off-nadir angle. The instruments provides highly resolved vertical profiles of atmospheric particle backscatter β_p , particle linear depolarization δ_p and particle extinction α_p at 532 nm and 1064 nm ($\Delta z = 15$ m) as well as water vapor mass mixing ratio r_m ($\Delta z = 150$ m) from aircraft to ground level. The horizontal resolution is a function of aircraft speed and temporal resolution of the measurements. In this work the raw data with 0.2 s temporal resolution are averaged to 1 s (HSRL) and 16 s (DIAL) to improve the signal-to-noise ratio. This results in horizontal resolutions of 3.2 km (DIAL) and 0.2 km (HSRL) at a typical aircraft speed of 200 m s^{-1}.
Due to the high pulse repetition rate of the lasers *Kiemle et al.* (2008) estimated the relative uncertainty of the DIAL measurements to be smaller than 5 %. To ensure highest data quality of $\delta_{p(532)}$ frequent in-flight calibration procedures following the '$\pm 45^\circ$ method' (*Freudenthaler et al.*, 2009) as described in Section 2.1.4 are performed. The remaining relative uncertainties in $\delta_{p(532)}$, which are primarily caused by atmospheric variations during the calibration procedure, are estimated to be in the range from 10 % to 16 % (*Esselborn et al.*, 2008). For backscatter and extinction coefficients relative uncertainties of less than 5 % ($\beta_{p(532)}$) and 10 % to 20 % ($\alpha_{p(532)}$) must be considered, respectively.

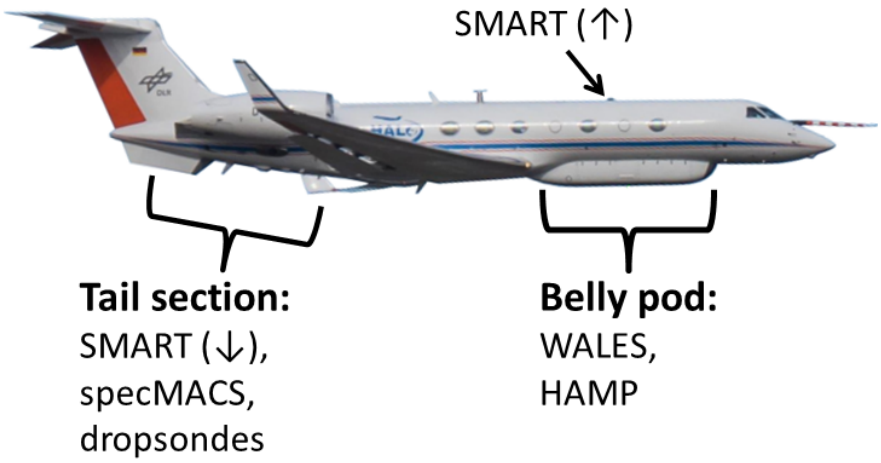

Figure 2.7: Illustration of the HALO instrument setup.

2.3 NARVAL - Next-generation aircraft remote sensing for validation studies

In this study WALES measurements conducted during the NARVAL-II mission (Next-generation Aircraft Remote sensing for VALidation studies-II; *Stevens et al.*, 2019) in August 2016 are used. The campaign aimed at studying the subtropical North Atlantic atmospheric circulation and the occurrence and formation of marine clouds during the wet summer season when annual dust-transport over the North Atlantic Ocean peaks (*Prospero and Lamb*, 2003). Moreover, studying the large scale atmospheric divergence was a main objective of NARVAL-II (*Bony and Stevens*, 2019).

During the campaign the HALO (High Altitude and LOng-range) research aircraft (*Krautstrunk and Giez*, 2012) served as an airborne platform for remote sensing measurements eastward the island of Barbados. The aircraft has a maximum range of more than 12000 km and a certified ceiling altitude of 15.545 km (max. altitude during NARVAL-II: $\sim$ 15 km). HALO was equipped with a combination of active and passive remote sensing instruments (Figure 2.7). Besides the lidar system WALES, a 35.2 GHz cloud radar (*Mech et al.*, 2014; *Ewald et al.*, 2019), the hyper-spectral imager (specMACS; *Ewald et al.*, 2016) and the Spectral Modular Airborne Radiation measurement System (SMART; *Wendisch et al.*, 2001) for radiation measurements have been operated on the aircraft. To get information on the thermodynamic state of the atmosphere, 218 dropsondes were additionally deployed. During NARVAL-II, 10 research flights (RFs) comprising a total of 85 flight hours were conducted. During four of those flights, flight patterns were specifically designed to lead over long-range-transported SALs eastward of Barbados (i.e. RF2, RF3, RF4 and RF6). Overall, a data set comprising

Table 2.2: Overview of the conducted research flights during NARVAL-II in 2016 including dates, times of take-off and landing, total duration as well as research objectives and flight hours in SAL regions (all times given in UTC - note: Atlantic Standard Time = UTC-4; TBPB: Grantley Adams International Airport; EDMO: Airport Oberpfaffenhofen).

Flight No.	Date	Take-off	Landing	Total Duration	Research objective	Dust
RF1	08 Aug	08:12 (EDMO)	18:51 (TBPB)	10:39 h	Transfer flight	-
RF2	10 Aug	11:52 (TBPB)	20:02 (TBPB)	08:10 h	Dust/no dust flight and divergence	∼2.3 h
RF3	12 Aug	11:43 (TBPB)	19:37 (TBPB)	07:54 h	Dust flight/Divergence	∼6.5 h
RF4	15 Aug	11:47 (TBPB)	19:46 (TBPB)	07:59 h	Dust/no dust flight	∼2.7 h
RF5	17 Aug	14:47 (TBPB)	23:08 (TBPB)	08:21 h	Satellite validation	-
RF6	19 Aug	12:28 (TBPB)	20:52 (TBPB)	08:24 h	Dust/no dust flight and divergence	∼4.5 h
RF7	22 Aug	13:16 (TBPB)	20:57 (TBPB)	07:41 h	ITCZ/Divergence	-
RF8	24 Aug	12:43 (TBPB)	20:55 (TBPB)	08:12 h	Tropical storm Garcon/Divergence	-
RF9	26 Aug	13:43 (TBPB)	20:54 (TBPB)	07:11 h	Tropical storm Garcon	-
RF10	30 Aug	09:42 (TBPB)	19:52 (EDMO)	10:10 h	Transfer flight/Divergence	-

38 h of measurements (22 h of lidar measurements during dust-free times, 16 h of lidar measurements with SAL present) are used in this work to investigate radiative effects of SALs and their impact on the subjacent marine shallow marine convection during NARVAL-II. Data sets obtained during the transfer flights from and to Germany (i.e. RF1 and RF10) are not included in the analysis because most measurements took place outside the trades and cirrus fields were present inside the trades. RF5 and RF7 are also excluded because cirrus fields covered most of the research area during RF5 and the objective of RF7 was to cross the ITCZ for several times. Table 2.2 gives a detailed overview of all performed NARVAL-II research flights including the main research objectives.

In Section 4.2 collected lidar measurements of marine trade wind cloud macrophysical properties inside the trades (10-20 °N) during NARVAL-II are compared to those collected during NARVAL-I: the predecessor of NARVAL-II which took place in the dust-free winter season 2013 (10 to 20 December; *Klepp et al.*, 2014). This is why Figure 2.8 illustrates an overview of the flight-tracks in dust-laden and dust-free regions during both NARVAL-I and NARVAL-II.

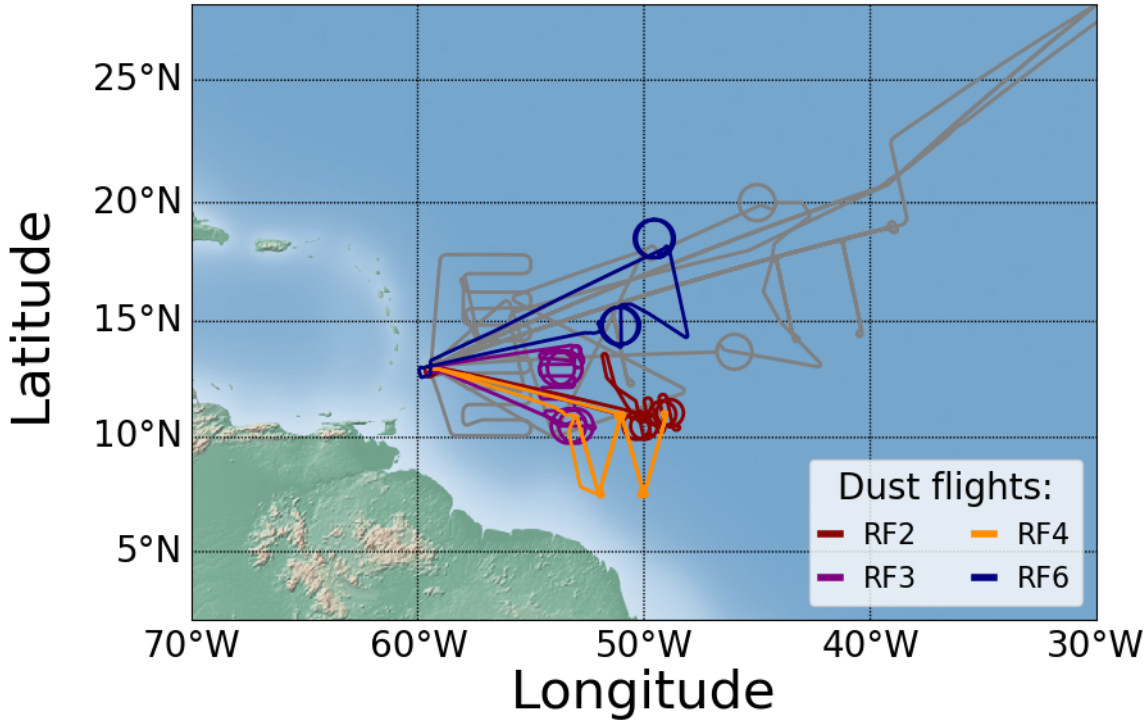

Figure 2.8: NARVAL research flight tracks: NARVAL-II dust-flights (color coded) and NARVAL-I and NARVAL-II dust-free flights (grey). During some research flights, aircraft routes were planned to have circular patterns for measurements of large scale atmospheric divergence (*Bony and Stevens*, 2019).

2.4 Radiative transfer calculations

Long-range-transported layers of mineral dust modify the Earth's radiation by scattering, absorption and emission processes.
Scattering processes can either lead to an increase or a reduction of radiation in a given direction. Scattering of radiation out of a given direction is given as,

$$\left(\frac{dI}{ds}\right)_{scat,out} = -\alpha_{scat}\, I, \tag{2.33}$$

where I is the radiance, s is the distance and α_{scat} is the extinction due to scattering. Scattering of radiation from other directions into a given direction can be written as,

$$\left(\frac{dI}{ds}\right)_{scat,in} = \frac{\alpha_{scat}}{4\pi} \int_0^{4\pi} I(\Omega')\; P(\Omega,\Omega')\; d\Omega' \tag{2.34}$$

where P is the probability that a photon is scattered from direction Ω' to Ω. Similar to scattering, absorption along a given direction in the atmosphere is given as,

$$\left(\frac{dI}{ds}\right)_{abs} = -\alpha_{abs}\, I, \tag{2.35}$$

with α_{abs} being extinction due to absorption. Since the atmosphere is in local thermodynamic equilibrium the emission of radiation can be written as,

$$\left(\frac{dI}{ds}\right)_{thermal} = \alpha_{abs} L_\nu(T). \tag{2.36}$$

Here $L_\nu(T)$ is the Planck function.

Combining the above equations for the effects of absorption, emission and scattering yields the Radiative Transfer Equation (RTE):

$$\begin{aligned} \frac{dI}{ds} &= -\left(\frac{dI}{ds}\right)_{abs} - \left(\frac{dI}{ds}\right)_{scat,out} + \left(\frac{dI}{ds}\right)_{scat,in} + \left(\frac{dI}{ds}\right)_{thermal} \\ &= -(\alpha_{abs}+\alpha_{scat})\; I \; + \frac{\alpha_{scat}}{4\pi} \int_0^{4\pi} I(\Omega')\; P(\Omega,\Omega')\; d\Omega' \; + \; \alpha_{abs} L_\nu(T). \end{aligned} \tag{2.37}$$

Radiative transfer models are commonly used to solve the RTE and to quantify radiative effects of aerosol layers or green house gases as well as to calculate atmospheric heating rates. They solve the RTE using numerical methods, e.g. discrete ordinate or Monte Carlo methods. The RTE is a monochromatic equation and solutions are calculated for individual spectral lines. Thus, one has to integrate the results of individual line-by-line calculations to compute exact radiances in a desired spectral region (e.g. the short-wave or long-wave region). Faster but less accurate methods use spectral band parametrizations to reduce the amount of individual line-by-line calculations.

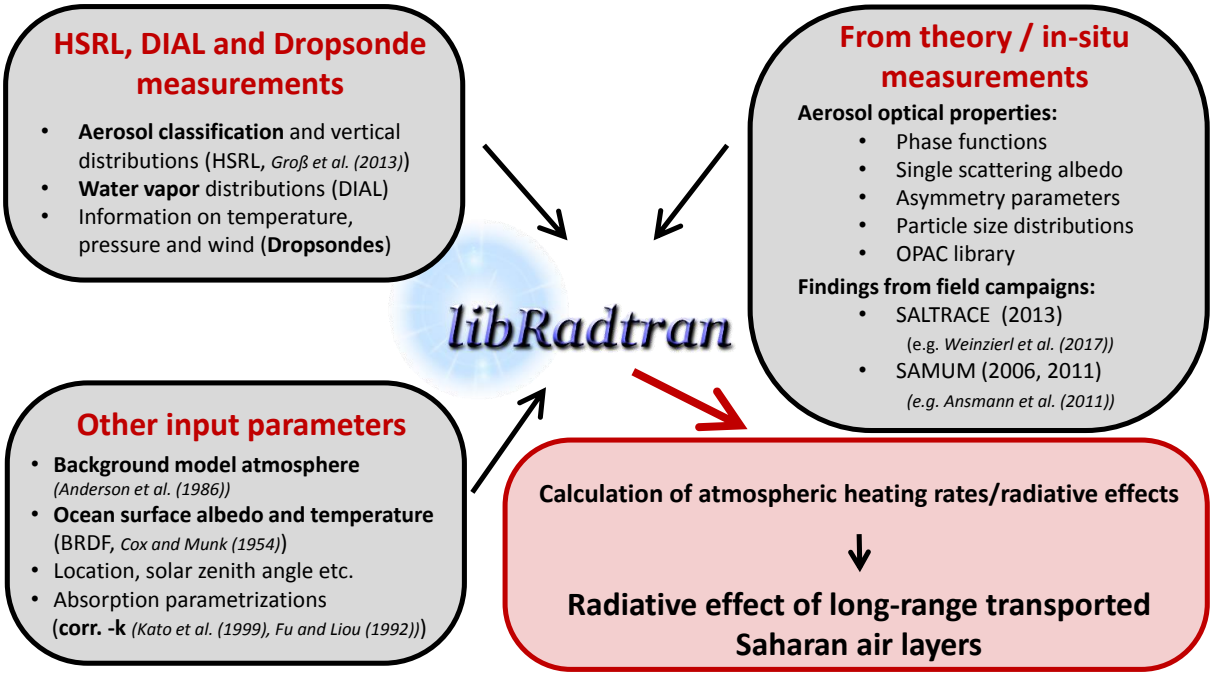

Figure 2.9: Schematic overview of the setup for radiative transfer calculations using libRadtran with lidar data.

In this work, the libRadtran radiative transfer model (library for Radiative transfer; *Mayer and Kylling*, 2005; *Emde et al.*, 2016) is used. It includes the most common RTE-solvers and spectral band parametrizations and provides a valuable toolkit for the parametrization of the model atmosphere using lidar data. Here, WALES DIAL and HSRL data are employed to parametrize vertical distributions of aerosol species and corresponding particle mass concentrations as well as water vapor mixing ratios. Together with well-known aerosol optical properties for mineral dust and marine aerosol, which were obtained from measurements during previous campaigns (i.e. SAMUM-1 (*Heintzenberg*, 2009), SAMUM-2 (*Ansmann et al.*, 2011) and SALTRACE (*Weinzierl et al.*, 2017)), as well as other modeled input parameters (e.g. ocean albedo and ozone distribution) atmospheric heating rates and aerosol radiative effects can be computed (Figure 2.9). This enables the investigation of impacts that elevated SALs have on atmospheric stability and the development of convection and clouds.

Details regarding radiative transfer calculations with libRadtran and the question how lidar data is used to parametrize the model atmosphere are discussed in the following sections.

2.4.1 The libRadtran software-package

The libRadtran software package (*Mayer and Kylling*, 2005; *Emde et al.*, 2016) contains a suite of valuable routines for radiative transfer calculations in the Earth's atmosphere. The core package, which is called uvspec, enables computations of radiances and irradiances as well as actinic fluxes and heating rates. Originally, uvspec was designed for radiative transfer calculations in the ultraviolet and visible parts of the spectrum (this is where the name comes from). However, over the years the package has been extended and improved and is now capable of computations in both the solar and the terrestrial parts of the spectrum. uvspec is divided in three main parts (Figure 2.10):

(I) a module that converts atmospheric quantities, e.g. pressure/temperature profile, trace gas concentration, cloud and aerosol microphysical properties, to optical properties,

(II) a set of RTE-solvers to choose from which calculate the radiances and irradiances as well as the actinic fluxes and heating rates,

(III) post processing tools to process the outputs, e.g. integration over wavelengths, calculation of brightness temperatures.

Depending on the problem at hand uvspec offers the user a set of various RTE-solvers to choose from, e.g. the fast two-stream code to approximately calculate one-dimensional irradiances (*Kylling et al.*, 1995), the accurate one-dimensional discrete ordinate solver DISORT (*Stamnes et al.*, 1988; *Buras et al.*, 2011) or even a Monte Carlo solver to solve the full three-dimensional RTE (*Emde and Mayer*, 2007; *Mayer*, 2009; *Emde and Mayer*, 2007; *Emde et al.*, 2010; *Buras and Mayer*, 2011; *Emde et al.*, 2011).

As WALES lidar measurements on the aircraft are of two-dimensional nature, the DISORT RTE-solver is employed for this study. It uses a predefined number of so-called streams or directions, for which the scattering phase function is described by means of appropriate Legendre-coefficients. Scattering at large aerosols causes lots of peaks in the phase functions. As a reason, a large number of streams would be needed for accurate radiative transfer calculations with DISORT. However, the intensity correction method as described by *Buras et al.* (2011) directly employs the scattering phase functions instead of expanding over their Legendre moments. It makes DISORT calculations of large aerosols much more accurate, lowers the number of needed streams and is therefore used in this work. It is applied with 16 streams in the short-wave ($0.12 - 4.0\,\mu$m) and long-wave ($2.5 - 100.0\,\mu$m) spectra.

From $0 - 10$ km altitude the model grid is set to 0.1 km. At higher altitudes from 10 km to 120 km altitude a coarser grid-spacing of several kilometers is chosen to save computational time (see Table 2.3). Sufficiently accurate correlated k-distribution absorption band parametrizations as described in *Kato et al.* (1999) and *Fu and Liou* (1992) are employed to avoid time-expensive spectral line-by-line calculations. Vertically resolved irradiances can then be calculated from the integration over the irradiances in the respective bands. Hence, libRadtran allows the calculation of the radiative flux (F) at any altitude z in the atmosphere.

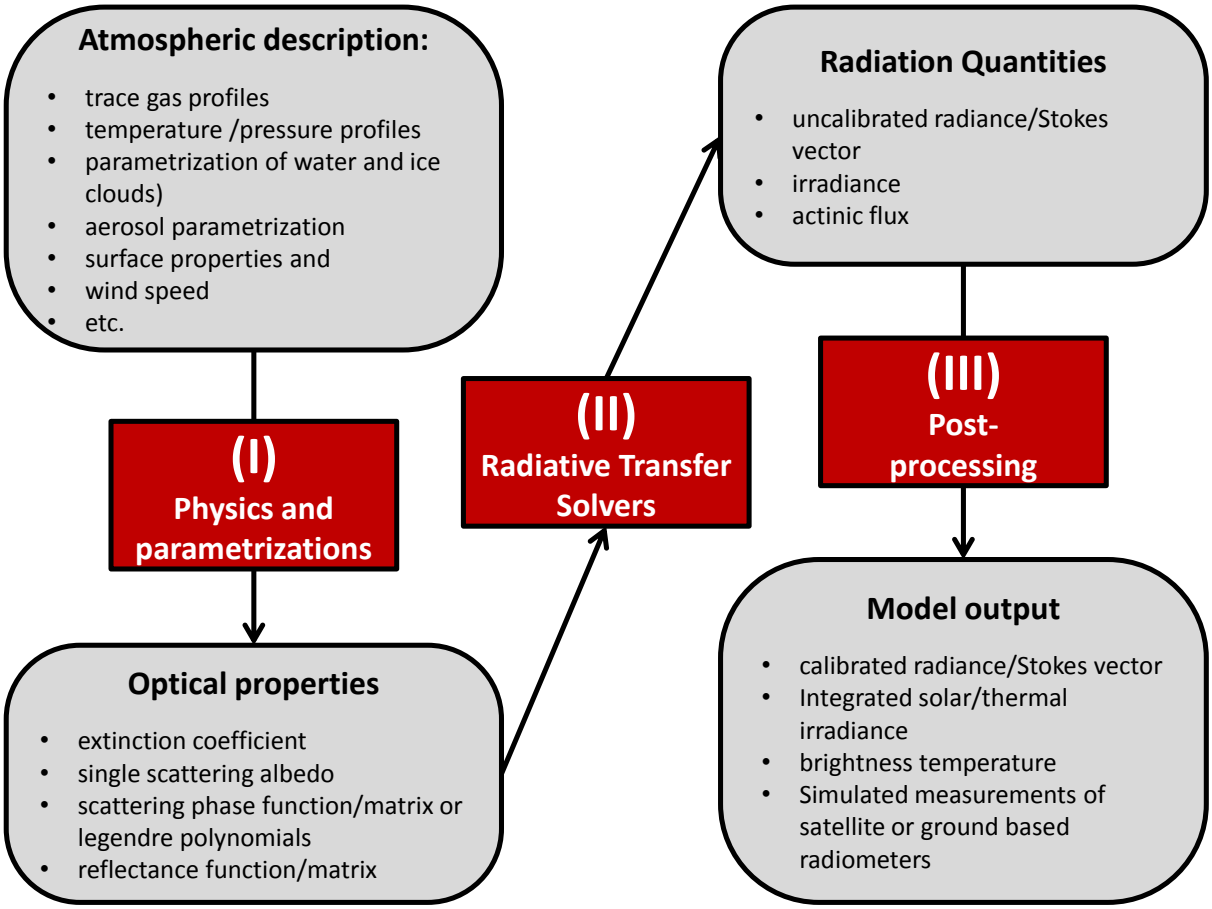

Figure 2.10: Structure of the uvspec-package. Reproduced after *Mayer and Kylling* (2005).

The net radiative flux F_{net} at altitude z is defined as the difference of the upwelling and the downwelling fluxes $F^{\uparrow}$ and $F^{\downarrow}$:

$$F_{net}(z) = F^{\uparrow}(z) - F^{\downarrow}(z). \tag{2.38}$$

The change of F_{net} with altitude z is then used to calculate atmospheric heating rates,

$$\frac{\delta T}{\delta t}(z) \;=\; -(c_p\,\rho_{air}(z))^{-1}\frac{\delta F_{net}}{\delta z}(z). \tag{2.39}$$

Here c_p is the specific heat capacity of air at constant pressure (humidity and temperature dependent) and $\rho_{air}(z)$ is the altitude dependent density of air.

Dropsonde measurements are used to parametrize atmospheric pressure and temperature profiles in the radiative transfer model. Moreover, measured wind speeds from dropsonde

Table 2.3: Vertical resolution of the used radiative transfer model.

Altitude [km]	Resolution [km]
0.0 to 10.0	0.1
10.0 to 30.0	1.0
30.0 to 60.0	10.0
60.0 to 120.0	20.0

measurements are employed to estimate the sea surface roughness and albedo using the bidirectional reflectance distribution function (BRDF; *Cox and Munk*, 1954a,b; *Bellouin et al.*, 2004). The BRDF represents the fraction of reflected radiation for all possible combinations of incident and reflection geometry. Over the ocean the BRDF is anisotropic and is calculated as the Fresnel reflection function weighted by the wave slope probability at a given wind speed. Reference profiles as described by *Anderson et al.* (1986) parametrize model trace gas concentrations, e.g. the ozone profile. Based on MODIS-Aqua/Terra measurements, which indicated a homogeneous sea surface temperature during NARVAL-II, surface temperature is set to a fixed value of 302 K.

2.4.2 Aerosol optical properties from lidar measurements

Aerosol classification

WALES measurements of $\delta_{p(532)}$ can be used to detect different types of aerosols in vertical lidar profiles. *Groß et al.* (2013) showed that values of $\delta_{p(532)}$ differ for various aerosol species (Figure 2.11). They found that mineral dust and dust mixtures show high values of $\delta_{p(532)}$ in the range from approximately 0.2 to 0.4. Biomass burning aerosol and anthropogenic pollution were found to be moderately depolarizing ($0.04 < \delta_{p(532)} < 0.20$) and marine aerosol was found to be only weakly depolarizing ($\delta_{p(532)} < 0.04$).

Marine aerosol consists of sea salt and water-soluble parts and is mainly confined to the MBL. Due to its spherical shape at high relative humidities it is a weakly depolarizing aerosol type in moist environments. Dry sea salt and thus stronger depolarizing marine aerosol (*Murayama et al.*, 1999; *Sakai et al.*, 2010) is not expected in this study, since relative humidity in the MBL was observed to be always greater than 80 %. Saharan mineral dust shows higher particle linear depolarization ratios due to the non-spherical particle shape ($\delta_{p(532)} \approx 0.3$; *Freudenthaler et al.*, 2009; *Tesche et al.*, 2009b; *Groß et al.*, 2011b). This ratio remains unchanged after long-range transport across the North Atlantic Ocean (*Groß et al.*, 2015). Thus, $\delta_{p(532)}$ represents a good proxy to differentiate between mineral dust and marine aerosol in WALES lidar profiles during NARVAL-II as other aerosol species, like volcanic ash or particles from biomass burning processes, are not expected in the measurement region. In this way, a detection-scheme is applied to the data for the detection of three different aerosol regimes:

1. **pure mineral dust regime:** $\delta_{p(532)} \geq 0.26$
2. **pure marine aerosol regime:** $\delta_{p(532)} \leq 0.04$
3. **mixed regime:** marine aerosol mixed with mineral dust $0.04 < \delta_{p(532)} < 0.26$

Additionally, aerosol-free regions in the lidar measurements can be determined via filtering for regions with no evident particle backscattering ($\boldsymbol{R_{532}} < 1.2$). Using this criteria an aerosol mask which serves as libRadtran input can be generated.

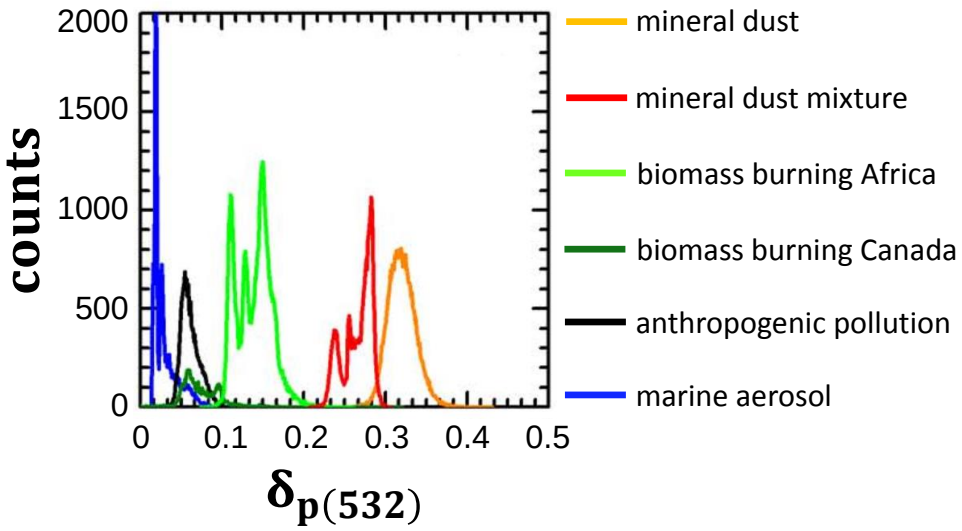

Figure 2.11: Absolute frequency distribution of lidar-derived particle linear depolarization ratios $\delta_{p(532)}$ for different aerosol types during the field campaigns LACE[1], SAMUM-1 and -2 and EUCAARI-LONGREX[2]. Adapted from *Groß et al.* (2013).

Conversion of aerosol extinction coefficients to aerosol mass concentrations

For radiative transfer calculations with libRadtran, particle mass concentrations of the different aerosol species in the three detected aerosol regimes have to be determined. A schematic overview of the procedure is given in Figure 2.12. Therefore, measurements of aerosol extinction coefficients from WALES are converted to aerosol mass concentrations.

According to *Groß et al.* (2016), conversion factors can be used to convert measured $\alpha_{p(532)}$ to mineral dust and marine aerosol concentrations per unit volume ($c_{v(dust)}, c_{v(marine)}$). These

[1] Lindenberg Aerosol Characterization Experiment, Germany (1998; *Ansmann et al.*, 2002)
[2] European integrated project on Aerosol Cloud Climate and Air Quality Interactions, Long-range experiment (2008; *Kulmala et al.*, 2009)

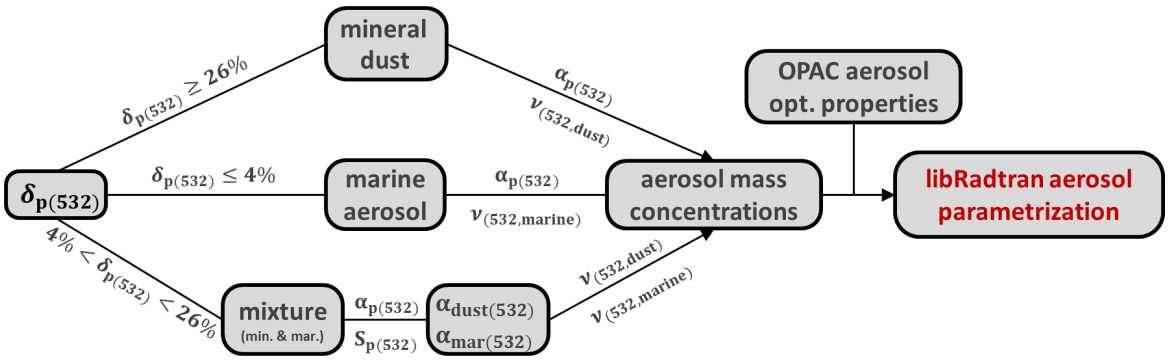

Figure 2.12: Schematic overview of the developed libRadtran aerosol parametrization with lidar data.

factors are taken from results of the AERONET (AErosol RObotik NETwork) inversion algorithm presented by *Mamouri and Ansmann* (2016) and are given in *Groß et al.* (2016). For long-range-transported Saharan dust a conversion factor of $\nu_{dust(532)} = c_{v(dust)}/\alpha_{dust(532)} = 0.65 \cdot 10^{-6}$ m is derived. Due to the similar size distribution of mineral dust and marine aerosols, the AERONET inversion deduced a similar conversion factor of $\nu_{marine(532)} = c_{v(marine)}/\alpha_{marine(532)} = 0.66 \cdot 10^{-6}$ m for marine aerosol. The respective aerosol mass concentrations $c_{m(dust)}$ and $c_{m(marine)}$ can be calculated by multiplication with the typical particle densities of mineral dust ($\rho_{dust} = 2.5\,\mathrm{g\,cm^{-3}}$) and marine aerosol ($\rho_{marine} = 2.2\,\mathrm{g\,cm^{-3}}$). The assumption of those particle densities is based on a study by (*Kaaden et al.*, 2009) who showed that SAL-aerosol is a mixture of mineral dust particles together with sulfate particles.

This method allows the characterization of aerosol mass concentrations in the pure mineral dust regime (regimes (1) and (2)). However, particle mass concentrations also have to be derived in mixed aerosol regimes, i.e. where mineral dust aerosol settles to lower atmospheric levels and is mixed with marine aerosol. Therefore, the contribution of mineral dust aerosol to the total aerosol mixture has to be determined. The aerosol extinction coefficient at 532 nm of a marine - mineral dust aerosol mixture $\alpha_{p(532),mix}$ can be written as,

$$\begin{aligned} \alpha_{p(532),mix} &= \alpha_{p(532),dust} + \alpha_{p(532),marine} \\ &= (1-x)\ \alpha_{p(532),mix} + x\alpha_{p(532),mix}, \end{aligned} \tag{2.40}$$

with $\alpha_{p(532),marine}$ and $\alpha_{p(532),dust}$ being the marine aerosol and mineral dust particle extinction coefficient at 532 nm and $x = \alpha_{p(532),dust}/\alpha_{p(532),mix}$. Using the known lidar ratios of marine and mineral dust aerosol at 532 nm ($S_{p(532),marine} \simeq 18$ sr and $S_{p(532),dust} \simeq 47$ sr; *Burton et al.*, 2012; *Groß et al.*, 2013) and following the methods described in *Tesche et al.* (2009a) and *Groß et al.* (2011a) one can calculate the fraction x of dust contributing to the total particle extinction coefficient of the mixture,

$$x = \frac{D_{marine}}{D_{marine} + D_{dust}} \tag{2.41}$$

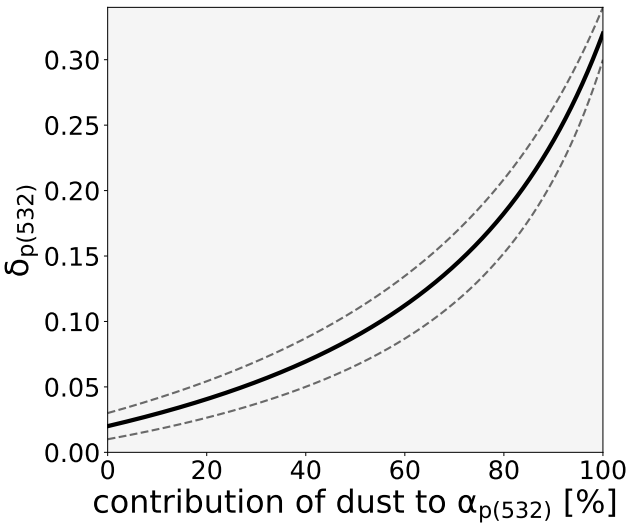

Figure 2.13: Contribution of mineral dust to total particle extinction $\alpha_{p(532)}$ for an aerosol mixture containing mineral dust and marine aerosol. The solid line marks the mean of the retrieval. The dashed line mark the uncertainties of the input parameters as derived by *Groß et al.* (2013).

with the coefficients D_{dust} and D_{marine}:

$$\begin{aligned} D_{dust} &:= \frac{\delta_{p(532),dust} - \delta_{p(532),mix}}{S_{p(532),dust}(1 + \delta_{p(532),dust})} \\ D_{marine} &:= \frac{\delta_{p(532),mix} - \delta_{p(532),marine}}{S_{p(532),marine}(1 + \delta_{p(532),marine})} \end{aligned} \tag{2.42}$$

Finally, Eq. (Equation 2.41), $\nu_{dust(532)}$ and $\nu_{marine(532)}$ as well as ρ_{dust} and ρ_{marine} are used to calculate mineral dust and marine aerosol particle mass concentrations in mixed aerosol regimes.

2.4.3 OPAC aerosol microphysical properties

In a last step, the calculated aerosol mass concentrations are related to typical aerosol optical properties that are needed for radiative transfer calculations, i.e. phase function $\boldsymbol{P}(\boldsymbol{\Theta})$ and single scattering albedo ω_0. Those properties are commonly modeled using size distributions and spectral refractive indices of the desired aerosol species. Model-assumptions always represent some source of uncertainty. For example, *Yi et al.* (2011) showed that different representations of particle shapes result in a change of $\boldsymbol{P}(\boldsymbol{\Theta})$ and can cause up to 30 % difference in the dust radiative forcing at top of the atmosphere (TOA). To minimize errors

resulting from wavelength-interpolations *Hess et al.* (1998) established the readily available spectrally resolved OPAC database (Optical properties of Aerosols and Clouds) which includes modeled information on the above mentioned aerosol optical properties for 61 wavelengths in the spectral range from $0.25 - 40\,\mu$m for various aerosol species. OPAC is a widely used data base in aerosol models and retrievals (e.g. *Kim et al.*, 2004; *Liu et al.*, 2004; *Patadia et al.*, 2009) as well as general circulation and climate models for calculations in both the short-wave and long-wave spectra. Thus, it is an appropriate tool to link lidar derived aerosol mass concentrations to aerosol optical properties in the classified aerosol regimes.

OPAC sea salt and water-soluble particle microphysical properties are modeled under the assumption of spherical particles using Mie-theory (*Mie*, 1908). The assumption of spherical particles is legitimate for radiative transfer simulations in the period of NARVAL-II since no dry and aspherical marine aerosol particles are expected at observed relative humidities of greater 80 % inside the derived marine aerosol regimes (*Murayama et al.*, 1999; *Sakai et al.*, 2010). Thus, a humidity dependent marine aerosol composition which refers to WALES measurements of water vapor mixing ratios together with dropsonde-derived temperature profiles is used in this study (see Table 2.4).

Mineral dust particles however, are characterized by highly irregular shapes (*Falkovich et al.*, 2001; *Kandler et al.*, 2011). Hence, an assumption of spherical mineral dust particles in radiative transfer models using Mie-theory is inappropriate and may lead to wrong results. Especially if particles are larger than the transmitted wavelength (which is the case for most backscatter lidar systems) phase functions of aspherical particles are characterized by an increased amount of sideward but a reduced amount of backward scattering compared to spherical particles (*Koepke and Hess*, 1988; *Gobbi et al.*, 2002; *Nousiainen*, 2009; *Wiegner et al.*, 2009; *Gasteiger et al.*, 2011; *Sakai et al.*, 2014). For this reason mineral dust particle microphysical properties were updated in the latest OPAC version (v4.0; *Gasteiger et al.*, 2011; *Koepke et al.*, 2015) and are now calculated by means of the T-matrix method (*Waterman*, 1971) under assumptions of an aspect ratio distribution for prolate spheroids observed during the Saharan mineral dust experiments SAMUM-1 and SAMUM-2 (*Kandler et al.*, 2009, 2011). Several studies have shown that T-matrix theory substantially improves the agreement between measured and modeled aerosol optical properties of aspherical mineral dust particles (*Mishchenko et al.*, 1997; *Kahnert et al.*, 2005; *Gasteiger et al.*, 2011) and are thus motivating its use in this study.

Results obtained from measurements during the SALTRACE field campaign (*Weinzierl et al.*, 2017) showed that the size distribution of long-range-transported mineral dust does not change significantly compared to the distributions measured at source regions. Gravitational settling processes of large particles with sizes of several microns in the course of the SAL-transatlantic transport are of a smaller magnitude than expected from Stokes gravitational settling calculations. *Denjean et al.* (2015) also found that the chemical composition and hygroscopicity of long-range-transported mineral dust compared to source regions remains unaltered. Thus, a mixture proposed by *Hess et al.* (1998), which consists of four OPAC v4.0-components for desert aerosol optical properties is assumed in this work (see Table 2.4).

Table 2.4: OPAC particle type composition of lidar derived aerosol regimes used in the radiative transfer simulations. Shown percentages refer to mass mixing ratios.

Regime	OPAC component	Mix. ratio
marine aerosol	sea salt (acc. mode)	92.8 %
	water-soluble	5.8 %
	sea salt (coarse mode)	1.4 %
mineral dust	Mineral (acc. mode)	74.7 %
	Mineral (coarse mode)	20.2 %
	Mineral (nuc. mode)	3.3 %
	Water-soluble	1.8 %

Chapter 3

Results

This chapter starts with a characterization of the observed SALs during the NARVAL-II campaign (Section 3.1). First, their optical and microphysical properties as derived from lidar are presented (Section 3.1.1). Second, water vapor distributions of lidar measurements in SAL-regions are shown and enhanced concentrations of water vapor inside SALs are pointed out (Section 3.1.2). The section continues by taking a closer look at the SAL-event on RF6 on 19 Aug (Section 3.1.3). This HALO research flight led over both dust-laden and dust-free trade wind regimes and therefore enables an investigation of the meteorological aspects in both regimes. Furthermore, the occurrence of enhanced concentrations of SAL-water vapor is investigated in more detail. The chapter continues with an investigation of radiative transfer in long-range-transported SALs in Section 3.2. By presenting three cases studies, the roles of dust aerosols and water vapor for atmospheric heating in SAL-influenced regions over the North Atlantic Ocean are examined (Section 3.2.1 & Section 3.2.2). Moreover, the dust radiative effects on surface and top of the atmosphere are quantified (3.2.3).

Major parts of the presented results are published in the peer-reviewed articles *Gutleben et al.* (2019a), *Gutleben et al.* (2019b) and (*Gutleben et al.*, 2020).

3.1 Characteristics of long-range-transported Saharan air layers

As already mentioned in Section 2.3, measurements over long-range-transported SALs were performed during four research flights of NARVAL-II (i.e. RF2, RF3, RF4 and RF6). To verify the Saharan origin of the layers, backward trajectories using the HYSPLIT model with NCEP GDAS meteorological input data were calculated and are shown in Figure 3.1. Starting times and locations were chosen to match the center of the detected layers in the lidar profiles and the reliability of the calculations was checked by a slight modification of them (not shown). The calculations indicate that the observed dust layers traveled for 5 to 10 days from the mountainous Adrar-Hoggar-Aïr region in the central Sahara to the measurement location over the western North Atlantic Ocean upstream of Barbados. In contrast to the dust layer observed

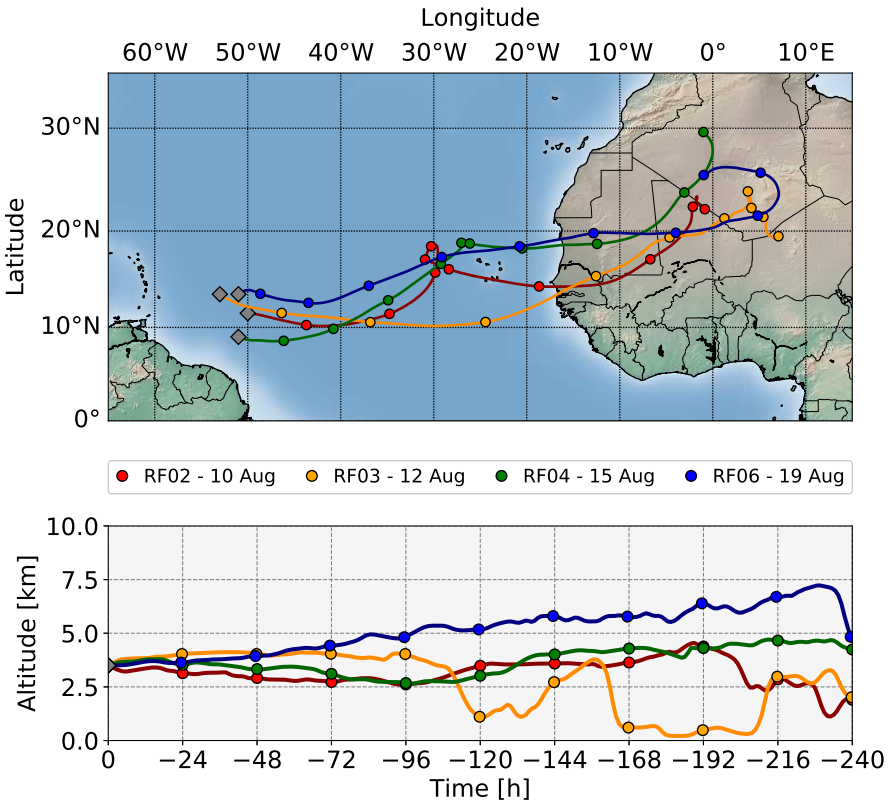

Figure 3.1: 10-day backward trajectories with starting points at the center of the respective SALs for the four NARVAL-II research flights leading over Saharan dust-laden trade wind regions (RF2, RF3, RF4 and RF6).

in the framework of RF3, which traveled for only 3.5 days from the West African coast to the measurement region, the transatlantic transport for all the other dust layers took at least 5.5 days.

3.1.1 Optical and macrophysical properties

An overview of the optical as well as macrophysical characteristics of the four observed SALs as determined from WALES measurements (i.e. $\boldsymbol{R_{532}}$, $\delta_{p(532)}$ as well as the SAL vertical extent Δz_{SAL} and optical depth $\tau_{SAL(532)}$) is presented in Figure 3.2. Departure and landing times in the morning and evening hours as well as the durations (approx. 8 h) were very similar for all four flights (see Table 2.2).

During the whole flight on 10 August (RF2), a thin SAL ranging from 2.5-5.0 km altitude was observed ($\Delta z_{SAL} < 2$ km). An average value of 30 % for $\delta_{p(532)}$ clearly classifies this

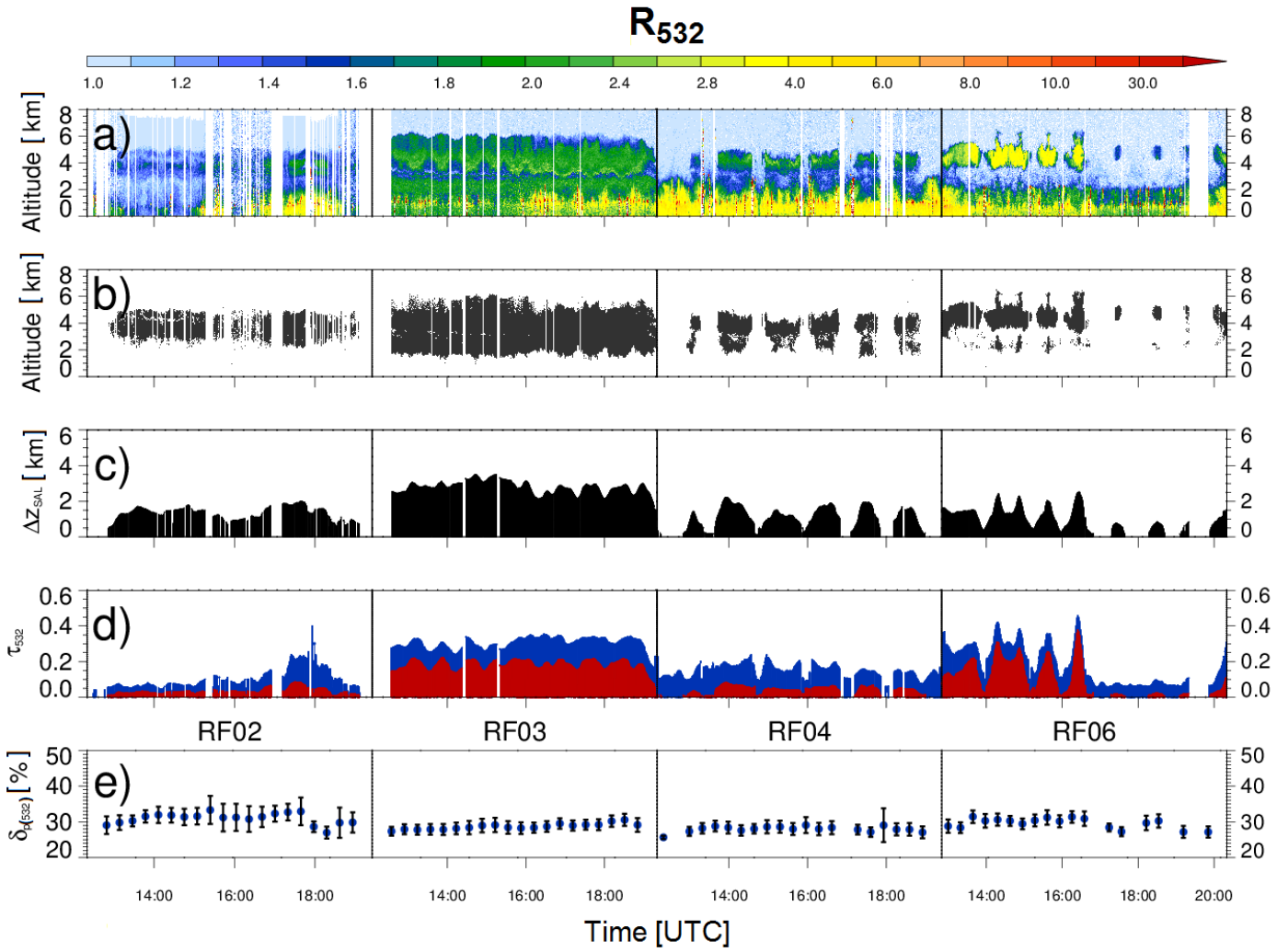

Figure 3.2: Overview of the four NARVAL-II research flights leading over Saharan-dust-laden trade wind regions. (a) Cross sections of measured backscatter ratio at 532 nm ($\boldsymbol{R_{532}}$) and (b) applied mineral dust mask. (c) The 10 min boxcar average of the calculated dust layer vertical extent Δz_{SAL}. (d) The 10 min boxcar average of the derived total aerosol optical depth from aircraft to ground level $\tau_{tot(532)}$ (blue) and aerosol layer optical depth $\tau_{SAL(532)}$ (red). (e) Mean values and standard deviations of the measured 10 min averaged SAL particle linear depolarization ratio ($\delta_{p(532)}$).

elevated layer as a mineral dust layer. When applying a mineral dust mask, one can identify a layer of pure mineral dust (SAL) in altitudes ranging from 2.5 km to 5.0 km. The aerosol optical depth at 532 nm of the SAL ($\tau_{SAL(532)}$) took values around 0.15. This equals on average approximately 35 % of the total column aerosol optical depth at 532 nm ($\tau_{tot(532)}$) during this RF. Unfortunately, bright and strongly reflecting clouds in the lidar field of view caused the safety circuit of the detector unit to shut down the device now and then. This caused some gaps in the continuous lidar data set.

In contrast to RF2, a vertically and optically thick dust layer was detected during the whole RF3 on 12 August. $\delta_{p(532)}$ of this layer ranged from 28-30 %, thus confirming the presence of Saharan mineral dust. The layer had a maximum vertical extent of approximately 4 km (extended from approx. 2 km to 6 km height), was characterized by aerosol optical depths (532 nm) of around 0.2 and contributed on average with 60 % to $\tau_{tot(532)}$ during that flight.

While RF2 and RF3 were designed for measurements solely in dust-laden regions, RF4 and RF6 on 15 and 19 August were planned for measurements in both dust-laden and dust-free regions within the very same research flight. Flight tracks were chosen to cross dust-gradients frequently, resulting in multiple flight segments of dust and no dust along the flight track. Elevated aerosol layers showed mean $\delta_{p(532)}$ of 30 % and could therefore be identified as SALs. While the SAL during RF4 ranged on average from 2.5-4.5 km, it reached higher to almost 6 km altitude during RF6. With $\tau_{SAL(532)}$ taking values around 0.1 the dust layer during RF4 contributed on average 25 % to $\tau_{tot(532)}$. $\tau_{SAL(532)}$ during RF6 took higher values of up to 0.4 and showed a mean contribution of 51 % to $\tau_{tot(532)}$.

3.1.2 Enhanced concentrations of water vapor inside Saharan air layers

During all four flights, WALES DIAL measurements indicated enhanced concentrations of water vapor inside the SALs compared to the surrounding dry free troposphere. This is highlighted in Figure 3.3.

The distribution of measured $\delta_{p(532)}$ during all research flights in dust-laden regions (Figure 3.3 (a)) confirms once more that all observed SALs have been elevated in the height interval from 2 to 5 km. In contrast to the SALs, small values of $\delta_{p(532)}$ are found in the MBLs, which ranged up to about 1.5 km altitude during all flights. $\delta_{p(532)}$ at these levels points towards an aerosol mixture of marine and mineral dust particles since most values are in the range from $0.02 < \delta_{p(532)} < 0.15$. At levels higher than approximately 5 km $\delta_{p(532)}$ drops to almost zero - an indication for an almost aerosol-free atmosphere above the SAL since also $\boldsymbol{R_{532}}$ decreases to approximately 1 at these levels (not shown).

The measured water vapor distribution (Figure 3.3 (b)) for all research flights in dust-laden regions highlights that the height interval from 2 km to 5 km is characterized by water vapor mass mixing ratios around 4 g kg^{-1}. This is also indicated by the joint distribution of both variables in (Figure 3.3 (c)). It clearly shows the correlation of enhanced water vapor mass mixing ratios and SALs since it peaks at mixing ratios of 4 g kg^{-1} and typical values of $\delta_{p(532)}$ for mineral dust around 30 %. Highest values of r_m during NARVAL-II are found inside the

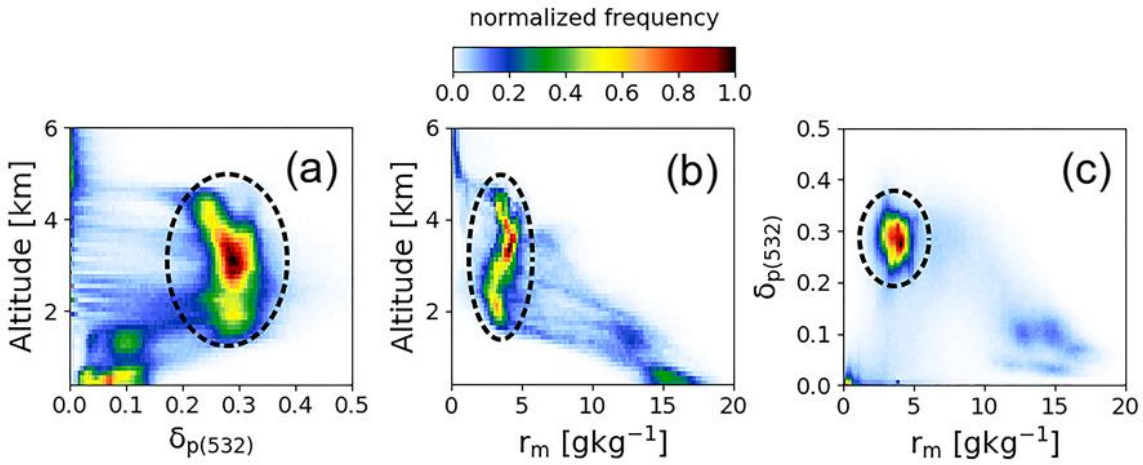

Figure 3.3: The 2-D histograms showing the distribution of measured 532 nm particle linear depolarization ratios ($\delta_{p(532)}$, (a)) and water vapor mass mixing ratios (r_m, (b)) as a function of altitude during the four NARVAL-II research flights leading over elevated SALs. (c) The 2-D histogram of r_m as a function of $\delta_{p(532)}$ during the four NARVAL-II research flights leading over elevated SALs. The distributions are normed to the maximum bin count in each individual histogram. Dashed regions indicate signatures of SALs.

MBL and ranged from 14 g kg^{-1} to 18 g kg^{-1}.

3.1.3 Taking a closer look: the dust-event on 19 Aug 2016

The following section takes a closer look at meteorological characteristics and the enhanced r_m of long-range-transported SALs by analyzing the dust-event during RF6 including in detail. By means of backward-trajectories, radiosonde and satellite data, the question where the moisture stems from is also discussed.

RF6 on 19 August 2016 took place in the area between 48°W to 60°W and 13°N to 19°N (Figure 3.4). The ITCZ and associated deep convection were located 550 km south of the flight track at around 10°N. RF6 crossed a sharp gradient between a dust-laden and a clear region in an altitude of approximately 8.25 km with about one half of the measurement time in dust-laden and the other half in dust-free regions. The circular patterns of the flight track were flown for dropsonde-based divergence measurements (*Bony and Stevens*, 2019). While the first pair of circles was performed over a heavily dust-laden region in the southern part of the flight track, the second pair was performed in the northern part over an almost dust-free region. This is also seen in MODIS aerosol optical depth imagery at 13:40 UTC in Figure Figure 3.4 (right) where the region around the southern circle shows a maximum aerosol optical depth greater 0.4. The HALO flight path during the northern circle did just shortly touch a SAL-impacted airmass in the Northwest where τ took values around 0.2.

Measured cross sections of $\boldsymbol{R_{532}}$ and the derived mineral dust mask from WALES (shown in

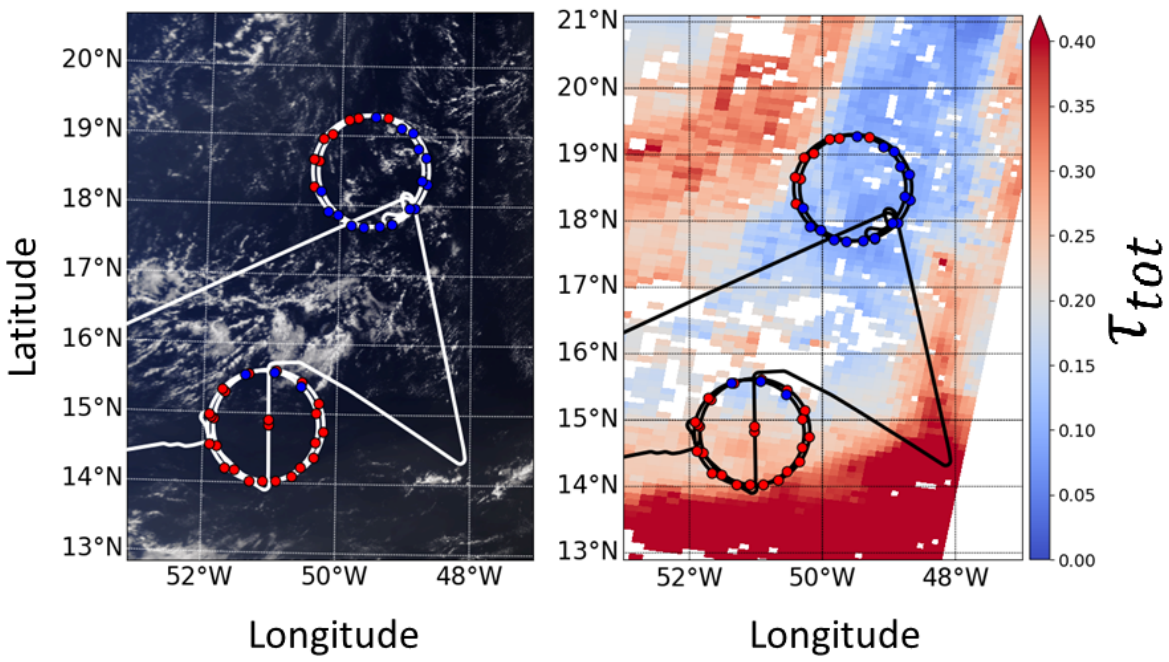

Figure 3.4: Flight track of RF6 on 19 Aug 2016 on top of the Terra-MODIS true color image (left) and the MODIS aerosol optical depth (τ_{tot}) product (right) at 13:40 UTC. Launched dropsondes are marked by colored dots (red dots: dropsondes launched in mineral dust-laden regions, blue: dropsondes launched in dust-free regions).

Figure 3.2 (a, RF6) and (b, RF6)) affirm the measurement situation and indicate pronounced elevated mineral dust layers ranging from 2.5-5.0 km altitude, horizontally alternating with dust-free profile regions.

Dropsonde analysis

During RF6 dropsondes were launched frequently along the flight tracks and can therefore be used to compare measured vertical profiles of meteorological parameters in dust-laden to those measured in dust-free regions. For this purpose mean profiles of potential temperature θ, relative humidity and water vapor mass mixing ratio (RH, r_m) as well as wind speed and direction (u, $wdir$) of all dropsonde-measurements in the respective dust-laden and dust-free regions are compared in Figure 3.5 (I.(b-d), II.(b-d) and III.(a-d)). Additionally, lidar-derived $\delta_{p(532)}$ is analyzed for both regimes (Figure 3.5, I.a and II.a).

Dropsonde measurements indicate that inside the SAL-region a three-layer structure is present: 1) the MBL, reaching up to approximately 1.3 km height. $\delta_{p(532)}$ smaller 10 % indicates

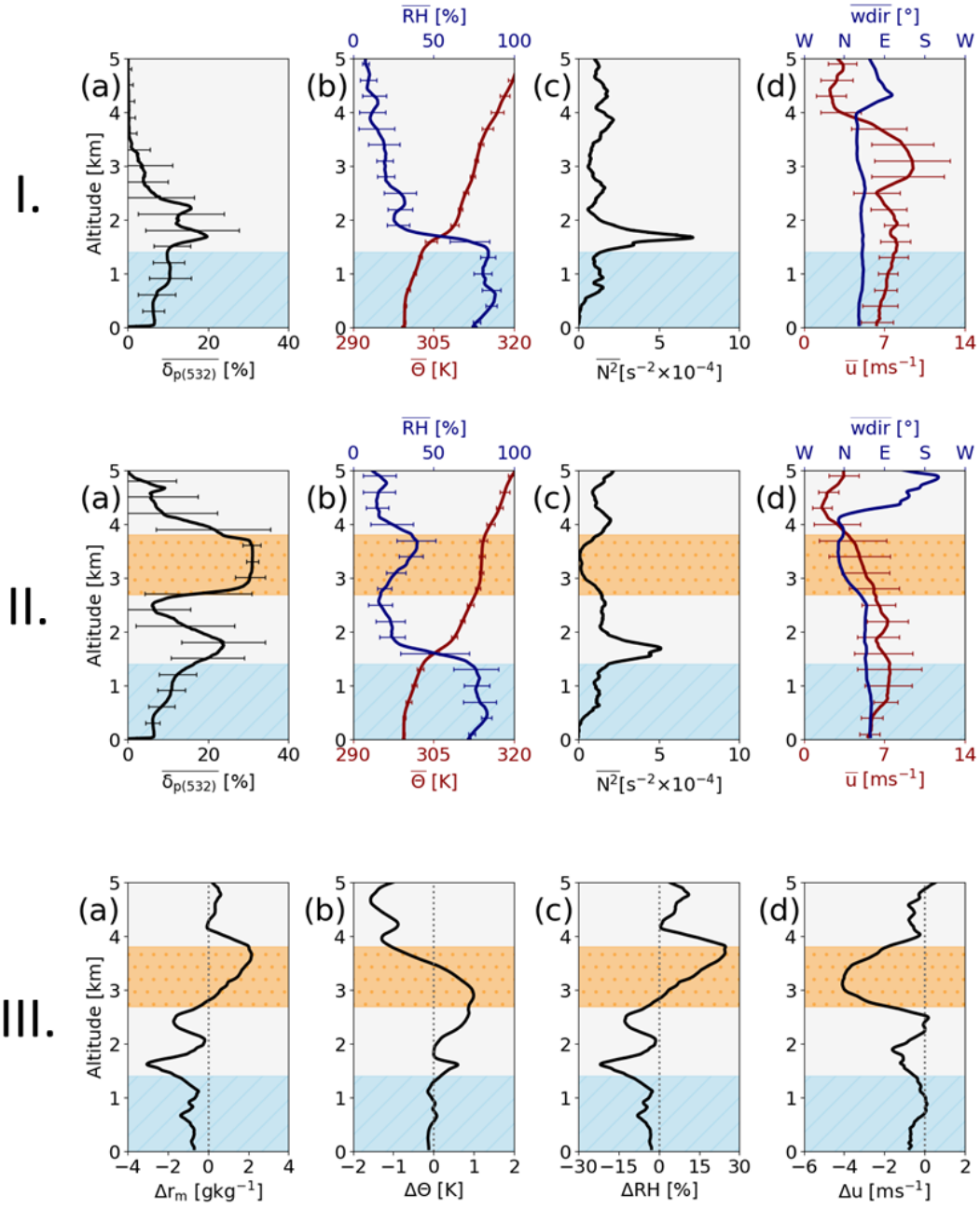

Figure 3.5: Mean vertical WALES lidar profiles of $\delta_{p(532)}$ and mean vertical dropsonde profiles of relative humidity (RH), potential temperature (Θ), squared Brunt-Väisälä frequency $N^2 = \frac{g}{\Theta}\frac{\partial \Theta}{\partial z}$ as well as wind speed (u) and direction ($wdir$) in dust-free (I.(a-d)) and dust-laden (II.(a-d)) regions during RF6 on 19 Aug 2016 (horizontal bars indicate standard deviations). III.(a-d): Differences in water vapor mass mixing ratio (r_m), potential temperature, relative humidity and wind speed between the two regions. Shaded regions mark the marine boundary layer (blue) and the Saharan air layer (orange).

that marine aerosols are the dominant contributor to the aerosol composition of the MBL; 2) a transition or mixed layer extending from the MBL-top to 2.8 km altitude with varying values of $\delta_{p(532)}$ (10 % $< \delta_{p(532)} <$ 20 %); and 3) the elevated SAL, with typical $\delta_{p(532)}$ for long-range-transported Saharan dust ($\delta_{p(532)}$ ∼30 %) ranging from 2.8 km to 3.8 km height. The mean profile of $\delta_{p(532)}$ inside the MBL has a similar shape in the dust-free and dust-laden regions. However, no SAL-signature is detected.

Both the dust-laden and the dust-free region clearly indicate the so-called trade wind inversion (TWI) in an altitude range from 1.5 km to 1.8 km height capping the moist MBL. It is caused by the large-scale subsiding flows of the Hadley cell and Walker circulation. The TWI is characterized by a rapid temperature decrease of about 4 K within 400 m (not shown) and a strong hydrolapse (RH drops from >80 % to ∼30 %). In both regimes the MBL itself can be divided into a sub-cloud layer which extends from the ocean surface to 0.5-0.7 km and a cloud layer which extends from the sub-cloud layer top to the TWI (0.5 - 1.8 km). Those two regions can be identified in profiles of Θ and humidity. Whereas the sub-cloud layer is well mixed (Θ = const., r_m = const.), the cloud layer shows a conditionally unstable lapse rate of 5-7 K km^{-1} (saturated air parcels are unstable to vertical displacement). The MBL of both regimes is dominated by north-easterly winds with speeds around 7 m s^{-1}. In dust-laden regions wind speeds in SAL-altitudes are by 4 m s^{-1} lower than in the dust-free regions. This suggests that the SAL represents a decoupled layer which penetrates into the trade-wind regime.

Besides the WALES measurements also dropsonde measurements indicate enhanced amounts of water vapor inside the long-range-transported SAL. Relative humidity and water vapor mass mixing ratio show an increase of 2 g kg^{-1} in SAL regions compared to the dust-free trade wind region. An in-depth investigation of the observed SAL water vapor during RF6 and an examination of its origin is presented in the following Section 3.1.3.

For a better visualization of atmospheric stability the squared Brunt Väisälä frequency $N^2 = \frac{g}{\Theta}\frac{d\Theta}{dz}$, with g being the gravity of the Earth, is shown. N^2 shows regions of high atmospheric stability and thus strong restoring forces for a vertical air parcel displacement at the inversion altitudes. Enhanced atmospheric stability is found at the TWI for both regimes. At higher altitudes N^2-profiles look different. In dust-laden regions the lower and upper boundary of the SAL are characterized by two additional inversions. These inversions have already been found in the sixties (*Lilly*, 1968). The inversion at the SAL-base is caused by the strong vertical gradients of temperature between the hot SAL-base and the subjacent cooler marine air below (*Prospero and Carlson*, 1972; *Dunion and Velden*, 2004) and the upper inversion is caused by the predominant large-scale subtropical subsidence in the upper troposphere (*Gamo*, 1996). Inside the layer N^2 is almost zero - indicating a well mixed SAL-regime. Furthermore, Θ points towards a neutral stratification in the interior of the SAL since it does not change with altitude. Altogether, a total of three prominent inversion layers could counteract convective development in dust-laden regions, whereas in dust-free regions just the trade wind inversion is present.

Retracing the water vapor inside the Saharan air layer

Figure 3.6 shows the WALES DIAL and backscatter measurements of the moist, elevated, and long-range-transported SAL on 19 August 2016. The 2-D cross section of backscatter ratio $\boldsymbol{R_{532}}$ measured during this research flight (Figure 3.6 (c)) shows an elevated layer of enhanced particle backscatter ($\boldsymbol{R_{532}} \approx 3.0$) ranging from 2.5 km to 5.0 km altitude. In those altitudes $\delta_{p(532)}$ takes typical values for mineral dust around 0.3 (Figure 3.6 (b)) and thus verifies that the layer is a SAL (Figure 3.6 (d)). The SAL aerosol optical depth at 532 nm is approximately 0.3 (not shown). Homogeneously distributed water vapor mass mixing ratios around 4 g kg^{-1} are observed in SAL altitudes (Figure 3.6 (a)). The profile of r_m follows the SAL signature in the $\boldsymbol{R_{532}}$ profile. It indicates that the SAL is representing a relatively moist layer compared to adjacent atmospheric levels above and below where r_m is by approximately 2 g kg^{-1} smaller. Inside the MBL, which extends from the ocean surface to approximately 1.5 km altitude, water vapor mixing ratios of up to 15 g kg^{-1} are measured.

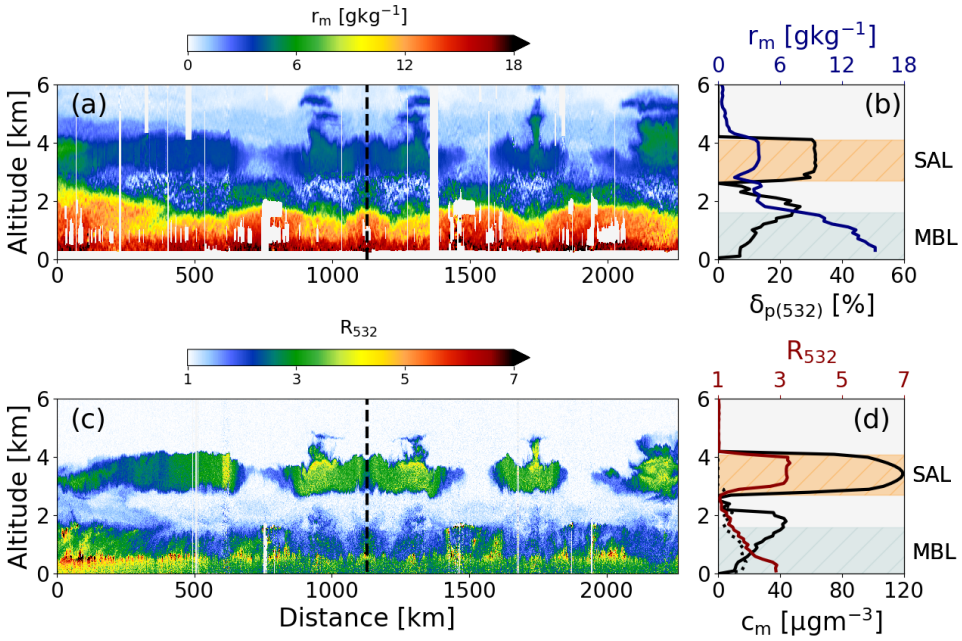

Figure 3.6: (a) The cross section of water vapor mass mixing ratio r_m measured during the research flight on 19 August 2016. (b) The vertical profiles of water vapor mass mixing ratio r_m and particle linear depolarization ratio $\delta_{p(532)}$ at the indicated measurement location (dashed lines in a and c). Hatched areas indicate the Saharan air layer (SAL, orange) and the marine boundary layer (MBL, light green). (c) The cross section of lidar backscatter ratio $\boldsymbol{R_{532}}$ measured during the research flight on 19 August 2016. (d) The vertical profiles of $\boldsymbol{R_{532}}$ as well as derived mineral dust (solid) and marine aerosol mass concentrations (dashed) at the indicated measurement location (dashed lines in a and c)

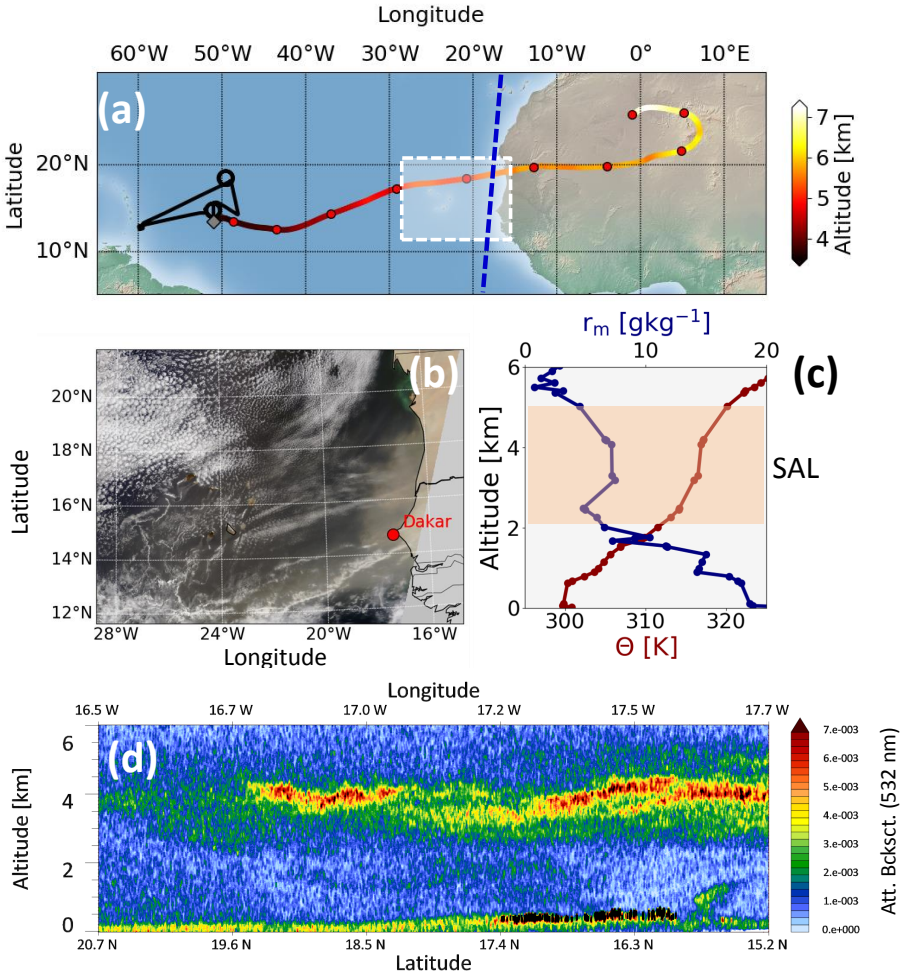

Figure 3.7: (a) The 10-day backward trajectory with the starting point being located inside the observed Saharan air layer (SAL; 19 August 2016 at 14:30 UTC; 14°N; 51.5°W; 3.5 km altitude). Colors mark the altitude of the trajectory. The black line in (a) marks the HALO research flight track on 19 August 2016. The white box in (a) indicates the field of view of the MODIS (Moderate-resolution Imaging Spectroradiometer) real color image illustrated in (b), which shows the dust outbreak region over Dakar (image taken on 15 August 2016 at 12:25 UTC). The dashed blue line in (a) marks the ground track of the smoothed 2-D CALIOP (Cloud-Aerosol LIdar with Orthogonal Polarization) 532 nm attenuated backscatter cross section of the observed SAL on 15 August 2016 around 03:00 UTC that is shown in (d). (c) Profiles of potential temperature Θ and water vapor mass mixing ratio r_m from radiosonde measurements over Dakar on 15 August 2016 at 12:00 UTC. The orange-colored region marks the observed SAL.

WALES lidar cross sections also show that the SAL is well separated from the MBL by an almost aerosol-free airmass. $\delta_{p(532)}$ inside the MBL takes values around 0.2 - an indicator for a mixed MBL containing settling mineral dust and marine aerosol particles at lowest atmospheric levels. When looking at the derived profiles of marine and mineral dust aerosol mass concentration (c_m) highest concentrations of mineral dust can be found at the center of the SAL reaching values of up to 120 g m^{-3}. At lower atmospheric levels the aerosol profile is composed of an aerosol mixture consisting of dust aerosol (c_m > 40 g m^3) and marine aerosol (c_m > 20 g m^{-3}) with highest concentrations of marine aerosol at near-surface levels. In SAL altitudes no marine aerosol is detected anymore.

Calculated HYSPLIT backward trajectories with NCEP GDAS input data indicate that the SAL traveled for about 10 days from the Saharan desert to the measurement location in the southern part of the flight track (Figure 3.7 (a)). The center of the SAL descended by more than 3 km (from 7 to 3.5 km). The huge dust-outbreak off-coast Senegal is also seen in MODIS and CALIOP satellite observations on 15 August 2016 (Figure 3.7 (b & d)). Enhanced backscatter in CALIOP lidar measurements indicate that the SAL was located in altitudes ranging from approximately 2 to 5 km altitude during the outbreak. Operationally launched radiosonde measurements on the same day over the city of Dakar (Senegal; Figure 3.7 (c)) reveal that the SAL already showed enhanced r_m of up to 7 g kg^{-1} at the beginning of its long-range transport. Measured r_m inside the SAL near the Caribbean islands (4 g kg^{-1}) is lower than in Dakar.

3.2 Radiative transfer in long-range-transported Saharan air layers

The following Section focuses on the impacts caused by both SAL water vapor and SAL aerosol particles on radiative transfer. The effects that SAL water vapor and SAL-aerosols have on atmospheric heating and the radiation budget at surface level and top of the atmosphere are therefore investigated in detail. In order to do that, libRadtran radiative transfer calculations for three typical cloudless 5 min-lidar cross sections during the NARVAL-II-research flights on 12 and 19 August 2016 (RF3 & RF6) are presented and discussed.

3.2.1 Case studies for radiative transfer calculations

On 12 August dust layers covered the whole research area. This is also seen in measured MODIS total column aerosol optical depth τ_{tot} during that day which took values around 0.3 along the whole flight track (Figure 3.8). In contrast, the research flight on 19 August led over trade wind regions comprising elevated mineral dust layers (τ_{tot} >0.3) as well as regions free of mineral dust and is therefore suitable for a comparison of radiative effects in SAL-influenced regions and SAL-free regions.

Figure 3.9 shows the three cloudless 5 min-lidar cross sections observed during these two research flights that are used for radiative transfer calculations in this work. While the first

case represents a SAL-free scenario with some residual mineral dust at low atmospheric levels, the other two cases are both characterized by a long-range-transported SAL. All the three selected cross sections are of approximately 50 km length and described in the following:

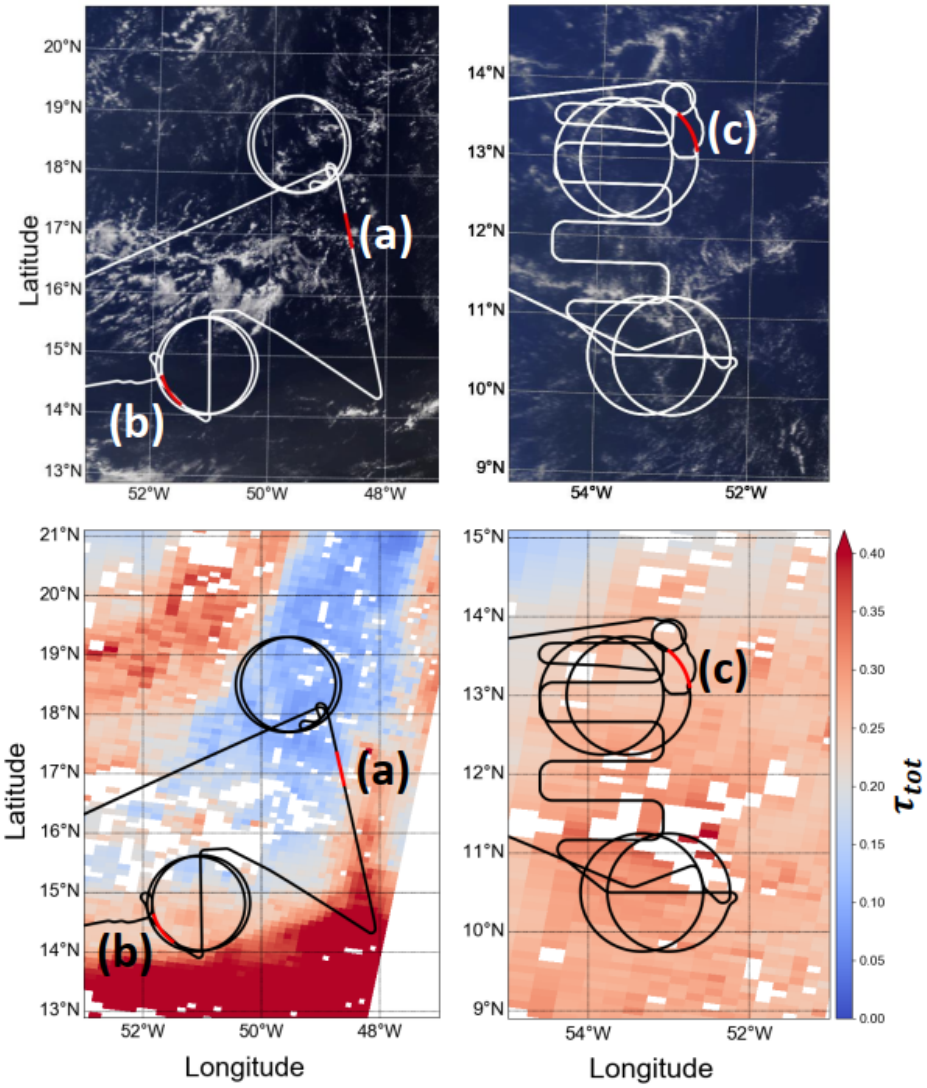

Figure 3.8: Flight tracks of the RF3 and RF6 conducted on 12 (right) and 19 (left) August 2016 on top of images showing MODIS true color (top) and total column aerosol optical depth (τ_{tot}, bottom) around 13:40 UTC. Red lines and labels indicate the discussed flight segments (cases (a), (b) and (c)).

(a) *SAL-free case - 19 Aug 2016 (16:51-16:56 UTC):*
This case represents a typical SAL-free measurement segment during NARVAL-II. Lidar profiles of $\boldsymbol{R_{532}}$ and $\delta_{p(532)}$ show no dust-signatures in altitudes greater 3 km. In the MBL both marine and mineral dust aerosol particles coexist (settling dust particles) and a maximum aerosol extinction coefficient of 0.03 km^{-1} was measured inside the MBL. $\delta_{p(532)}$ ranges from roughly 0.05 to 0.25 and derived aerosol mass concentrations of both marine and mineral dust aerosol reach maximum values of approximately 30 $\mu g\, m^{-3}$.

(b) *Elevated SAL - 19 Aug 2016 (14:26 - 14:31 UTC):*
The second case represents a scenario with a detected elevated and long-range-transported SAL extending from 3 - 4 km altitude. The SAL shows increased backscatter ratios around 3 and high particle linear depolarization ratios of ∼0.3. $\delta_{p(532)}$ and $\boldsymbol{R_{(532)}}$ profiles feature sharp gradients to the above free-troposphere and to lower atmospheric levels. The SAL itself is associated with evenly distributed mineral dust mass concentrations of approximately 120 $\mu g\, m^{-3}$ and aerosol extinction coefficients around 0.07 km^{-1}. Marine aerosols are mainly confined to the MBL which extends from 0.0 - 1.6 km altitude. Similar to case (a) the aerosol composition within the MBL is not exclusively characterized by marine aerosols but also contains portions of mineral dust aerosols. An intermediate layer showing small values of $\delta_{p(532)}$, $c_{m(dust)}$ and $\boldsymbol{R_{(532)}}$ is located in between the MBL and the SAL and ranges from 1.6 - 2.8 km altitude.

(c) *Thick SAL - 12 Aug 2016 (14:26 - 14:31 UTC):*
The third scenario represents the thickest SAL that has been observed during the whole NARVAL-II campaign. Measured $\delta_{p(532)}$ of around 0.3 clearly indicates the presence of Saharan mineral dust from ground level to almost 5 km altitude. The $\boldsymbol{R_{(532)}}$-profile also shows enhanced particle backscatter greater 2.0 in these altitudes. Profiles of calculated aerosol mass concentration highlight a pure dust regime ($c_{m(dust)} \approx 100\, \mu g\, m^{-3}$; aerosol extinction coefficients around 0.06 km^{-1}) at altitudes ranging from approximately 1.5 - 5.0 km altitude transitioning to a mixed marine and dust aerosol regime at lower atmospheric levels (0 - 1.5 km). The lidar measurements again do not indicate a pure marine aerosol regime at low altitudes. Both marine and settling mineral dust aerosol is found in the MBL (0 - 1.5 km).

As already indicated by the correlation of $\delta_{p(532)}$ and r_m shown in Figure 3.3 (c) the SALs described in cases (b) and (c) are also associated with enhanced concentrations of water vapor compared to the surrounding free troposphere: r_m and $\boldsymbol{R_{532}}$ in the lidar profiles show a distinct correlation (Figure 3.10). The SALs show almost uniformly increased water vapor

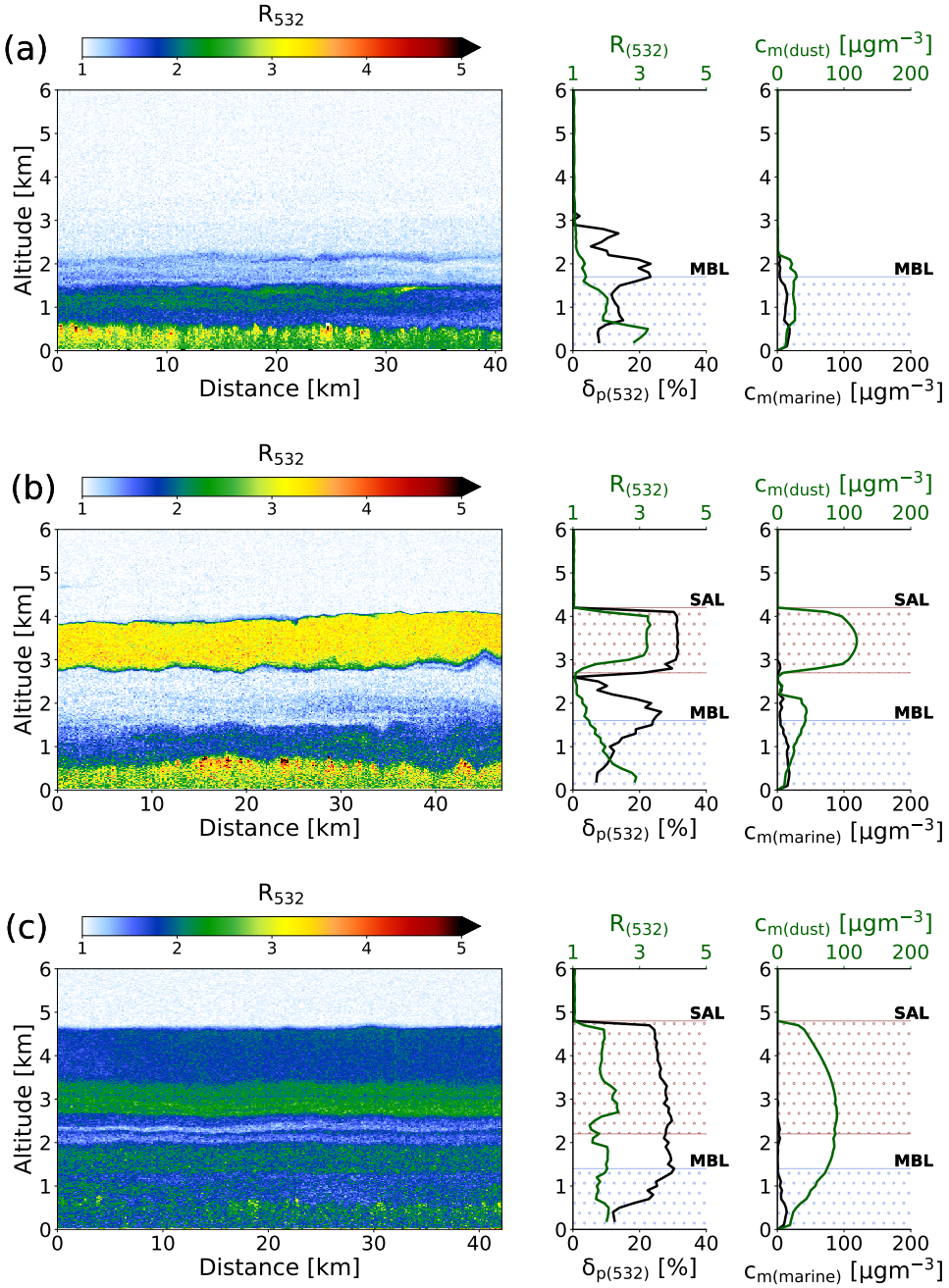

Figure 3.9: left: cross sections of WALES backscatter ratio $\boldsymbol{R_{532}}$; middle: averaged profiles of linear particle depolarization ratios $\delta_{p(532)}$ and backscatter ratio $\boldsymbol{R_{532}}$; right: derived aerosol mass concentrations ($c_{m(dust)}$ (red) and $c_{m(marine)}$ (blue)) for case (a) and (b) on 19 Aug as well as case (c) on 12 Aug 2016. Dotted areas indicate approximate extents of the marine boundary layer (MBL; blue) and the Saharan air layer (SAL; dark-red).

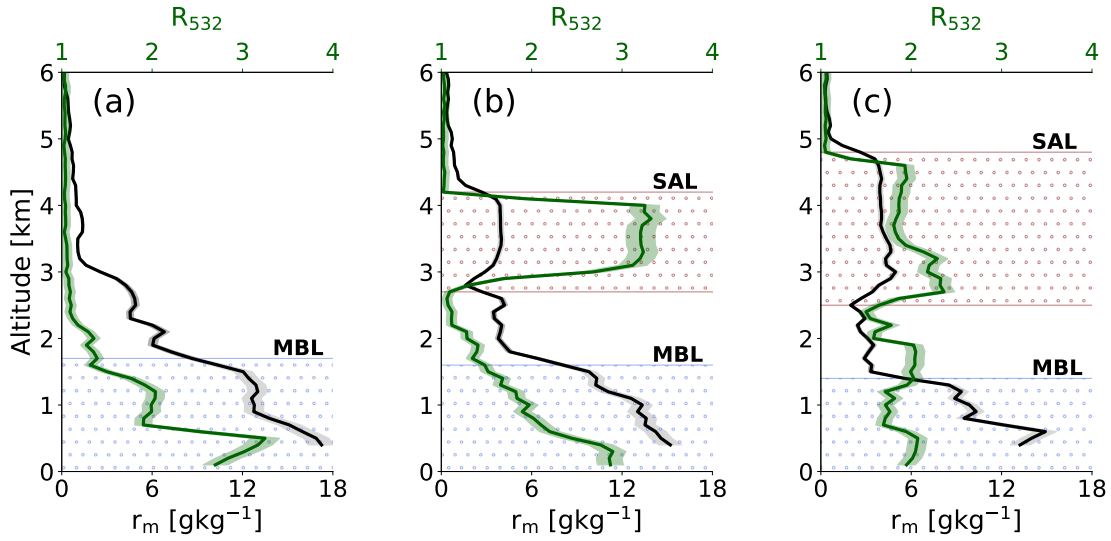

Figure 3.10: Averaged vertical profiles of backscatter ratio ($\boldsymbol{R_{532}}$) and water vapor mass mixing ratio (r_m) for cases (a),(b) and (c). Shaded: estimated measurement uncertainties. Dotted height intervals highlight the approximate extents of observed Saharan air layers (SALs, dark-red), and marine boundary layers (MBLs, light-green).

mixing ratios ranging from 3 - 5 gkg^{-1} compared to the surrounding free troposphere (case (b): 2.8 - 4.2 km; case (c): 2.5 - 4.8 km). Case (a) however, indicates that no distinct correlation of enhanced r_m and $\boldsymbol{R_{532}}$ could be observed in the SAL-free troposphere. The profile shows a drop of r_m to values smaller 1 gkg^{-1} at altitudes greater 3 km, indicating the transition from the MBL to the dry free troposphere. Such a drop in humidity was observed during most SAL-free periods in NARVAL-II, and has already been discussed in the framework of the dropsonde analysis in Section 3.1.3. It comes along with a strong TWI that is generated by the subsiding branches of the Hadley cell and the Walker circulation.

3.2.2 Saharan air layer radiative heating

Profiles of calculated short-wave, long-wave and net heating rates (24 h-averaged) for the three selected case studies are shown in Figure 3.11. Since WALES is able to measure both water vapor mixing ratios and aerosol optical properties, total heating rate profiles and contributions of mineral dust to total heating rate profiles can be derived. The dust-contribution to the total heating rate is derived as the difference between heating rates that consider dust in the model and heating rates with no dust in the model atmosphere.

Observed SALs in case (b) and (c) are well mixed (constant potential temperature Θ around 315 K). Both profiles have strong gradients of r_m and Θ at the upper edge of the SAL (at the boundary to the above dry and aerosol-free trade wind atmosphere) indicating the two

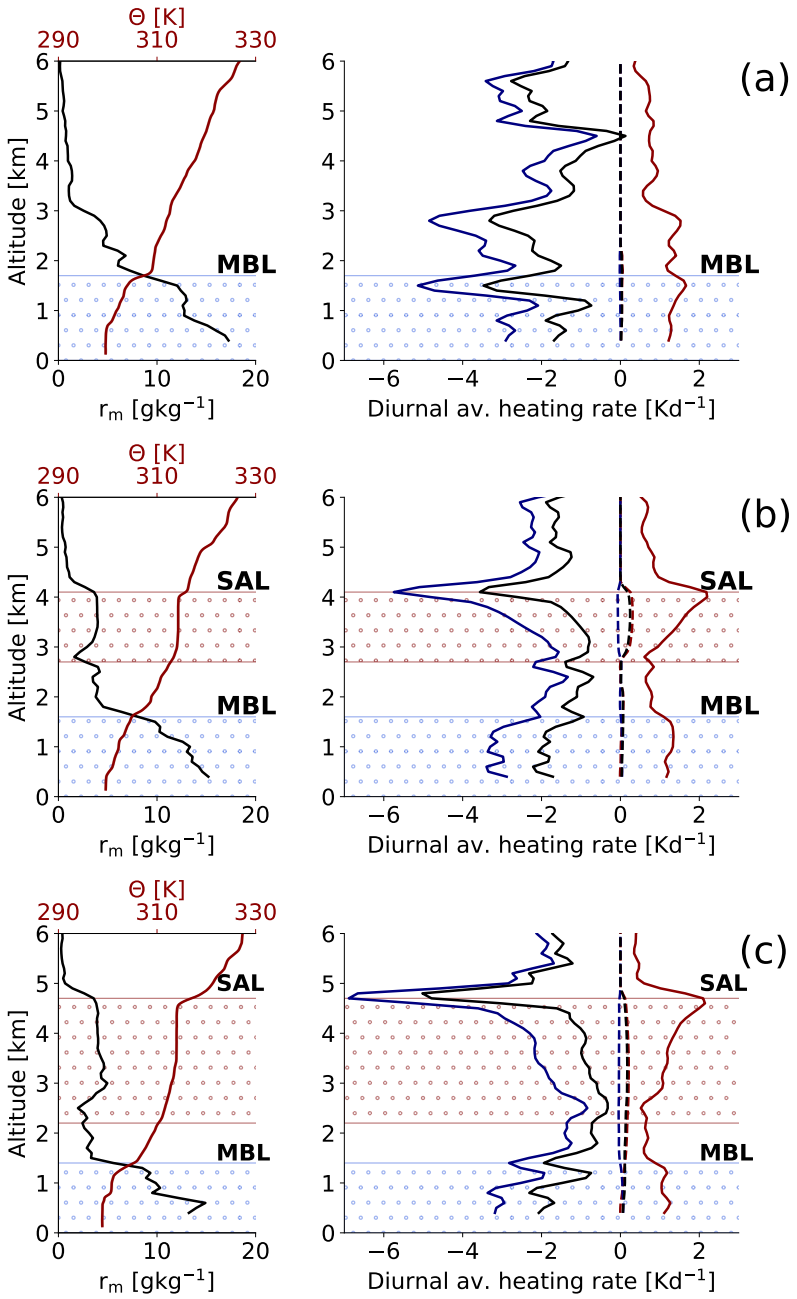

Figure 3.11: Left: the vertical profiles of derived water vapor mass mixing ratio from DIAL measurements (blue) and potential temperature from dropsonde measurements (red) for the three selected scenarios. Right: the diurnally averaged net (black), short-wave (red) and long-wave (blue) heating rates (solid). Dashed lines illustrate the aerosol-contributions to the total heating rate profiles). Colored and dotted height intervals highlight the approximate extent of the observed Saharan air layers (SAL, dark-red) and marine boundary layers (blue, dotted).

SAL-related bounding inversions (*Lilly*, 1968; *Dunion and Velden*, 2004; *Ismail et al.*, 2010). The MBL in all three cases is characterized by high relative humidities (r_m: 10-16 g kg^{-1}) and is capped by a temperature inversion (TWI) and a pronounced hydrolapse (r_m drops from >15 to approximately 5 g kg^{-1}).

Calculated profiles of diurnally averaged mineral dust short-wave heating rates for mean profiles of case (b) and (c) indicate an atmospheric heating of less than 0.5 K d^{-1} in SAL altitudes. Maximum short-wave heating is hereby found in altitudes of highest dust mass concentration (case (b): ∼3.5 km; case (c): ∼2.5 km). A dust aerosol heating rate profile of similar shape towards negative values is found in the long-wave spectrum. At altitudes of highest mass concentration dust aerosols show cooling rates of ∼0.2 K d^{-1}. This results in a small net warming effect of long-range-transported dust aerosols of approximately 0.3 K d^{-1} for both cases (b) and (c). The net mineral dust radiative heating rate for the SAL-free case (a) is limited to the lowest atmospheric levels and takes small values of less than 0.1 K d^{-1}.

The effect of water vapor on the total vertical radiative heating and cooling rate profile is much larger than the effect caused by the dust aerosols and also has a different shape. Greatest water vapor absorption of solar radiation takes place at the uppermost levels of the SAL and leads to strong heating at these levels. Long-wave cooling due to emission of radiation towards space is also strongest at the top of the SAL since there is no heating by atmospheric counter radiation from higher atmospheric levels. Hence, greatest total heating and cooling rates are found at the upper edge of both observed SALs (short-wave: 2.2 K d^{-1} (both cases); long-wave: -6 K d^{-1} (case (b)) and -7 K d^{-1} (case (c)). Adding short-wave and long-wave heating rates results in SAL net heating rates. They are entirely negative for both cases and take values from -1.0 to -3.5 K d^{-1} (case (b)) and -0.5 to -5.5 K d^{-1} (case (c)). Moreover, an intensification of net radiative cooling with height towards the top of the SAL is evident.

Another increase in short-wave heating and long-wave cooling rates is found within the MBL which is characterized by a moist mixture of mineral dust and marine aerosols in all three cases. However, the shape of the MBL heating rate profile in SAL-influenced regions differs to those in SAL-free regions. While for the SAL-free scenario strong cooling at the top of the MBL can be observed (strongly pronounced inversion; case (a)), SAL-influenced regions show less cooling (weakly pronounced inversion; cases (b) and (c)). Short-wave, long-wave as well as net heating rate profiles calculated for the dust-free case (a) show no distinct features above the MBL. In this case peak values of atmospheric heating and cooling correlate with regions of strongest gradients in r_m (maximum long-wave cooling: -5 K d^{-1}; maximum short-wave heating: 1.8 K d^{-1}). This emphasizes the dominating effect of water vapor on atmospheric heating.

3.2.3 Dust-radiative effects at surface level and top of the atmosphere

Saharan dust short-wave radiative effects at surface level and TOA (Figure 3.12) are investigated by analyzing modeled solar zenith angle dependent short-wave irradiances for the three discussed scenarios. It is assumed that the observed profiles do not change and remain sta-

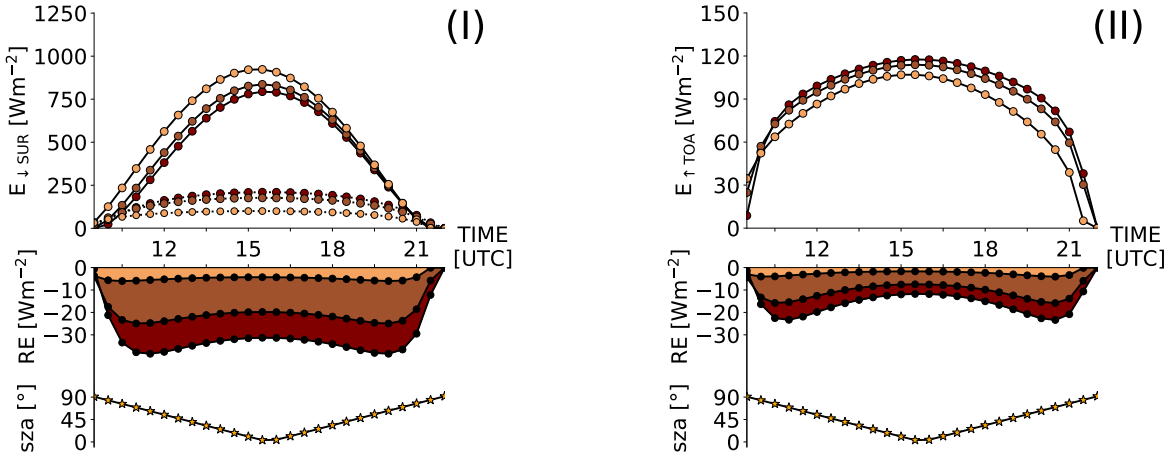

Figure 3.12: Top: Diurnal cycles of the modeled downwelling short-wave irradiances at surface level (I - $E_{\downarrow SUR}$: direct (solid), diffuse (dashed)) and upwelling short-wave irradiances at top of the atmosphere (II - $E_{\uparrow TOA}$). Bottom: The corresponding diurnal cycles of the modeled Saharan dust short-wave radiative effects (RE) at surface level (I) and top of the atmosphere (II) together with the solar zenith angle (sza). Colors indicate the three cases: light-orange (case (a)), orange (case (b)), dark-orange (case (c)).

tionary within a 24 h time frame. Saharan dust short-wave radiative effects at surface level (RE_{SUR}) and top of the atmosphere (RE_{TOA}) are inferred as the difference between modeled irradiances considering mineral dust particles in the model atmosphere ($E_{\downarrow tot(SUR)}$, $E_{\uparrow tot(TOA)}$) and irradiances calculated under assumption of no dust in the atmosphere ($E_{\downarrow nodust(SUR)}$, $E_{\uparrow nodust(TOA)}$),

$$RE_{SUR} = E_{\downarrow tot(SUR)} - E_{\downarrow nodust(SUR)}. \tag{3.1}$$

and,

$$RE_{TOA} = -(E_{\uparrow tot(TOA)} - E_{\uparrow nodust(TOA)}), \tag{3.2}$$

Downward and upward irradiances are primarily determined by the solar zenith angle, therefore having a symmetrical shape with maxima at noon (around 15:30 UTC). At intermediate zenith angles (morning and evening hours) Mie-scattering is the dominant contributor to $E_{\downarrow tot}$ and $E_{\uparrow tot}$ at both surface level and TOA. The longer the slant path of solar rays through SALs, the larger the fraction of backscattered light to space. As a reason, RE_{SUR} and RE_{TOA} show minimum magnitudes at low solar zenith angles around noon and maximum magnitudes at intermediate zenith angles in the morning and evening hours.

For case (c) a maximum negative RE_{SUR} of almost -40 W m^{-2} is calculated for morning and evening hours (11:30 and 20:00 UTC). At noon the diffuse fraction of downwelling irradiance ($E_{\downarrow diff}$) at surface level reaches 200 W m^{-2} making one third of $E_{\downarrow tot}$ at surface

levels. Calculations of RE_{TOA} show similar results for case (c). At intermediate zenith angles the diurnal maximum in atmospheric backscattering causes a maximum negative RE_{TOA} of -25 W m^{-2}. $E_{\uparrow tot}$ at TOA reaches maximum values of nearly 120 W m^{-2} at midday. For case (b) a lidar-derived RE_{SUR} of -25 W m^{-2} is computed for intermediate zenith angles. It shows a local minimum at noon (-20 W m^{-2}). Compared to case (c), $E_{\downarrow diff}$ at noon is slightly smaller (180 W m^{-2}). This reduced diffuse fraction is also evident when looking at RE_{TOA}. Due to the decrease in scattering, RE_{TOA} reduces to a minimum of -17 W m^{-2} for case (b). Compared to the other cases, case (a) shows the smallest values of RE_{SUR} ($>$-8 W m^{-2}) with weakly pronounced maxima during sunrise and sunset. RE_{TOA} is also weakest ($>$-5 W m^{-2}).

Chapter 4

Discussion

During NARVAL-II all observed SALs came along with enhanced concentrations of water vapor compared to the surrounding atmosphere. These findings fit well to former observations of water vapor mixing ratios in elevated SALs. *Kanitz et al.* (2014) for example derived water vapor mass mixing ratios of 4 to 5 g kg^{-1} (RH: 30 % to 80 %) inside a SAL form shipborne Raman lidar and microwave radiometer measurements in May 2013. *Jung et al.* (2013) deduced similar concentrations of r_m inside an elevated and long-range-transported SAL that traveled over the North Atlantic Ocean in early April 2010 ($\sim$ 4 g kg^{-1}). While *Kanitz et al.* (2014) did not examine the main drivers for SAL-moistening, *Jung et al.* (2013) tried to identify them by comparing vertical soundings of the observed SAL near its origin (Dakar-Senegal) and after its long-range transport (Barbados). The deduced profiles indicated that the observed SAL - which extended from the MBL-top to 4.00 km (Dakar) and 2.65 km altitude (Barbados) - was moistened during transport by upwelling surface fluxes, because water vapor concentrations inside the SAL were found to be by 2 g kg^{-1} higher at Barbados than at Dakar.

To retrace SAL-moisture during NARVAL-II, backward-trajectories are calculated for the two presented case studies where SALs were present (case (b): RF6, and case (c): RF3). Both SALs can be traced back to the coastal region of Senegal and Mauritania. Operationally launched radiosonde measurements at the airport of Dakar during the dust outbreaks together with dropsonde measurements during the research flights allow Lagrangian measurements of SAL-moisture. Figure 4.1 shows that for both case studies upwelling surface fluxes did not play a significant role for SAL-moistening. Additional moistening of the SALs during transport has not been observed. While SAL water vapor concentrations during RF6 (case (b)) were similar at the beginning and at the end of transatlantic transport ($\sim$ 4 g kg^{-1}), they were even higher over Dakar ($\sim$ 7 g kg^{-1}) than over the Caribbean ($\sim$ 4 g kg^{-1}) for the SAL which was observed during RF3 (case (c)). This drop of SAL-moisture during transport is most likely related to the dissipation and thinning of the SAL during transport. Differences in Θ and r_m indicate that the observed SALs descended during transport, since the tops of both observed SALs dropped by 0.7 km (RF3, case (c)) and 1.5 km (RF6, case (b)).

Identified SAL water vapor mass mixing ratios over Dakar fit well to observations by *Marsham et al.* (2008) who found that air masses over the Saharan desert can already show water

vapor mass mixing ratios in the range from 4 to 7 g kg^{-1}. Consequently, water vapor uptake during dust-mobilization processes might also be considered as a driver for SAL moistening. Especially Saharan dust mobilization by cold and humid downbursts (haboobs) from convective systems could contribute to SAL-moistening in the summer months (e.g. *Schepanski et al.*, 2009). However, a detailed identification of all processes that lead to SAL-moistening as well as of possible seasonal fluctuations of SAL-moistening by upwelling moisture fluxes, is not the focus of this thesis.

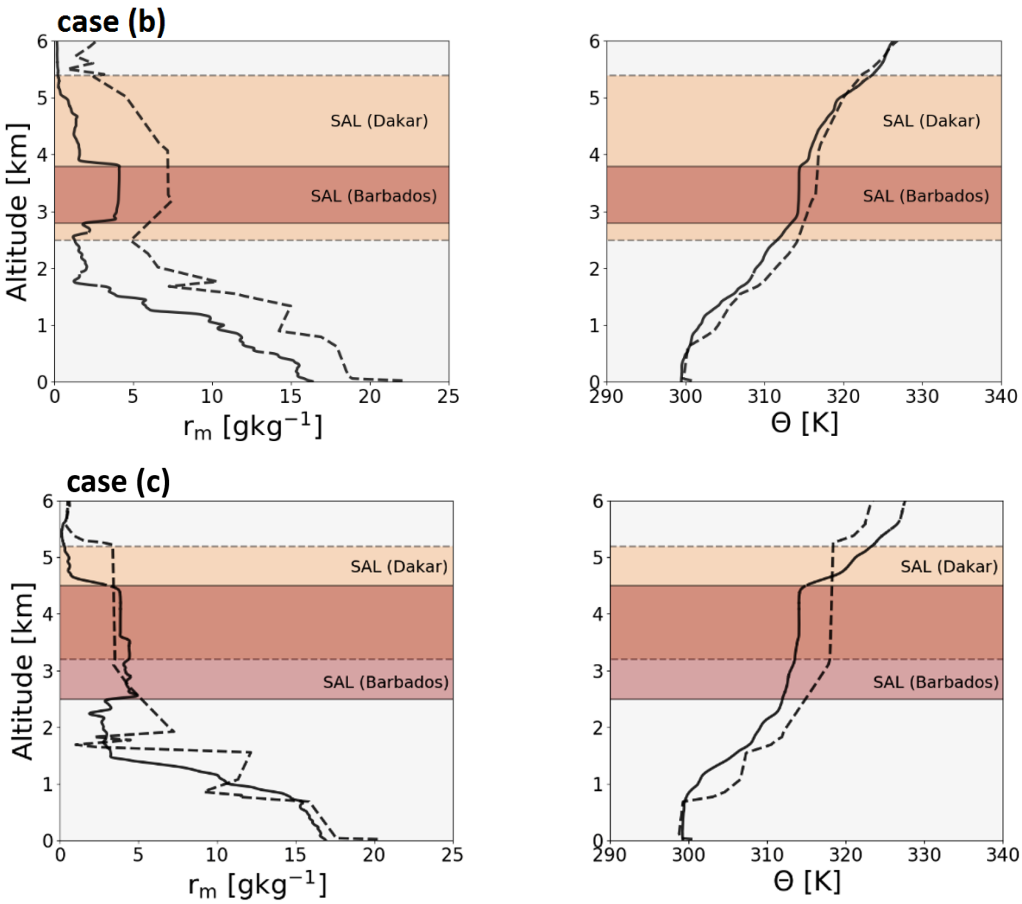

Figure 4.1: Lagrangian measurements (verified by calculated HYSPLIT backward trajectories) of vertical Θ and r_m-profiles of the observed SALs during the presented case studies (b (RF6 - top) and c (RF3 - bottom)) as measured by dropsondes near Barbados (solid) and by operational radiosondes at the beginning of SAL-transport near Dakar (dashed). Light brown areas mark the approximate vertical extent of the SALs over Dakar (dashed margins). Dark brown areas mark the vertical extent of the long-range-transported SALs as observed during the respective research flights (solid margins).

4.1 Implications of Saharan air layer radiative properties

Trapped by the two SAL-related inversions the received moisture remained enclosed within the SALs during transatlantic transport. The previous chapter illustrated the impacts of SAL water vapor on atmospheric radiative heating. Not only it is the strongest contributor to calculated heating rate magnitudes, but also it significantly changes the vertical structure of heating rate profiles. As a consequence, SAL-heating induced by water vapor has some important impacts on atmospheric stability and cloud development. Those implications are discussed in the following.

4.1.1 Impacts on Saharan air layer stratification

Inside the observed SALs it was shown that the net radiative heating rates are entirely negative and that cooling strengthens with height. *Lilly* (1968) showed that such a strengthening of cooling with altitude tends to decrease the static stability and to promote vertical mixing. Strengthening of heating with altitude has the opposite effect and increases static stability in the atmosphere. A schematic illustration of these radiative heating impacts on atmospheric stability is shown in Figure 4.2.

The observed strengthening of SAL-cooling with altitude during NARVAL-II is in line to results of prior studies, which found neutral stratification inside SALs (*Prospero and Carlson*, 1972). Dropsonde measurements of Θ and r_m during NARVAL-II also indicated that the observed SALs have been neutrally stratified and well-mixed (Θ = const.; see Figure 3.11 (b, c)). At the top and at the bottom of the SALs net radiative heating rates were observed to increase with altitude - an indicator of stable stratification, which is also marked by positive changes of Θ in dropsonde measurements. Those stable stratified regions mark the two bounding inversions that come along with SALs (*Carlson and Prospero*, 1972; *Dunion and Velden*, 2004; *Ismail et al.*, 2010).

Similar results have been found by *Kim et al.* (2004) who focused on the effect of enhanced water vapor concentrations within Asian dust plumes. They also highlighted that derived atmospheric heating rates within the dust plumes are altered by enhanced water vapor concentrations. In their study they compared heating rate calculations where measured water vapor profiles have been considered, to calculations where reference water vapor profiles have been used. Calculated maximum short-wave heating and long-wave cooling rates were also found to be shifted from the center to the top of the dust layers when including the measured water vapor profiles in calculations.

The findings of this thesis could answer the still open research question why super-micron mineral dust particles with diameters larger than 7 μm can still be found inside SALs after long-range transport and are not removed by gravitational settling. *Weinzierl et al.* (2017) explained that large and asymmetric dust particles with diameters of 20 μm, typical densities of 2.6 g cm^{-3} and shape factors of 1.4 are supposed to descend by 2.1 km d^{-1} according to Stokes gravitational settling theory. Hence, even if these large particles would start their transatlantic travel at the top of the SAL in 6 km to 7 km altitude, they would be removed from the

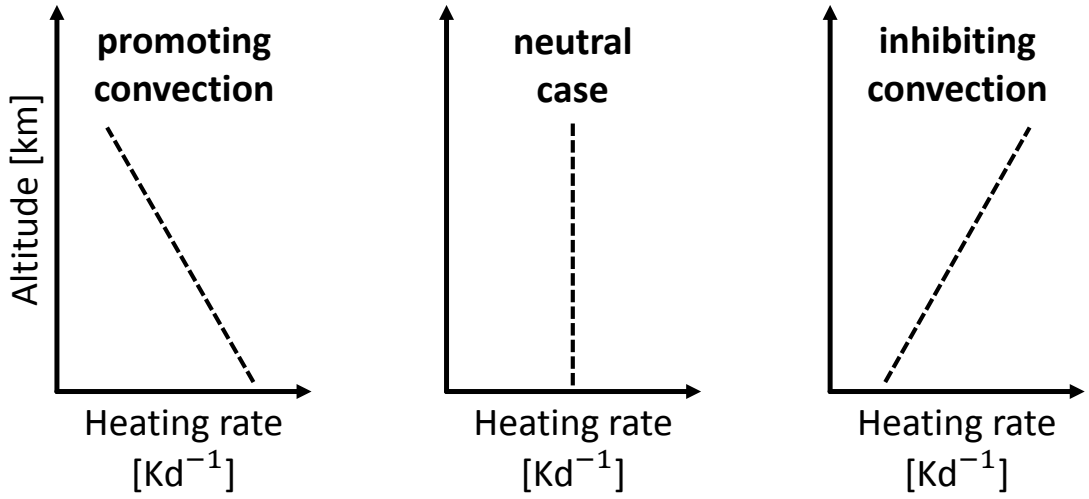

Figure 4.2: Illustration of radiative heating impacts on atmospheric stability.

atmosphere before they reach the Caribbean. However, analyses of mineral dust particle size distributions over Barbados by *Denjean et al.* (2015) and *Weinzierl et al.* (2017) highlighted that this is not the case. Expected maximum particle diameters of 7 μm were exceeded by far since particles with diameters larger than 20 μm could still be found in long-range-transported SALs.

Trying to unravel the processes behind these findings *Gasteiger et al.* (2017) used an integrated model and measurement approach to investigate particle settling processes during SAL advection. They conjectured that daytime convective mixing within the SAL could be the main driver for particle mixing and would allow dust particles with diameters larger than 20 μm to arrive in the Caribbean.

With the presented results in this thesis, vertical mixing processes within the SALs can be explained for the first time. They indicated that water vapor radiative heating could explain this phenomenon. It strengthens the cooling inside the SALs with altitude and therefore promotes vertical mixing processes inside the SALs. Additionally, water vapor radiative heating sustains the layers bounding inversions. Consequently, SAL radiative heating processes can counteract mineral dust settling from the SALs and help larger particles to remain inside the SALs during transatlantic transport.

To substantiate the hypothesis that vertical mixing processes counteract gravitational settling inside SALs, indicators for static stability from measurements by dropsondes of temperature and wind speed in SAL-regimes during RF3 are derived (Figure 4.3). RF3 is chosen, because a large number of dropsondes has been launched during that flight. An indicator that is frequently used to analyze the stratification and static stability of the atmosphere is the squared Brunt-Väisälä frequency $N^2 = \frac{g}{\Theta}\frac{d\Theta}{dz}$, which has already been introduced in Section 3.1.3. If N^2 takes values much higher than zero the atmosphere is stably stratified and buoyant motion is suppressed. Small positive values of N^2 indicate regions of neutral strat-

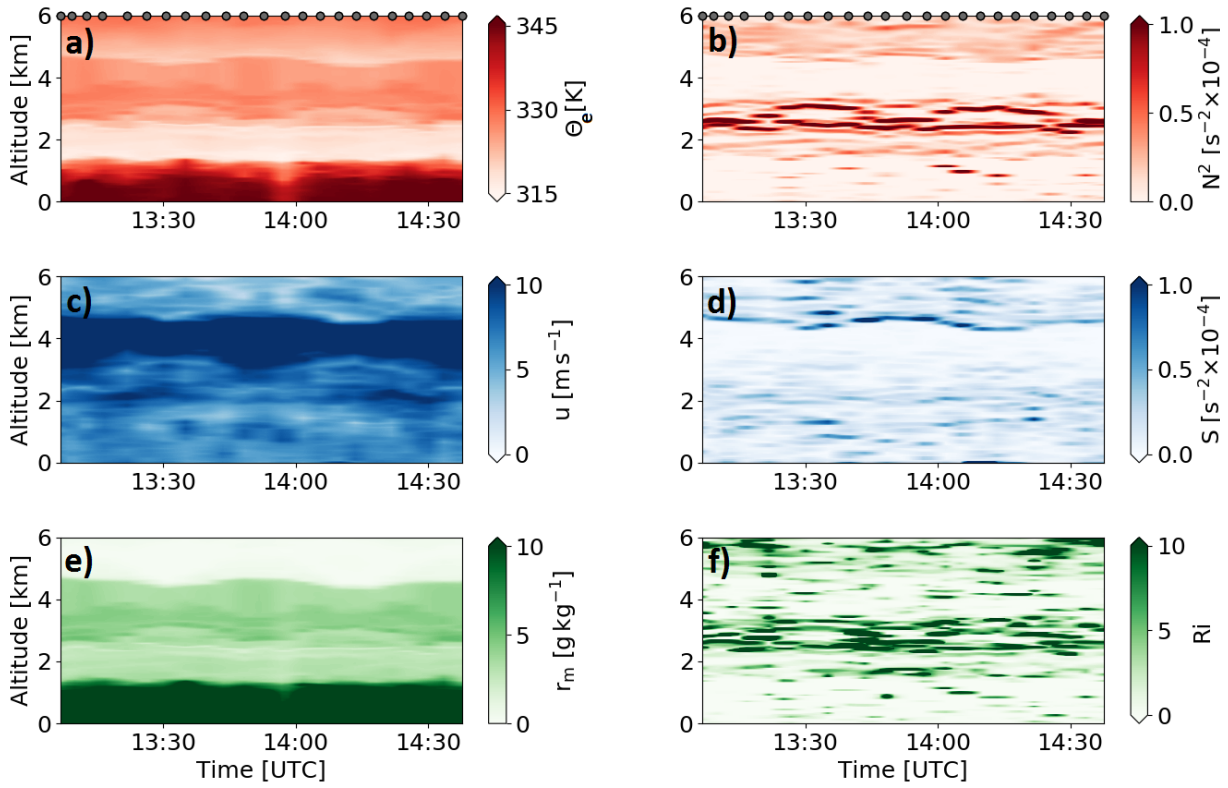

Figure 4.3: Vertical profiles of meteorological quantities as measured from dropsondes during RF3 that are interpolated along the HALO flight path: (a) equivalent potential temperature Θ_e, (b) Brunt-Väisälä frequency N^2, (c) wind speed u, (d) wind shear S, (e) water vapor mass mixing ratio r_m and (f) Richardson number Ri. Grey dots indicate the locations where the dropsondes have been launched.

ification where mixing processes can occur. In case of N^2 <0 , buoyant motions are likely. The 2D-profile of N^2 points out that the MBL (ranging from 0.0 km to approximately 1.5 km altitude) and the SAL (ranging from 1.5 km to approximately 5 km altitude) represent two neutrally stratified regimes, since N^2 takes very small values ($N^2 < 0.1 \cdot 10^{-4}\,\mathrm{s}^{-2}$). The profiles of equivalent potential temperature Θ_e and r_m also point towards a neutral stratification in these regions as both take constant values with altitude ($r_m \approx 4\,\mathrm{g\,kg}^{-1}$). The regions between the MBL and SAL and above the SAL are characterized by high static stability ($N^2 > 0.5 \cdot 10^{-4}\,\mathrm{s}^{-2}$). Those regions can be attributed to the three inversions in SAL-regimes: the TWI and the inversions at the top and the bottom of the SAL.

Nonetheless, turbulence and vertical mixing can even occur under stably stratified conditions as a consequence of gravity wave breaking events or strong flow shear,

$$S = \left(\frac{\partial u}{\partial z}\right)^2 = \left(\frac{\partial \mathbf{u}}{dz}\right)^2 + \left(\frac{\partial \mathbf{v}}{dz}\right)^2 \tag{4.1}$$

Here $\mathbf{u}$ and $\mathbf{v}$ represent the two components of the wind vector towards the East and the North. The dimensionless Richardson number is a parameter which is used for the analysis of atmospheric stability that takes both static stability and flow shear into account. It is the ratio of buoyant suppression of turbulent motion and the generation of turbulence due to flow shear and is defined as,

$$Ri = \frac{g}{\Theta} \frac{\frac{\partial \Theta}{\partial z}}{\left(\frac{\partial u}{\partial z}\right)^2} = \frac{N^2}{S}. \tag{4.2}$$

Hence, the greater Ri, the lower the chance for vertical mixing. Stability theory reveals that for the formation of turbulence Ri has to be smaller than a critical value of $1/4$ (e.g. *Turner*, 1973). This can either happen when shear overpowers stabilizing buoyancy forces or when great static instability is prevailing. During RF3 wind speeds have been considerably higher in SAL regions ($>$10 m s^{-1}) than in regions below and above ($<$10 m s^{-1}). These strong gradients of wind speed at the top and at the bottom of the SAL resulted in great flow shear. However, buoyant suppression of vertical motion overpowered the generation of turbulence due to flow shear in these regions ($Ri > 5$). In the interior of the SAL and the MBL almost no flow shear could be observed. Nevertheless, those regions can be identified as turbulent regimes ($Ri < 0.25$) as static stability was weak. Summed up, the analysis of N^2 and Ri confirms the hypothesis of vertical mixing due to radiative cooling inside SALs.

4.1.2 Impacts on the marine boundary layer and convection

Besides its impacts on atmospheric stability in SAL-altitudes, SAL-water vapor also has an impact on cooling and heating rate profiles inside the subjacent MBL. In Section 3.2 it can be seen that calculated net heating rates for the dust-laden cases (Figure 3.11 (b, c)) show less cooling at the top of the MBL compared to the SAL-free case (Figure 3.11 (a)). An elevated and moist SAL is associated with down-welling long-wave irradiance which counteracts radiative cooling inside the MBL and weakens the cooling of the MBL. This leads to a steadily increasing net heating rate profile within the MBL. However, for the SAL-free case no atmospheric counter-radiation is present. Hence, MBL-cooling strengthens with altitude and strongest cooling is located at the top of the MBL. As a consequence, the development of convection is reinforced (see Figure 4.4).

Stevens et al. (2017) used idealized distributions of water vapor in the lower atmosphere for a model study to highlight the impact of elevated moist layers on the vertical distribution of heating rates. They claimed that such layers could reduce the cooling at lower atmospheric levels and could therefore potentially modify the state of the boundary layer by inducing low-level circulations. A theoretical study by *Naumann et al.* (2017) already explained that

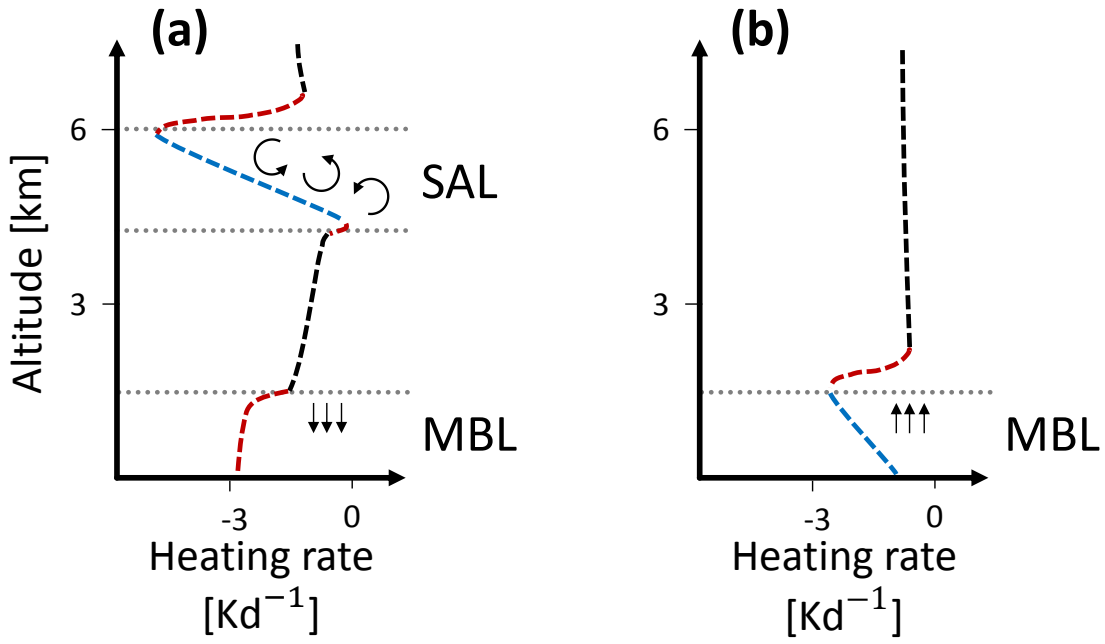

Figure 4.4: Schematic graph that illustrates the implications of radiative heating on atmospheric stability in SAL regions (a) and SAL-free regions (b). Red lines mark regions where atmospheric heating strengthens static stability. Blue lines indicate regions where atmospheric heating has a weakening effect on static stability and helps to promote vertical mixing processes. The TWI on top of the MBL and the two bounding inversions of the SAL are marked by dashed and dotted grey lines.

variations in infrared cooling due to vertical gradients of tropospheric moisture may drive atmospheric circulations in trade wind regions.

In addition to radiative heating or cooling, the MBL-state can also be modified by cooler sea surface temperatures due to dimmed solar radiation. For example, a study by *Foltz and McPhaden* (2008) has already highlighted that less down-welling solar radiation in dust-laden regions can cause gradients in sea surface temperature and can also potentially impact the evolution of clouds. In this thesis maximum radiative effects of -40 W m^{-2} have been derived at surface level. Similar values have been observed by *Kanitz et al.* (2013) who studied the Saharan dust radiative effect near source regions in the vicinity of the Cap Verde islands. Based on their shipborne aerosol Raman/polarization lidar measurements on 1 May 2010 they deduced a maximum diurnal dust short-wave radiative effect of approximately -60 W m^{-2} at surface level. Results in this work are of a slightly smaller magnitude which is most probably caused by the thinning of the SAL during long-range transport. Consequently, also the dust radiative effects at TOA are slightly smaller (*Kanitz et al.*, 2013: -42 W m^{-2}; this work: -25 W m^{-2}).

4.2 Cloud macro-physical properties in Saharan-dust-laden and dust-free regions

From the presented effects of SALs on atmospheric heating and static stability in the MBL, it seems likely that cloud macrophysical properties (i.e. cloud fractions, cloud top heights, cloud lengths and cloud gaps) are different for SAL regions and SAL-free regions.

The MODIS true color image shown earlier in Section 3.1.3 (Figure 3.4 - left) already indicates that the dust-free regions seem to be characterized by less clouds compared to the dust-laden ones during RF6. The low cloud amount in the dust-laden region (southern part of the flight track) is also evident in lidar measurements (see Figure 3.2). Whereas a lot of cloud signatures (high values of $\boldsymbol{R_{532}}$) are detected in the northern part of the flight track (after about 16:45 UTC), almost no cloud signature is detected along the earlier southern flight path - with the exception of the transition region to the dust-free research area. Another characteristic of clouds in SAL regions during RF6 is that their tops are rarely located higher than approximately 1 km. However, in dust-free regions during RF6 cloud tops reach almost twice as high ($\sim$ 2 km).

To examine if radiative effects of SALs have significant impacts on shallow marine clouds, differences in lidar-derived cloud macrophysical properties in regions from 10° N to 20° N are investigated for the whole NARVAL-II field campaign. For this purpose, cloud fractions (CFs) and distributions of cloud top heights (CTHs), cloud lengths (CLs) and cloud gap lengths (CGLs) are derived and compared for dust-free and dust-laden regions. It is also investigated whether correlations of SAL-properties (i.e. vertical extent or layer optical depths) and cloud macrophysical properties exist. To investigate possible seasonal dependencies, WALES lidar data collected during the dust-free NARVAL-I field campaign in winter 2013 (10 to 20 December, 44 h of measurements) is additionally analyzed (flight tracks indicated in Figure 2.8).

Cloud detection with lidar is usually performed by employing fixed signal thresholds (e.g. *Medeiros et al.*, 2010; *Nuijens et al.*, 2009, 2014) or by applying wavelet covariance methods for the detection of sharp gradients to the backscattered signal (*Gamage and Hagelberg*, 1993). To avoid potential miscategorizations of sharp aerosol gradients as cloud tops using wavelet transforms, a fixed threshold of $\boldsymbol{R_{532}}$ is used in this work. During NARVAL-II it was found that $\boldsymbol{R_{532}}$ in the cloud-free marine trade wind boundary layer as well as in the elevated SAL never exceeds a ratio of 10. Marine trade wind water-clouds are optically thick and thus take much larger values. Based on these findings a fixed threshold of $\boldsymbol{R_{532}} = 20$ is used for the cloud/no-cloud decision.

To determine the CTH, the profile of $\boldsymbol{R_{532}}$ is scanned from flight level downwards to 250 m altitude and the first range bin where $\boldsymbol{R_{532}}$ is greater or equal to the defined threshold is marked. Additionally, the whole profile is flagged as a cloud containing profile. All cloud containing profiles with CTHs in a certain altitude range are taken and divided by the total number of cloud-flagged profiles to obtain the CTH-fraction in the respective bin of the overall CTH-distribution. Similar to that the CF is defined as the number of all cloud containing profiles divided by the total number of vertical lidar profiles. For the calculation of CLs

along the flight path neighboring cloud-flagged vertical profiles are connected. The CL (of a cloud extending from point A to point B) is then determined as a function of the respective geolocations (aircraft latitude and longitude) and CTH using the haversine formula. CGLs are calculated analogously by connecting neighboring cloud-free profiles. Due to the instruments maximum horizontal resolution of approximately 200 m it is possible to resolve minimum CLs and CGLs of 200 m. It should be mentioned that not the maximum CL and CGL of each individual cloud or cloud gap, but the along-track length is derived. As a result, the amount of small clouds and cloud gaps in this analysis may be overestimated.

4.2.1 Cloud fraction, cloud top heights, cloud lengths and cloud gap lengths

A first indicator for differences in marine trade wind cloud occurrence is the cloud fraction CF. During NARVAL-II a total number of $3.2 \cdot 10^4$ one second resolved cloud tops were detected in trade wind regions ($N_{CT(dust)} = 8 \cdot 10^3$; $N_{CT(nodust)} = 2.4 \cdot 10^4$). They contribute to an overall observed CF of 24 % within the measurement period. In dust-free regions a CF of 31 % was derived, while in SAL-regions the observed CF was smaller by a factor of more than two (14 %). In the winter season (NARVAL-I) an almost three times higher CF of 37 % is derived.

Another parameter that can indicate differences between the three regions is the distribution of CTHs (Figure 4.5). In the SAL-regions only a small fraction of clouds exceeds an altitude of 2 km and no cloud top is found at altitudes higher 2.5 km. The majority of CTHs (∼61 %) is found within the altitude range from 0.5 km to 1.0 km in lower altitudes of the MBL-cloud layer. 26 % of all detected CTHs are located in the 1.0 km to 1.5 km height interval and only 11 % of that fraction contribute to the interval from 1.5 km to 2.0 km altitude. Cloud tops in altitudes higher than 2.5 km (including deeper reaching convection with maximum top heights of 6 km) are found in ∼16 % of all dust-free cloud profiles. Below around 3 km altitude the CTH-distribution shows a two-modal structure with two local maxima ranging from 0.5 km to 1.0 km (∼35 %) and 1.5 km to 2.0 km altitude (∼20 %). Several clouds were also detected in the lowermost 0.5 km of the atmosphere (∼1 %).

In the dust-free winter season a shift of the distribution to higher altitudes is observed, since most cloud tops were sampled in the interval from 2.0 km to 2.5 km altitude (∼39 %). However, no cloud was observed in altitudes higher 3.5 km. This shift is most probably caused by a slightly higher TWI in winter months as presented by *Stevens et al.* (2017). They compared mean dropsonde-profiles of water vapor mixing ratio during NARVAL-I and II.

Nuijens et al. (2009) and *Nuijens and Stevens* (2012) claimed that high wind speeds near surface correspond to an increase of boundary layer humidity leading to a deepening of the cloud layer and increased area rainfall. This is also presented by *Lonitz et al.* (2015), who used Large Eddy Simulations to show how increased humidity associated with observed dusty boundary layers can change the evolution of the cloud layer. However, when comparing boundary layer wind speed and humidity from dropsonde measurements in the two regimes, no distinct differences can be observed. This supports the hypothesis that the stabilizing effect due to radiative heating of the MBL in SAL-regions is the responsible mechanism for

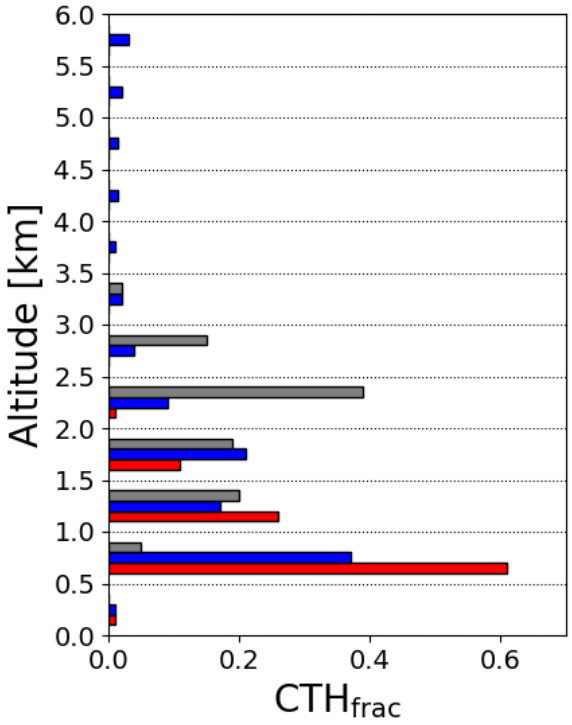

Figure 4.5: Histograms of detected CTH-fractions during NARVAL-I and II with bins of 0.5 km size. Red bars illustrate the distribution of CTH-fractions in SAL-regions. Blue bars represent the derived CTH distribution from measurements in the dust-free trades during NARVAL-II. Grey bars show the derived CTH in the dust-free winter season during NARVAL-I.

the observed differences in cloud fraction and cloud top height. Divergence measurements during NARVAL-II discussed by *Bony and Stevens* (2019) and *Stevens et al.* (2019) also show that dynamical properties between dust-laden and dust-free regions are different. They found that in contrast to dusty regions the MBL vertical motion in the dust-free region is directed upwards and would therefore promote the evolution of clouds.

It was shown that the SAL radiative heating can suppress vertical mixing processes and the evolution of convection in the MBL. Hence, suppressed cloud development must also be reflected in CL and CGL-distributions of marine trade wind clouds in SAL-regions and mineral dust-free regions (Figure 4.6). A total of 3688 and 2355 clouds were observed in dust-free and dust-laden regions during NARVAL-II and 5010 clouds were detected during NARVAL-I in dust-free winter. In all three samples clouds with horizontal extents of less than 0.5 km are by far the most numerous ones. Whereas 72 % of all clouds in SAL-regions are of this length, 65 % of all clouds detected in the clear summer trades and 61 % of all clouds detected in the clear winter trades contribute to this length-interval. Both regions show a decreasing trend

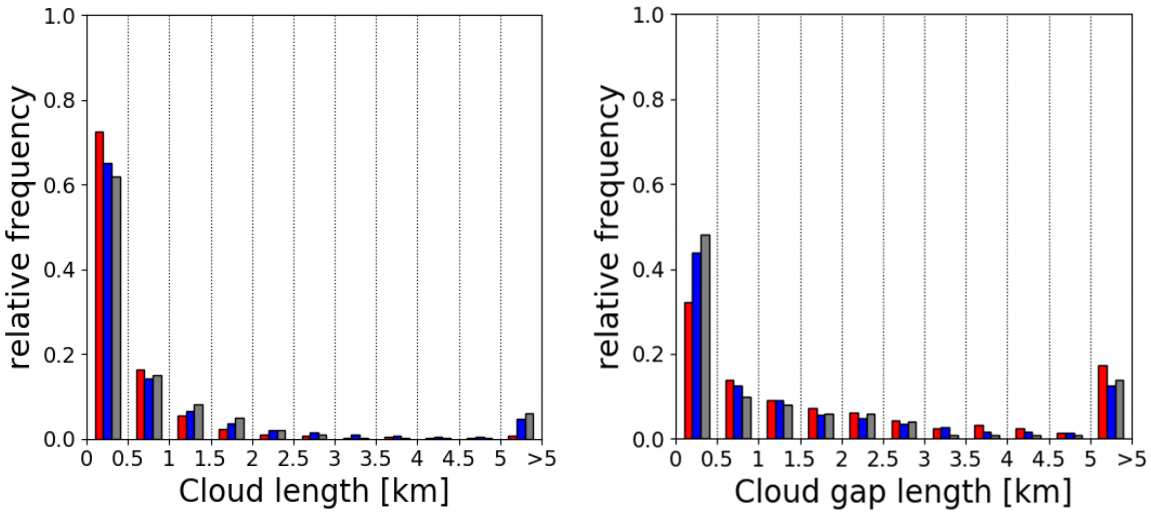

Figure 4.6: Histograms of detected CLs (top) and CGLs (bottom). Red bars illustrate the distribution of CLs and CGLs of marine low clouds located below Saharan dust layers. Blue bars represent the distribution derived from measurements in the dust-free trades during NARVAL-II. Grey bars show the derived distribution in the dust-free winter season during NARVAL-I.

in frequency of CL-occurrence for lengths of up to 5 km. Relative frequency drops to 17 % (dust-laden), 16 % (dust-free) and 16 % (NARVAL-I) in the length interval 0.5 km to 1.0 km. Only 5 % of all clouds in dusty regions are observed to have a horizontal extent greater than 2.0 km. This fraction almost doubles to 9 % in dust-free regions and in winter months. The main contributor to this fraction are clouds with horizontal extents of more than 5 km (4 and 5 %). Clouds of this length are basically only found outside dust-laden regions.

Similar to the distribution of CLs, also CGL-frequencies decrease with increasing CGL (Figure 4.6, right). In all three regimes cloud gaps shorter 0.5 km are dominating. They contribute with 45 % and 35 % to the total amount of observed cloud gaps in dust-free and dust-laden regions during NARVAL-II and with even 48 % in winter months. A different picture emerges, when looking at the amount of CGLs greater than 5 km. A fraction of 17 % is found to be greater than 5 km below dust layers, whereas in dust-free regions and in winter months these gap sizes contribute with 12 % and 14 % to the distribution. CGL-fractions in range bins from 1.5 km to 4.5 km decrease in both regions consistently with increasing CGL.

The statistical significance of observed differences in all shown distributions (i.e. of CTHs, CLs and CGLs) was checked by randomly resampling the respective data sets to smaller sub-sets and by comparing the shapes of the resulting distributions to the shape of the overall

distributions. The shapes of the resampled distributions showed no major differences compared to the overall distributions. Thus it can be concluded that NARVAL-measurements indicate the presence of less, shallower and smaller clouds in Saharan dust-laden trade wind regions compared to dust-free regions.

This work for the first time investigated shallow marine cloud macrophysical properties using highly resolved airborne measurements in both dust-laden and dust-free subtropical regions. The structure of subtropical marine cloudiness has already been a focus of prior remote sensing studies (e.g. *Nuijens et al.*, 2009; *Medeiros et al.*, 2010; *Siebert et al.*, 2013; *Nuijens et al.*, 2014). Satellite measurements are the major source for retrieving cloud-macrophysical properties, as they provide long-term measurements with nearly global coverage. However, the major drawback of satellite measurements is their coarse spatial resolution. Since most shallow marine clouds do only extend over a few hundred meters, their sensitivity is simply too low to detect them with high resolution. As a consequence, prior studies that concentrated on shallow marine cloud statistics rather focused on long-term and large-scale observations of marine clouds, e.g. low-level boundary layer cloud cover in the subtropical winter months (*Medeiros et al.*, 2010). Furthermore, these studies did not distinguish between dusty and dust-free trade wind regimes.

4.2.2 Connecting the properties of Saharan air layers and subjacent clouds

In a model study by *Wong and Dessler* (2005) it was claimed that the convection barrier increases with SAL aerosol optical depth. To investigate a possible relation between SAL optical depth or layer vertical extent and marine trade wind CTH and CF, their distributions are analyzed as a function of SAL vertical extent and optical depth of overlying mineral dust layers (Δz_{SAL} and $\tau_{SAL(532)}$; Figure 4.7). CFs and CTHs in dust-flagged profiles of all four research flights are grouped together with respect to similar Δz_{SAL} (bin width: 0.2 km) and $\tau_{SAL(532)}$ (bin width: 0.015). During NARVAL-II SALs with maximum vertical extents of 4 km and maximum optical depths of 0.4 were observed (Figure 3.2). However, below optically thick dust layers ($\tau_{SAL(532)} > 0.24$; $z_{SAL} > 3.8$ km) not any cloud has been detected.

The distribution of CTH as a function of Δz_{SAL} shows that up to a layer thickness of 1.8 km mean CTH decreases with increasing Δz_{SAL} from 1.4 km to 0.8 km altitude. For a greater layer thickness ($\Delta z_{SAL} > 1.8$ km) this trend is not evident anymore. A further increase in Δz_{SAL} does not imply a significant decrease in mean CTH - in some bin-intervals the mean CTH even increases slightly. Mean CTHs vary strongly below vertically thin dust layers ($\sigma=$ 0.5 km) - an indication for the presence of both shallow developing convective clouds and higher reaching trade wind clouds within the MBL. With increasing Δz_{SAL} the variability of mean CTH decreases and reduces to $\sigma < 0.2$ km for $\Delta z_{SAL} < 3$ km. This suggests that the cloud layer indeed lowers and that the few evolving clouds are confined to low levels of the MBL. The CF-distribution as a function of Δz_{SAL} does not show any distinct trend for geometrically thin layers. For $\Delta z_{SAL} < 1$ km CF takes values around 20 % - only slightly lower values than the CF derived from measurements in dust-free regions. For vertical extents

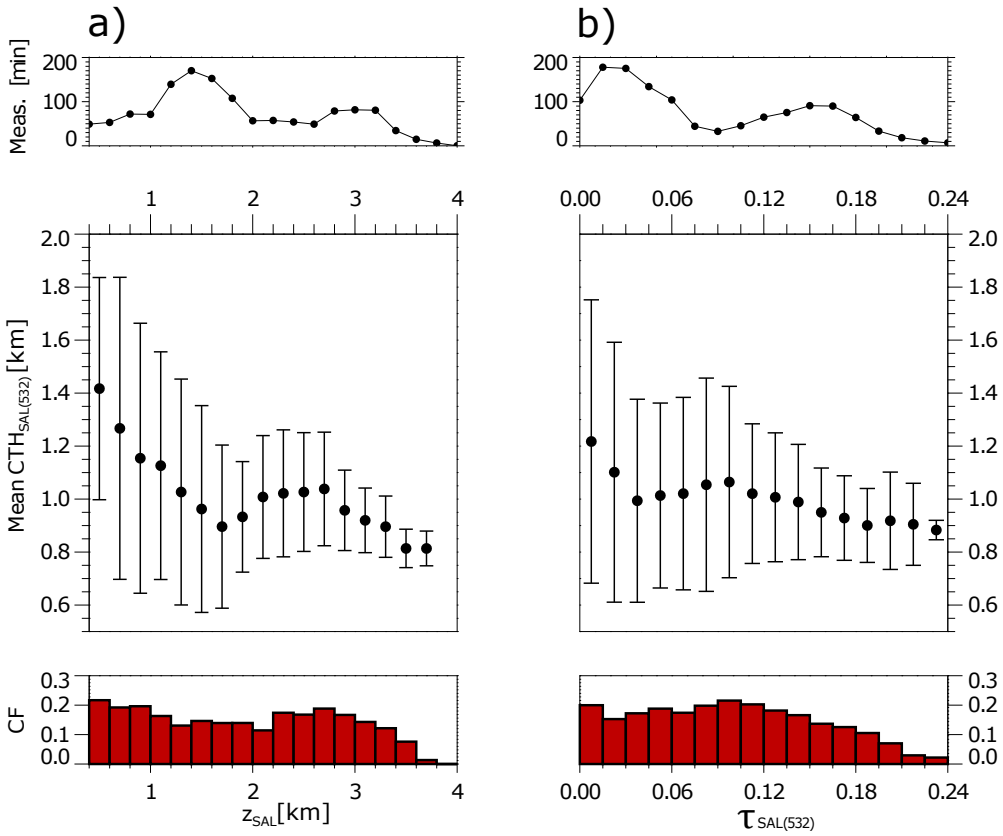

Figure 4.7: (a) Mean CTHs (middle) and CF (bottom) of clouds detected below Saharan dust layers as a function of Saharan dust layer vertical extent (Δz_{SAL}) - bin-interval: 0.2 km, (b) Mean CTHs (middle) and CF (bottom) of clouds detected below Saharan dust layers as a function of Saharan dust layer optical depth ($\tau_{SAL(532)}$) at 532 nm wavelength - bin-interval: 0.015. Bars mark respective standard deviations of mean CTHs (1σ). The uppermost graphs in (a) and (b) illustrate summed measurement-times in each interval.

ranging from 1 km $< \Delta z_{SAL} <$ 2.6 km no clear decrease in CF is detected. In this range CF varies around 15 % and even increases slightly. A clear decreasing trend of CF with increasing Δz_{SAL} is obvious only for $\Delta z_{SAL} >$ 2.6 km.

Next, the CTH distribution as a function of dust layer optical depth $\tau_{SAL(532)}$ is analyzed. Up to a value of $\tau_{SAL(532)} \sim 0.05$ the mean CTH decreases with increasing optical depth of the aerosol layer. The mean CTH drops from ∼1.3 km to ∼1.0 km in this region. A further increase of $\tau_{SAL(532)}$ to a value of about 0.12 does not show any further decrease in mean CTH. This is in line with the observed decrease in CF as a function of $\tau_{SAL(532)}$ in this range. The observed CF increases slightly from 15 % to 20 % for small SAL-optical depths ($\tau_{SAL(532)} <$ 0.12). At the upper tail of the distribution ($0.12 < \tau_{SAL(532)}$) the mean CTH as well as the CF decrease again. CFs shows a steady decrease of about 20 % in the range from $\tau_{SAL(532)} = 0.12$ to 0.24. Moreover, the variability of mean CTH in that range gets smaller, again indicating that higher-reaching convection is suppressed.

For the interpretation of these distributions the accumulated measurement-time in the respective intervals as well as the contribution of different research flights have to be taken into account. Mainly data collected in the course of RF3 contributes to SAL-measurements in the ranges 0.09$<\tau_{SAL(532)}<$0.24 and 2 km$<\Delta z_{SAL}<$4 km (Figure 3.2), thus being the main contributor to observed increases of mean CTH and CF in regions of high $\tau_{SAL(532)}$ and Δz_{SAL}. The remaining research flights (RF2, RF4 and RF6), were characterized by thinner dust layers that were rather decoupled from the MBL and contribute to regions of small $\tau_{SAL(532)}$ and Δz_{SAL}.

Altogether, a decreasing trend of CTH and CF as a function of dust layer optical depth and vertical extent was detected during research flights over elevated and long-range-transported SALs. However, RF3 showed a predominant and strongly pronounced transition layer that possibly altered the cloud layer resulting in an increased CF and CTH in the respective intervals of $\tau_{SAL(532)}$ and Δz_{SAL}.

Chapter 5

Summary and Outlook

5.1 Summary of results

Lidar data sets collected during the NARVAL-II field campaign contributed to a better understanding of long-range-transported SALs, their radiative effects and their implications for atmospheric stability as well as cloud development. By combining airborne HSRL and water vapor DIAL measurements it was possible to identify typical characteristics of long-range-transported SALs. This has also been addressed in research question (R1) in Section 1.4:

(R1) What are typical optical and meteorological characteristics of long-range-transported SALs?

In the framework of the NARVAL-II field campaign upstream the Caribbean islands it was possible to take measurements of meteorological and microphysical parameters of several long-range-transported SALs within a set of 4 research flights. All layers traveled for 5 to 10 days over the Atlantic Ocean and showed maximum dust particle mass concentrations of up to $120\,\mu g\,m^{-3}$. Their maximum vertical extents as well as layer optical thicknesses varied from 1 km to 4 km and 0.1 to 0.4. All observed SALs showed characteristic values of $\delta_{p(532)}$ for transported Saharan mineral dust ($\approx$0.3).

Differences in vertical profiles of meteorological properties between subtropical regions comprising elevated SALs and regions free of elevated SALs were studied by means of a dropsonde analysis during RF6. In SAL regions a three-layer-structure consisting of the MBL, a transition layer and the SAL was observed. Consequently, SAL-regimes were characterized by three inversions in the lower troposphere: the two bounding inversions of the SAL and the TWI. In contrast, only the TWI was present in regions without SALs. The interior of all observed SALs showed nearly constant potential temperature - an indicator for neutral

stratification and vertical mixing.

The main finding of this analysis were enhanced water vapor concentrations ($\approx 4\,\mathrm{g\,kg^{-1}}$) inside the observed SALs compared to the surrounding atmosphere. It was shown that these enhanced concentrations can be retraced to the origin of transport. This finding suggests that already during dust mobilization at the beginning of transport SALs get moistened. Water vapor represents the Earth's strongest greenhouse gas. Therefore, it also has a great impact on the radiation budget. The second research question addressed the need for a better understanding of the radiative effects of long-range-transported SALs and also aimed at a better understanding of the role of water vapor for atmospheric radiative heating (R2):

(R2) What are the radiative effects of long-range-transported SALs?

To answer this second question, radiative transfer simulations with WALES lidar input data were performed. Calculated radiative effects of long-range-transported SALs at surface level and top of the atmosphere revealed that maximum short-wave radiative effects of -40 $\mathrm{W\,m^{-2}}$ (surface) and 25 $\mathrm{W\,m^{-2}}$ (TOA) are found at intermediate zenith angles. These numbers fit well to findings from other studies.

NARVAL-II lidar data were also used to quantify atmospheric heating rates. It was found that water vapor plays the dominant role for atmospheric heating rates in SAL-altitudes. Compared to water vapor, dust aerosol was identified to have a minor effect on total heating rates in SAL-altitudes. Only small positive maximum dust aerosol heating rates of 0.3 to 0.5 $\mathrm{K\,d^{-1}}$ in the short-wave and slightly negative maximum cooling rates of -0.1 to -0.2 $\mathrm{K\,d^{-1}}$ in the long-wave spectrum were found at altitudes of highest aerosol mass concentration. Water vapor, however, was found to contribute much stronger to total SAL-heating with maximum short-wave and long-wave heating rates of 1.8 to 2.2 $\mathrm{K\,d^{-1}}$ and -6 $\mathrm{K\,d^{-1}}$ to -7 $\mathrm{K\,d^{-1}}$ at the uppermost levels of the SAL. As a result, calculated net heating rates inside SALs are entirely negative and decrease with altitude. The impact of SAL-water vapor on radiative heating highlights the necessity of a correct vertical parametrization of water vapor in radiative transfer simulations.

Radiative heating of atmospheric layers can have an effect on atmospheric stability not only in the heated layer itself, but also on surrounding atmospheric layers like the MBL. A further reaching research question concerning the radiative effects on atmospheric stability has been posed in (R3) and was discussed in the framework of this thesis:

(R3) How can SAL-radiative properties impact atmospheric stability?

Radiative transfer calculations have shown that water vapor radiative cooling in SAL-altitudes strengthens with height. As a consequence, vertical mixing - which counteracts particle settling processes - is promoted inside the SAL. Dropsonde measurements have also confirmed the well-mixed and neutrally stratified layering inside the observed SALs during NARVAL-II (Θ = constant). Overall, radiative effects of water vapor can explain why super-micron particles with diameters greater than 7 μm remain inside the SAL during transatlantic transport and do not settle towards the surface as predicted from Stokes gravitational settling theory.

SALs were also found to have a possible impact on cloud development in the MBL since they introduce additional atmospheric counter-radiation towards the top of the MBL. As a result, MBL tops in dust-laden regions do not experience as much cooling as in SAL-free regions. This is also indicated by the heating rate profile in SAL-regions which is increasing with altitude and therefore counteracts the development of convection in the MBL.

Whether these effects are leading to differences in cloud macrophysical properties of shallow marine clouds (i.e. CFs, CTHs, CLs and CGLs) or not was addressed in the final research question of this thesis (R4):

(R4) Do SALs have an effect on shallow marine cloud occurrence and cloud macrophysical properties (i.e. cloud top heights, cloud lengths and cloud gap lengths)?

To answer these research questions a comparison of marine low cloud macrophysical properties in dust-laden and dust-free trade wind regimes was conducted. Significant differences in the CTH-distribution as well as in the CL-distribution and CGL-distribution were found for flights in SAL-regions compared to the distributions derived from flights in dust-free regions. It can be summarized that during times with SALs less, shallower (CTHs < 2.5 km) and smaller clouds were present than during times without SALs. The overall derived CF in the dust-laden trade wind summer regime was 14 % and thus a factor of two smaller than the CF of 31 % and 37 % derived from observations in the dust-free regime and the winter season.

To investigate a possible relation between SAL optical depth or layer vertical extent and marine trade wind CTH, the CTH- and CF-distribution was analyzed as a function of SAL vertical extent and optical depth. It was found that mean CTH decreased with increasing layer vertical extent for vertically thin layers (< 1.5 km). Additionally, the mean CTH-variability for these layers was high, indicating the occurrence of higher-reaching clouds in those regions. There was no significant decrease of mean CTH for thicker dust layers, but a reduction of CTH-variability could be derived. Also a decrease in mean CTH-variability with increasing dust layer optical thickness starting at $\tau_{SAL(532)} \approx 1.2$ could be detected. Moreover, a decrease in CF came along with this reduction in variability of the mean CTH. Below optically thick dust

layers with $\tau_{SAL(532)} > 0.24$ no cloud was detected. These results indicate that optically and vertically thick elevated Saharan dust layers have a greater suppressing effect on convection below than optically and vertically thin layers.

5.2 Outlook and open questions

During NARVAL-II, the majority of mineral dust particles was located inside an elevated SAL above the MBL. However, during previous field campaigns it was observed that the vertical distribution of long-range-transported mineral dust can be highly variable (e.g. *Reid*, 2002). For example, during the Puerto RIco Dust Experiment (PRIDE) in summer 2000 the majority of dust was in some cases observed to be located at lower atmospheric levels and in other cases it was observed to be located in an elevated layer. A distinct seasonal pattern of Saharan dust transport towards the Atlantic Ocean was already found by *Chiapello et al.* (1995), who studied the vertical distribution of mineral dust particles at the beginning of long-range transport at the Cape Verde islands. They found that in contrast to the summer months, wintertime dust-transport towards the Atlantic Ocean is mainly taking place at lower atmospheric levels.

When the majority of Saharan dust particles is transported at low atmospheric levels and when dust particles are not well separated from the MBL (as it was the case during NARVAL-II), many further research questions arise: How do mineral dust particles modify boundary layer cloudiness when they are transported at lower atmospheric levels and not in elevated layers? Can changes in cloud macrophysical properties be observed? Do these particles act as CCNs (like proposed by e.g. *Karydis et al.*, 2011; *Bègue et al.*, 2015) and modify cloud microphysics at low atmospheric levels? Could this have an effect on precipitation? As mineral dust particles are known to be good INPs (e.g. *Seifert et al.*, 2010; *Hoose and Möhler*, 2012; *DeMott et al.*, 2015; *Villanueva et al.*, 2020) - do higher reaching clouds in a dusty atmosphere have a more pronounced ice phase than in a dust-free atmosphere? Moreover, questions regarding the reasons for variable vertical distributions of mineral dust and whether there is a certain seasonal pattern in their vertical distribution not only at the beginning but also throughout the long-range dust transport should be answered in the framework of future studies.

Another unanswered research question is how the SAL gets moistened. Analyzing backward trajectories in more detail and focusing on measurements of moisture fluxes at dust source regions could contribute to a better understanding of this research objective. It should also be investigated to what extent upwelling fluxes from sea surface and from land surfaces contribute to SAL-moistening. Possible entrainment processes of moisture between the SAL and SABL and adjacent layers should also be identified.

Data during future field campaigns should also contribute to a better understanding of a possible seasonal variability in the transport of SAL-moisture. Radiative transfer calculations should be performed for data sets during the subtropical winter season and should also be compared to the results of this work which concentrated on the summer season. Moreover, the effects of radiative SAL-heating on marine cloud development in winter months should be investigated in detail.

Abbreviations and Symbols

List of Abbreviations

Abbreviation	Explanation
AEJ	African Easterly Jet
AEW	African Easterly Wave
AERONET	AErosol RObotic NETwork
ALADIN	Atmospheric LAser Doppler INstrument
APD	Avalanche PhotoDiodes
ATLID	ATmospheric LIDar
BOMEX	Barbados Oceanographic and MEteorological EXperiment
BRDF	Bidirectional Reflectance Distribution Function
BS	Beam Splitter
CALIOP	Cloud-Aerosol LIdar with Orthogonal Polarization
CALIPSO	Cloud-Aerosol LIdar and Pathfinder Satellite Observations
CPR	Cloud Profiling Radar
CCN	Cloud Condensation Nuclei
CF	Cloud Fraction
CL	Cloud Length
CGL	Cloud Gap Length
CH_4	Methane
CO_2	Carbon Dioxide
CTH	Cloud Top Height
DAC	Data Acquisition Computer
DBS	Dielectric Beam Splitter
DFB laser	Distributed FeedBack laser
DIAL	DIfferential Absorption Lidar
DISORT solver	DIscrete ORdinate Radiative Transfer solver
DLR	Deutsches Zentrum für Luft- und Raumfahrt
EarthCARE	Earth Clouds, Aerosols and Radiation Explorer
EDMO	ICAO-Code for the Airport Oberpfaffenhofen
ERFaci	Effective Radiative Forcing due to aerosol-cloud interactions
EUCAARI-LONGREX	EUropean integrated project on aerosol Cloud climate And AiR quality Interactions - LONG-Range EXperiment
EUREC^{4}A	ElUcidating the RolE of Clouds-Circulation Coupling in ClimAte
FWHM	Full Width at Half Maximum
GARP	Global Atmospheric Research Program
GATE	GARP Atlantic Tropical Experiment

Abbreviation	Explanation
GDAS	Global Data Assimilation System
GEOS-5	NASA Goddard Earth Observing System Model-5
GOCART	Goddard Chemistry Aerosol Radiation and Transport Model
GOES	Geostationary Operational Environmental Satellite
H_2O	Water/Water Vapor
H_2S	Hydrogen Sulfide
HNO_3	Nitric acid
HO_2	Hydroperoxyl radical
HALO	High Altitude and LOng range research aircraft
HAMP	HALO Microwave Package
HSRL	High Spectral Resolution Lidar
HYSPLIT	HYbrid Single Particle Lagrangian Integrated Trajectory model
ICAO	International Civil Aviation Organization
INP	Ice-Nucleating Particle
IPCC AR5	5^{th} Assessment Report of the Intergovernmental Panel on Climate Change
ITCZ	Inter-Tropical Convergence Zone
J2-Cell	Iodine Cell
KTP/$KTiOPO_4$	Potassium Titanyl Phosphate
LACE	Lindenberg Aerosol Characterization Experiment
libRadtran	library for Radiative transfer software package
lidar	LIght Detection And Ranging
LW	Long-Wave radiation (2.5-100.0 μm)
MBL	Marine Boundary Layer
MERLIN	MEthane Remote sensing LIdar missioN
MODIS	MODerate resolution Imaging Spectroradiometer
NARVAL	Next-generation Aircraft Remote-sensing for VALidation studies
NCEP	National Center for Environmental Prediction
Nd : $Y_3Al_5O_{12}$	Neodymium-doped Yttrium Aluminum
NO	Nitric Oxide
NO_2	Nitrogen Dioxide
NO_x	Nitrogen Oxides
O_3	Ozone
OA	Optical Analyzer
OPAC	Optical Properties of Aerosol and Clouds software package
OPO	Optical Parametric Oscillator
PBSC	Polarizing BeamSplitter Cube
PM	Photo-Multiplier
PRIDE	Puerto RIco Dust Experiment
RF	Research Flight
RTE	Radiative Transfer Equation
SABL	Saharan Atmospheric Boundary Layer
SAL	Saharan Air Layer
SALTRACE	Saharan Aerosol Long-range TRansport and Aerosol-Cloud-interaction Experiment
SAMUM	Saharan Mineral dUst experiMent
SHG	Second Harmonic Generator
SHL	Saharan Heat Low
SMART	Spectral Modular Airborne Radiation measurement sysTem
SO_2	Sulfur Dioxide
specMACS	spectrometer of the Munich Aerosol Cloud Scanner

Abbreviation	Explanation
SUR	SURface
SW	Short-Wave radiation (0.12-4.00 μm)
TOA	Top-Of-Atmosphere
TWI	Trade Wind Inversion
TBPB	ICAO-Code for the Grantley Adams International Airport
UTC	Coordinated Universal Time
WALES	WAter vapor Lidar Experiment in Space

List of Symbols

Symbol	Meaning	Unit
A	area of telescope	m^2
α	extinction coefficient	m^{-1}
$\alpha_\perp$	cross polarized component of the extinction coefficient	m^{-1}
$\alpha_\parallel$	parallel polarized component of the extinction coefficient	m^{-1}
α_{abs}	extinction due to absorption	m^{-1}
α_m	molecular extinction coefficient	m^{-1}
α_p	particle extinction coefficient	m^{-1}
α_{scat}	extinction due to scattering	m^{-1}
β	backscatter coefficient	$m^{-1}\,sr^{-1}$
β'	volume scattering cross section	m^{-1} or m^2m^{-3}
β_m	molecular backscatter coefficient	$m^{-1}\,sr^{-1}$
β_{off}	backscatter coefficient of offline wavelength (DIAL)	$m^{-1}\,sr^{-1}$
β_{on}	backscatter coefficient of online wavelength (DIAL)	$m^{-1}\,sr^{-1}$
β_p	particle backscatter coefficient	$m^{-1}\,sr^{-1}$
$\beta_{p\perp}$	cross polarized component of the particle backscatter coefficient	$m^{-1}\,sr^{-1}$
$\beta_{p\parallel}$	parallel polarized component of the particle backscatter coefficient	$m^{-1}\,sr^{-1}$
β_{tot}	total backscatter coefficient in a HSRL setup	$m^{-1}\,sr^{-1}$
c	speed of light	$m\,s^{-1}$
C	system constant of the lidar system	$m^3\,sr$
c_m	particle mass concentration	$\mu g\,m^{-3}$
C_m	system constant of the HSRL channel which detects the molecular signal	$m^3\,sr$
C_{off}	system constant of the offline DIAL channel	$m^3\,sr$
C_{on}	system constant of the online DIAL channel	$m^3\,sr$
$C_\perp$	system constant of the cross polarized channel	$m^3\,sr$
$C_\parallel$	system constant of the parallel polarized channel	$m^3\,sr$
c_p	specific heat capacity	$J\,kg^{-1}\,K^{-1}$
C_{tot}	system constant of the HSRL channel which detects the total signal	$m^3\,sr$
c_v	aerosol volume fraction	
CTH_{frac}	cloud top height fraction	
D_{dust}	arbitrary coefficient used for calculations in Section 2.4.2	sr
D_{marine}	arbitrary coefficient used for calculations in Section 2.4.2	sr
$\delta_\star$	signal ratio	
δ_m	volume linear depolarization ratio for air molecules	
δ_p	particle linear depolarization ratio	
δ_v	volume linear depolarization ratio	
ΔR	range resolution	m
Δz_{SAL}	vertical extent of the Saharan air layer	m
$E_\downarrow$	downwelling irradiance	$W\,m^{-2}$
$E_\uparrow$	upwelling irradiace	$W\,m^{-2}$
ϕ	angle between the plane of the PBSC and the plane of the laser beam	rad
$F^\downarrow$	downwelling radiative flux	W
$F^\uparrow$	upwelling radiative flux	W
F_{net}	radiative flux	W
g	gravitational acceleration of the Earth	$m\,s^{-2}$
I	radiance	$W\,m^2sr-1$

Symbol	Meaning	Unit
I_t	intensity of emitted laser light at distance r	$\mathrm{W\,m^2}$
I_r	intensity of received light at telescope	$\mathrm{W\,m^2}$
λ_{off}	offline wavelength in a DIAL setup	m
λ_{on}	online wavelength in a DIAL setup	m
$L_\nu(T)$	Planck function	$\mathrm{W\,m^2sr-1}$
N^2	squared Brunt-Väisälä frequency	$\mathrm{s^{-2}}$
N_{CT}	number of detected cloud tops	
ν_{dust}	factor for conversion of dust aerosol extinction to mass concentration	m
ν_{marine}	factor for conversion of marine aerosol extinction to mass concentration	m
Ω	solid angle	sr
ω_0	single scattering albedo	
P	probability	
$P_\perp$	cross polarized component of the light power	W
$P_\parallel$	parallel polarized component of the light power	W
P_0	power of emitted laser pulse	W
$P_{0[off]}$	power of emitted offline laser pulse (DIAL)	W
$P_{0[on]}$	power of emitted online laser pulse (DIAL)	W
P_m	molecular part of power received by the telescope of a HSRL system	W
$\boldsymbol{P}$	phase function	
$\boldsymbol{P_m}$	Rayleigh phase function	
P_p	light power parallel to the incident plane of the PBSC	W
P_R	reflected power component by the PBSC	W
P_s	light power perpendicular to the incident plane of the PBSC	W
P_T	transmitted power component by the PBSC	W
P_{tel}	power received from lidar telescope	W
P_{tot}	total power received by a telescope of a HSRL system	W
P_V	power of scattered light from illuminated volume	W
r	distance or radius	
$\boldsymbol{R}$	backscatter ratio	
ρ_{air}	density of air	$\mathrm{kg\,m^{-3}}$
ρ_{dust}	particle density of dust	$\mathrm{g\,cm^{-3}}$
ρ_{marine}	particle density of marine aerosol	$\mathrm{g\,cm^{-3}}$
r_m	water vapor mass mixing ratio	$\mathrm{g\,kg^{-1}}$
R_P	PBSC-reflectance for parallel polarized light	
R_S	PBSC-reflectance for perpendicular polarized light	
RE_{SUR}	radiative effect at surface level	$\mathrm{W\,m^{-2}}$
RE_{TOA}	radiative effect at top of the atmosphere	$\mathrm{W\,m^{-2}}$
RH	relative humidity	
Ri	Richardson number	
s	distance (radiative transfer)	m
S	flow shear	$\mathrm{s^{-2}}$
σ	standard deviation	
σ_{scat}	molecular scattering cross section (DIAL)	$\mathrm{m^2}$
σ_{abs}	molecular absorption cross section (DIAL)	$\mathrm{m^2}$
S_m	molecular lidar ratio	sr
S_p	particle lidar ratio	sr
sza	solar zenith angle	$^\circ$
T	temperature	K
t	time	s

Symbol	Meaning	Unit
t_0	time at emission of laser pulse	s
T_P	PBSC-transmittance for parallel polarized light	
t_r	preset time-interval for photon count	s
T_S	PBSC-transmittance for perpendicular polarized light	
τ	aerosol optical depth	
τ_L	length of laser pulse	s
τ_{SAL}	Saharan air layer aerosol optical depth	
τ_{tot}	aerosol optical depth from aircraft to ground level	
θ	laser beam divergence	rad
Θ	potential temperature	K
Θ_e	equivalent potential temperature	K
u	wind speed	$\mathrm{m\,s^{-2}}$
$\mathbf{u}$	wind component in east direction	$\mathrm{m\,s^{-2}}$
$\mathbf{v}$	wind component in north direction	$\mathrm{m\,s^{-2}}$
V	volume	$\mathrm{m^3}$
$V_\star$	relative amplification factor	
V_R	receivers optical loss and electronic amplification (reflected channel of PBSC)	
V_T	receivers optical loss and electronic amplification (reflected channel of PBSC)	
$wdir$	wind direction	$^\circ$
x	fraction x of dust contributing to total particle extinction coefficient	
$\tilde{x}$	size parameter	
z	altitude	m

Acknowledgements

This thesis is the result of my research at the Institute of Atmospheric Physics (IPA) of German Aerospace Center (DLR) during the past three and a half years. In the following I want to thank all the people who supported me during this time.
First and foremost, I want to thank Dr. Silke Groß for her outstanding guidance during the past years and for giving me the opportunity to work at DLR. Without her ideas and supervision this work would not have been possible. I would also like to thank Dr. Martin Wirth and Dr. Andreas Fix for teaching me how to operate the WALES lidar system and for many unforgettable moments during the field campaigns in Iceland, Ireland, Oberpfaffenhofen and Barbados. Furthermore, I want to thank Prof. Dr. Bernhard Mayer and Prof. Dr. Markus Rapp as well as Dr. Anke Roiger for their continuous support as supervisors and mentors. I also thank Dr. Claudia Emde and Prof. Dr. Bernhard Mayer for providing valuable advises concerning conducted radiative transfer calculations. Many thanks go to my colleagues and office mates Benedikt Urbanek, Robert Reichert, Eleni Tetoni, Eleni Marinou, Sebastian Wolff, Florian Ewald, Andreas Schäfler, Quitterie Cazenave and Benedikt Ehard for valuable interdisciplinary discussions, amusing coffee breaks and an incredibly nice working atmosphere. Last but not least, I want to thank the German Academic Exchange Service (DAAD) for granting me a PhD-scholarship at DLR and for the associated financial support.

All this would not have been possible without the tremendous support of Conny and my family. Thank you so much.

Bibliography

Adams, A. M., J. M. Prospero, and C. Zhang, 2012: CALIPSO-derived three-dimensional structure of aerosol over the Atlantic basin and adjacent continents. *J. Clim.*, **25 (19)**, 6862–6879, doi:10.1175/jcli-d-11-00672.1.

Amiri-Farahani, A., R. J. Allen, D. Neubauer, and U. Lohmann, 2017: Impact of Saharan dust on North Atlantic marine stratocumulus clouds: importance of the semidirect effect. *Atmos. Chem. Phys.*, **17 (10)**, 6305–6322, doi:10.5194/acp-17-6305-2017.

Anderson, G. P., S. A. Clough, F. X. Kneizys, J. H. Chetwynd, and E. P. Shettle, 1986: AFGL atmospheric constituent profiles (0-120 km). Tech. rep.

Ansmann, A., U. Wandinger, A. Wiedensohler, and U. Leiterer, 2002: Lindenberg aerosol characterization experiment 1998 (LACE 98): Overview. *J. Geophys. Res.-Atmos.*, **107 (D21)**, doi:10.1029/2000jd000233.

Ansmann, A., and Coauthors, 2003: Long-range transport of Saharan dust to northern Europe: The 11-16 October 2001 outbreak observed with EARLINET. *J. Geophys. Res.-Atmos*, **108 (D24)**, doi:10.1029/2003jd003757.

Ansmann, A., and Coauthors, 2008: Influence of Saharan dust on cloud glaciation in southern Morocco during the Saharan Mineral Dust Experiment. *J. Geophys. Res.*, **113 (D4)**, doi:10.1029/2007jd008785.

Ansmann, A., and Coauthors, 2011: Saharan mineral dust experiments SAMUM-1 and SAMUM-2: what have we learned? *Tellus B*, **63 (4)**, 403–429, doi:10.1111/j.1600-0889.2011.00555.x.

Bauer, S. E., and D. Koch, 2005: Impact of heterogeneous sulfate formation at mineral dust surfaces on aerosol loads and radiative forcing in the Goddard Institute for Space Studies general circulation model. *J. Geophys. Res.*, **110 (D17)**, doi:10.1029/2005jd005870.

Bègue, N., P. Tulet, J. Pelon, B. Aouizerats, A. Berger, and A. Schwarzenboeck, 2015: Aerosol processing and CCN formation of an intense Saharan dust plume during the EUCAARI 2008 campaign. *Atmos. Chem. Phys.*, **15 (6)**, 3497–3516, doi:10.5194/acp-15-3497-2015.

Behrendt, A., and T. Nakamura, 2002: Calculation of the calibration constant of polarization lidar and its dependency on atmospheric temperature. *Opt. Express*, **10 (16)**, 805, doi:10.1364/oe.10.000805.

Bellouin, N., O. Boucher, M. Vesperini, and D. Tanré, 2004: Estimating the direct aerosol radiative perturbation: impact of ocean surface representation and aerosol non-sphericity. *Q. J. Roy. Meteor. Soc.*, **130 (601)**, 2217–2232, doi:10.1256/qj.03.136.

Biagio, C. D., Y. Balkanski, S. Albani, O. Boucher, and P. Formenti, 2020: Direct radiative effect by mineral dust aerosols constrained by new microphysical and spectral optical data. *Geophys. Res. Lett.*, **47 (2)**, doi:10.1029/2019gl086186.

Bian, H., and C. S. Zender, 2003: Mineral dust and global tropospheric chemistry: Relative roles of photolysis and heterogeneous uptake. *J. Geophys. Res.-Atmos*, **108 (D21)**, doi:10.1029/2002jd003143.

Biele, J., G. Beyerle, and G. Baumgarten, 2000: Polarization lidar: Corrections of instrumental effects. *Opt. Express*, **7 (12)**, 427–435, doi:10.1364/OE.7.000427.

Bony, S., and B. Stevens, 2019: Measuring area-averaged vertical motions with dropsondes. *J. Atmos. Sci.*, **76 (3)**, 767–783, doi:10.1175/jas-d-18-0141.1.

Boose, Y., and Coauthors, 2016: Ice nucleating particles in the Saharan air layer. *Atmos. Chem. Phys.*, **16 (14)**, 9067–9087, doi:10.5194/acp-16-9067-2016.

Buras, R., T. Dowling, and C. Emde, 2011: New secondary-scattering correction in DISORT with increased efficiency for forward scattering. *J. Quant. Spectrosc. Ra.*, **112 (12)**, 2028–2034, doi:10.1016/j.jqsrt.2011.03.019.

Buras, R., and B. Mayer, 2011: Efficient unbiased variance reduction techniques for monte carlo simulations of radiative transfer in cloudy atmospheres: the solution. *J. Quant. Spectrosc. Ra.*, **112 (3)**, 434–447, doi:10.1016/j.jqsrt.2010.10.005.

Burpee, R. W., 1972: The origin and structure of easterly waves in the lower troposphere of North Africa. *J. Atmos. Sci.*, **29 (1)**, 77–90, doi:10.1175/1520-0469(1972)029⟨0077:toasoe⟩2.0.co;2.

Burton, S. P., and Coauthors, 2012: Aerosol classification using airborne high spectral resolution lidar measurements – methodology and examples. *Atmos. Meas. Tech.*, **5 (1)**, 73–98, doi:10.5194/amt-5-73-2012.

Cakmur, R. V., and Coauthors, 2006: Constraining the magnitude of the global dust cycle by minimizing the difference between a model and observations. *J. Geophys. Res.*, **111 (D6)**, doi:10.1029/2005jd005791.

Carlson, T. N., and J. M. Prospero, 1972: The large-scale movement of Saharan air outbreaks over the northern equatorial Atlantic. *J. Appl. Meteorol.*, **11 (2)**, 283–297, doi:10.1175/1520-0450(1972)011⟨0283:TLSMOS⟩2.0.CO;2.

Chiapello, I., G. Bergametti, L. Gomes, B. Chatenet, F. Dulac, J. Pimenta, and E. S. Suares, 1995: An additional low layer transport of Sahelian and Saharan dust over the north-eastern tropical Atlantic. *Geophys. Res.Lett.*, **22 (23)**, 3191–3194, doi:10.1029/95gl03313.

Cook, K. H., 1999: Generation of the African easterly jet and its role in determining west african precipitation. *J. Clim.*, **12 (5)**, 1165–1184, doi:10.1175/1520-0442(1999)012⟨1165:gotaej⟩2.0.co;2.

Cox, C., and W. Munk, 1954a: Measurement of the roughness of the sea surface from photographs of the sun's glitter. *J. Opt. Soc. Am.*, **44 (11)**, 838–850, doi:10.1364/JOSA.44.000838.

Cox, C., and W. Munk, 1954b: Statistics of the sea surface derived from sun glitter. *J. Mar. Res.*, **13 (2)**, 198–227.

de Longueville, F., P. Ozer, S. Doumbia, and S. Henry, 2012: Desert dust impacts on human health: an alarming worldwide reality and a need for studies in West Africa. *Int. J. Biometeorol.*, **57 (1)**, 1–19, doi:10.1007/s00484-012-0541-y.

DeMott, P. J., and Coauthors, 2015: Integrating laboratory and field data to quantify the immersion freezing ice nucleation activity of mineral dust particles. *Atmos. Chem. Phys.*, **15 (1)**, 393–409, doi:10.5194/acp-15-393-2015.

Denjean, C., and Coauthors, 2015: Long-range transport across the Atlantic in summertime does not enhance the hygroscopicity of African mineral dust. *Geophys. Res. Lett.*, **42 (18)**, 7835–7843, doi:10.1002/2015gl065693.

Dunion, J. P., and C. S. Velden, 2004: The impact of the Saharan air layer on Atlantic tropical cyclone activity. *B. Am. Meteorol. Soc.*, **85 (3)**, 353–366, doi:10.1175/BAMS-85-3-353.

Ehret, G., and Coauthors, 2017: MERLIN: A French-German space lidar mission dedicated to atmospheric methane. *Remote Sens.*, **9 (10)**, 1052, doi:10.3390/rs9101052.

Elterman, L., 1951: The measurement of stratospheric density distribution with the searchlight technique. *J. Geophys. Res.*, **56 (4)**, 509–520, doi:10.1029/JZ056i004p00509.

Elterman, L., 1966: Aerosol measurements in the troposphere and stratosphere. *Appl. Opt.*, **5 (11)**, 1769–1776, doi:10.1364/AO.5.001769.

Emde, C., R. Buras, and B. Mayer, 2011: ALIS: An efficient method to compute high spectral resolution polarized solar radiances using the Monte Carlo approach. *J. Quant. Spectrosc. Ra.*, **112 (10)**, 1622–1631, doi:10.1016/j.jqsrt.2011.03.018.

Emde, C., R. Buras, B. Mayer, and M. Blumthaler, 2010: The impact of aerosols on polarized sky radiance: model development, validation, and applications. *Atmos. Chem. Phys.*, **10 (2)**, 383–396, doi:10.5194/acp-10-383-2010.

Emde, C., and B. Mayer, 2007: Simulation of solar radiation during a total eclipse: a challenge for radiative transfer. *Atmos. Chem. Phys.*, **7 (9)**, 2259–2270, doi:10.5194/acp-7-2259-2007.

Emde, C., and Coauthors, 2016: The libRadtran software package for radiative transfer calculations (version 2.0.1). *Geosci. Model Dev.*, **9 (5)**, 1647–1672, doi:10.5194/gmd-9-1647-2016.

Esselborn, M., M. Wirth, A. Fix, M. Tesche, and G. Ehret, 2008: Airborne high spectral resolution lidar for measuring aerosol extinction and backscatter coefficients. *Appl. Opt.*, **47 (3)**, 346–358, doi:10.1364/AO.47.000346.

Ewald, F., S. Groß, M. Hagen, L. Hirsch, J. Delanoë, and M. Bauer-Pfundstein, 2019: Calibration of a 35 GHz airborne cloud radar: lessons learned and intercomparisons with 94 GHz cloud radars. *Atmos. Meas. Tech.*, **12 (3)**, 1815–1839, doi:10.5194/amt-12-1815-2019.

Ewald, F., T. Kölling, A. Baumgartner, T. Zinner, and B. Mayer, 2016: Design and characterization of specMACS, a multipurpose hyperspectral cloud and sky imager. *Atmos. Meas. Tech.*, **9 (5)**, 2015–2042, doi:10.5194/amt-9-2015-2016.

Falkovich, A. H., E. Ganor, Z. Levin, P. Formenti, and Y. Rudich, 2001: Chemical and mineralogical analysis of individual mineral dust particles. *J. Geophys. Res.-Atmos*, **106 (D16)**, 18 029–18 036, doi:10.1029/2000jd900430.

Fischer, H., M.-L. Siggaard-Andersen, U. Ruth, R. Röthlisberger, and E. Wolff, 2007: Glacial/interglacial changes in mineral dust and sea-salt records in polar ice cores: sources, transport, and deposition. *Rev. Geophys.*, **45 (1)**, doi:10.1029/2005rg000192.

Foltz, G. R., and M. J. McPhaden, 2008: Impact of Saharan dust on tropical North Atlantic SST. *J. Clim.*, **21 (19)**, 5048–5060, doi:10.1175/2008jcli2232.1.

Freudenthaler, V., and Coauthors, 2009: Depolarization ratio profiling at several wavelengths in pure Saharan dust during SAMUM 2006. *Tellus B*, **61 (1)**, 165–179, doi:10.1111/j.1600-0889.2008.00396.x.

Fu, Q., and K. N. Liou, 1992: On the correlated k-distribution method for radiative transfer in nonhomogeneous atmospheres. *J. Atmos. Sci.*, **49 (22)**, 2139–2156, doi:10.1175/1520-0469(1992)049⟨2139:OTCDMF⟩2.0.CO;2.

Gamage, N., and C. Hagelberg, 1993: Detection and analysis of microfronts and associated coherent events using localized transforms. *J. Atmos. Sci*, **50**, 750–756, doi:10.1175/1520-0469(1993)050⟨0750:daaoma⟩2.0.co;2.

Gamo, M., 1996: Thickness of the dry convection and large-scale subsidence above deserts. *Bound-Lay. Meteorol.*, **79 (3)**, 265–278, doi:10.1007/BF00119441.

Gasteiger, J., S. Groß, D. Sauer, M. Haarig, A. Ansmann, and B. Weinzierl, 2017: Particle settling and vertical mixing in the Saharan air layer as seen from an integrated model, lidar, and in situ perspective. *Atmos. Chem. Phys.*, **17 (1)**, 297–311, doi:10.5194/acp-17-297-2017.

Gasteiger, J., M. Wiegner, S. Groß, V. Freudenthaler, C. Toledano, M. Tesche, and K. Kandler, 2011: Modelling lidar-relevant optical properties of complex mineral dust aerosols. *Tellus B*, **63 (4)**, 725–741, doi:10.1111/j.1600-0889.2011.00559.x.

Ginoux, P., J. M. Prospero, T. E. Gill, N. C. Hsu, and M. Zhao, 2012: Global-scale attribution of anthropogenic and natural dust sources and their emission rates based on MODIS Deep Blue aerosol products. *Rev. Geophys.*, **50 (3)**, doi:10.1029/2012rg000388.

Gobbi, G., F. Barnaba, M. Blumthaler, G. Labow, and J. Herman, 2002: Observed effects of particles nonsphericity on the retrieval of marine and desert dust aerosol optical depth by lidar. *Atmos. Res.*, **61 (1)**, 1–14, doi:10.1016/s0169-8095(01)00104-1.

Griffin, D. W., 2007: Atmospheric movement of microorganisms in clouds of desert dust and implications for human health. *Clin. Microbiol. Rev.*, **20 (3)**, 459–477, doi:10.1128/cmr.00039-06.

Groß, S., M. Esselborn, B. Weinzierl, M. Wirth, A. Fix, and A. Petzold, 2013: Aerosol classification by airborne high spectral resolution lidar observations. *Atmos. Chem. Phys.*, **13 (5)**, 2487–2505, doi:10.5194/acp-13-2487-2013.

Groß, S., V. Freudenthaler, K. Schepanski, C. Toledano, A. Schäfler, A. Ansmann, and B. Weinzierl, 2015: Optical properties of long-range transported Saharan dust over Barbados as measured by dual-wavelength depolarization Raman lidar measurements. *Atmos. Chem. Phys*, **15 (19)**, 11 067–11 080, doi:10.5194/acp-15-11067-2015.

Groß, S., J. Gasteiger, V. Freudenthaler, T. Müller, D. Sauer, C. Toledano, and A. Ansmann, 2016: Saharan dust contribution to the Caribbean summertime boundary layer – a lidar study during SALTRACE. *Atmos. Chem. Phys*, **16 (18)**, 11 535–11 546, doi:10.5194/acp-16-11535-2016.

Groß, S., M. Tesche, V. Freudenthaler, C. Toledano, M. Wiegner, A. Ansmann, D. Althausen, and M. Seefeldner, 2011a: Characterization of saharan dust, marine aerosols and mixtures of biomass-burning aerosols and dust by means of multi-wavelength depolarization and Raman lidar measurements during SAMUM 2. *Tellus B*, **63 (4)**, 706–724, doi:10.1111/j.1600-0889.2011.00556.x.

Groß, S., M. Wiegner, V. Freudenthaler, and C. Toledano, 2011b: Lidar ratio of Saharan dust over Cape Verde islands: Assessment and error calculation. *J. Geophys. Res.-Atmos.*, **116 (D15)**, doi:10.1029/2010JD015435, d15203.

Groß, S., M. Wirth, and M. Esselborn, 2012: *Atmospheric Physics*. Springer Berlin Heidelberg, 477-486 pp., doi:10.1007/978-3-642-30183-4.

Grousset, F. E., P. Ginoux, A. Bory, and P. E. Biscaye, 2003: Case study of a Chinese dust plume reaching the French Alps. *Geophys. Res. Lett.*, **30 (6)**, doi:10.1029/2002gl016833.

Gutleben, M., S. Groß, and M. Wirth, 2019a: Cloud macro-physical properties in Saharan-dust-laden and dust-free North Atlantic trade wind regimes: a lidar case study. *Atmos. Chem. Phys.*, **19 (16)**, 10 659–10 673, doi:10.5194/acp-19-10659-2019.

Gutleben, M., S. Groß, M. Wirth, C. Emde, and B. Mayer, 2019b: Impacts of water vapor on Saharan air layer radiative heating. *Geophys. Res. Lett.*, **46 (24)**, 14 854–14 862, doi:10.1029/2019GL085344.

Gutleben, M., S. Groß, M. Wirth, and B. Mayer, 2020: Radiative effects of long-range-transported Saharan air layers as determined from airborne lidar measurements. *Atmos. Chem. Phys. Disscus.*, doi:10.5194/acp-2020-420.

Haarig, M., A. Ansmann, H. Baars, C. Jimenez, I. Veselovskii, R. Engelmann, and D. Althausen, 2018: Depolarization and lidar ratios at 355, 532, and 1064 nm and microphysical properties of aged tropospheric and stratospheric Canadian wildfire smoke. *Atmos. Chem. Phys.*, **18 (16)**, 11 847–11 861, doi:10.5194/acp-18-11847-2018.

Hatch, C. D., P. R. Tumminello, M. A. Cassingham, A. L. Greenaway, R. Meredith, and M. J. Christie, 2019: Technical note: Frenkel, Halsey and Hill analysis of water on clay minerals: toward closure between cloud condensation nuclei activity and water adsorption. *Atmos. Chem. Phys.*, **19 (21)**, 13 581–13 589, doi:10.5194/acp-19-13581-2019.

Heintzenberg, J., 2009: The SAMUM-1 experiment over southern Morocco: overview and introduction. *Tellus B*, **61 (1)**, 2–11, doi:10.1111/j.1600-0889.2008.00403.x.

Hess, M., P. Koepke, and I. Schult, 1998: Optical properties of aerosols and clouds: The software package OPAC. *B. Am. Meteorol. Soc*, **79 (5)**, 831–844, doi:10.1175/1520-0477(1998)079⟨0831:opoaac⟩2.0.co;2.

Hoose, C., and O. Möhler, 2012: Heterogeneous ice nucleation on atmospheric aerosols: a review of results from laboratory experiments. *Atmos. Chem. Phys.*, **12 (20)**, 9817–9854, doi:10.5194/acp-12-9817-2012.

Hulburt, E. O., 1937: Observations of a searchlight beam to an altitude of 28 kilometers. *J. Opt. Soc. Am.*, **27 (11)**, 377–382, doi:10.1364/JOSA.27.000377.

Huneeus, N., and Coauthors, 2011: Global dust model intercomparison in AeroCom phase I. *Atmos. Chem. Phys.*, **11 (15)**, 7781–7816, doi:10.5194/acp-11-7781-2011.

Illingworth, A. J., and Coauthors, 2015: The EarthCARE Satellite: the next step forward in global measurements of clouds, aerosols, precipitation, and radiation. *B. Am. Meteoro.l Soc.*, **96 (8)**, 1311–1332, doi:10.1175/BAMS-D-12-00227.1.

IPCC, 2013: *Climate Change 2013: The Physical Science Basis. Contribution of Working Group I to the Fifth Assessment Report of the Intergovernmental Panel on Climate Change*. Cambridge University Press, Cambridge, United Kingdom and New York, NY, USA, 1535 pp.

Ismail, S., and Coauthors, 2010: LASE measurements of water vapor, aerosol, and cloud distributions in Saharan air layers and tropical disturbances. *J. Atmos. Sci.*, **67 (4)**, 1026–1047, doi:10.1175/2009JAS3136.1.

Jickells, T. D., 2005: Global iron connections between desert dust, ocean biogeochemistry, and climate. *Science*, **308 (5718)**, 67–71, doi:10.1126/science.1105959.

Johnson, E. A., R. C. Meyer, R. E. Hopkins, and W. H. Mock, 1939: The measurement of light scattered by the upper atmosphere from a search-light beam. *J. Opt. Soc. Am.*, **29 (12)**, 512–517, doi:10.1364/JOSA.29.000512.

Jones, C., N. Mahowald, and C. Luo, 2003: The role of easterly waves on African desert dust transport. *Jo. Clim.*, **16 (22)**, 3617–3628, doi:10.1175/1520-0442(2003)016⟨3617:troewo⟩2.0.co;2.

Jung, E., B. Albrecht, J. M. Prospero, H. H. Jonsson, and S. M. Kreidenweis, 2013: Vertical structure of aerosols, temperature, and moisture associated with an intense African dust event observed over the eastern Caribbean. *J. Geophys. Res.-Atmos.*, **118 (10)**, 4623–4643, doi:10.1002/jgrd.50352.

Kaaden, N., and Coauthors, 2009: State of mixing, shape factor, number size distribution, and hygroscopic growth of the Saharan anthropogenic and mineral dust aerosol at Tinfou, Morocco. *Tellus B*, **61 (1)**, 51–63, doi:10.1111/j.1600-0889.2008.00388.x.

Kahnert, M., T. Nousianen, and B. Veihelmann, 2005: Spherical and spheroidal model particles as an error source in aerosol climate forcing and radiance computations: A case study for feldspar aerosols. *J. Geophys. Res.-Atmos.*, **110 (D18)**, doi:10.1029/2004jd005558.

Kandler, K., and Coauthors, 2009: Size distribution, mass concentration, chemical and mineralogical composition and derived optical parameters of the boundary layer aerosol at Tinfou, Morocco, during SAMUM 2006. *Tellus B*, **61 (1)**, 32–50, doi:10.1111/j.1600-0889.2008.00385.x.

Kandler, K., and Coauthors, 2011: Electron microscopy of particles collected at Praia, Cape Verde, during the Saharan Mineral Dust Experiment: particle chemistry, shape, mixing state and complex refractive index. *Tellus B*, **63 (4)**, 475–496, doi:10.1111/j.1600-0889.2011.00550.x.

Kanitz, T., A. Ansmann, P. Seifert, R. Engelmann, J. Kalisch, and D. Althausen, 2013: Radiative effect of aerosols above the northern and southern Atlantic Ocean as determined from shipborne lidar observations. *J. Geophys. Res.-Atmos.*, **118 (22)**, 12,556–12,565, doi:10.1002/2013jd019750.

Kanitz, T., R. Engelmann, B. Heinold, H. Baars, A. Skupin, and A. Ansmann, 2014: Tracking the Saharan air layer with shipborne lidar across the tropical Atlantic. *Geophys. Res. Lett.*, **41 (3)**, 1044–1050, doi:10.1002/2013gl058780.

Karyampudi, V. M., and Coauthors, 1999: Validation of the Saharan dust plume conceptual model using lidar, Meteosat, and ECMWF data. *B. Am. Meteorol. Soc.*, **80 (6)**, 1045–1075, doi:10.1175/1520-0477(1999)080⟨1045:VOTSDP⟩2.0.CO;2.

Karydis, V. A., P. Kumar, D. Barahona, I. N. Sokolik, and A. Nenes, 2011: On the effect of dust particles on global cloud condensation nuclei and cloud droplet number. *J. Geophys. Res.-Atmos.*, **116 (D23)**, doi:10.1029/2011jd016283.

Kato, S., T. P. Ackerman, J. H. Mather, and E. E. Clothiaux, 1999: The k-distribution method and correlated-k approximation for a shortwave radiative transfer model. *J. Quant. Spectrosc. Ra.*, **62 (1)**, 109–121, doi:10.1016/s0022-4073(98)00075-2.

Kiemle, C., and Coauthors, 2008: First airborne water vapor lidar measurements in the tropical upper troposphere and mid-latitudes lower stratosphere: accuracy evaluation and intercomparisons with other instruments. *Atmos. Chem. Phys.*, **8 (17)**, 5245–5261, doi:10.5194/acp-8-5245-2008.

Kim, S., S. Yoon, A. Jefferson, J. Won, E. G. Dutton, J. A. Ogren, and T. L. Anderson, 2004: Observation of enhanced water vapor in Asian dust layer and its effect on atmospheric radiative heating rates. *Geophys. Res. Lett.*, **31 (18)**, doi:10.1029/2004gl020024.

Kinne, S., and Coauthors, 2006: An AeroCom initial assessment – optical properties in aerosol component modules of global models. *Atmos. Chem. Phys.*, **6 (7)**, 1815–1834, doi:10.5194/acp-6-1815-2006.

Klepp, C., F. Ament, S. Bakan, L. Hirsch, and B. Stevens, 2014: NARVAL campaign reoprt. Report, Max Planck Institiut für Meteorologie.

Klett, J. D., 1981: Stable analytical inversion solution for processing lidar returns. *Appl. Opt.*, **20 (2)**, 211–220, doi:10.1364/AO.20.000211.

Knippertz, P., and M. C. Todd, 2010: The central west Saharan dust hot spot and its relation to African easterly waves and extratropical disturbances. *J. Geophys. Res.*, **115 (D12)**, doi:10.1029/2009jd012819.

Koepke, P., J. Gasteiger, and M. Hess, 2015: Technical note: Optical properties of desert aerosol with non-spherical mineral particles: data incorporated to OPAC. *Atmos. Chem. Phys.*, **15 (10)**, 5947–5956, doi:10.5194/acp-15-5947-2015.

Koepke, P., and M. Hess, 1988: Scattering functions of tropospheric aerosols: the effects of non-spherical particles. *Appl. Opt.*, **27 (12)**, 2422, doi:10.1364/ao.27.002422.

Krautstrunk, M., and A. Giez, 2012: The transition from FALCON to HALO era airborne atmospheric research. *Atmospheric Physics*, U. Schumann, Ed., Research Topics in Aerospace, Springer Berlin Heidelberg, 609–624.

Kulmala, M., and Coauthors, 2009: Introduction: European integrated project on aerosol cloud climate and air quality interactions (EUCAARI) – integrating aerosol research from nano to global scales. *Atmos. Chem. Phys.*, **9 (8)**, 2825–2841, doi:10.5194/acp-9-2825-2009.

Kumar, P., I. N. Sokolik, and A. Nenes, 2009: Parameterization of cloud droplet formation for global and regional models: including adsorption activation from insoluble CCN. *Atmos. Chem. Phys.*, **9 (7)**, 2517–2532, doi:10.5194/acp-9-2517-2009.

Kumar, P., I. N. Sokolik, and A. Nenes, 2011: Measurements of cloud condensation nuclei activity and droplet activation kinetics of fresh unprocessed regional dust samples and minerals. *Atmos. Chem. Phys.*, **11 (7)**, 3527–3541, doi:10.5194/acp-11-3527-2011.

Kylling, A., K. Stamnes, and S. C. Tsay, 1995: A reliable and efficient two-stream algorithm for spherical radiative transfer: documentation of accuracy in realistic layered media. *J. Atmos. Chem.*, **21 (2)**, 115–150, doi:10.1007/bf00696577.

Laaksonen, A., 2015: A unifying model for adsorption and nucleation of vapors on solid surfaces. *J. Phys. Chem. A*, **119 (16)**, 3736–3745, doi:10.1021/acs.jpca.5b00325.

Li, F., A. M. Vogelmann, and V. Ramanathan, 2004: Saharan dust aerosol radiative forcing measured from space. *J. Clim.*, **17 (13)**, 2558–2571, doi:10.1175/1520-0442(2004)017⟨2558:sdarfm⟩2.0.co;2.

Lilly, D. K., 1968: Models of cloud-topped mixed layers under a strong inversion. *Q. J. Roy. Meteor. Soc.*, **94 (401)**, 292–309, doi:10.1002/qj.49709440106.

Liou, K. N., and H. Lahore, 1974: Laser sensing of cloud composition: A backscattered depolarization technique. *J. Appl. Meteorol.*, **13 (2)**, 257–263, doi:10.1175/1520-0450(1974)013⟨0257:lsocca⟩2.0.co;2.

Liu, Z., M. A. Vaughan, D. M. Winker, C. A. Hostetler, L. R. Poole, D. Hlavka, W. Hart, and M. M., 2004: Use of probability distribution functions for discriminating between cloud and aerosol in lidar backscatter data. *J. Geophys. Res.*, **109 (D15)**, doi:10.1029/2004jd004732.

Lonitz, K., B. Stevens, L. Nuijens, V. Sant, L. Hirsch, and A. Seifert, 2015: The signature of aerosols and meteorology in long-term cloud radar observations of trade wind cumuli. *J. Atmos. Sci.*, **72 (12)**, 4643–4659, doi:10.1175/jas-d-14-0348.1.

Mahnke, P., H. Klingenberg, A. Fix, and M. Wirth, 2007: Dependency of injection seeding and spectral purity of a single resonant KTP optical parametric oscillator on the phase matching condition. *Applied Physics B*, **89 (1)**, 1–7, doi:10.1007/s00340-007-2746-z.

Mahowald, N. M., D. R. Muhs, S. Levis, P. J. Rasch, M. Yoshioka, C. S. Zender, and C. Luo, 2006: Change in atmospheric mineral aerosols in response to climate: last glacial period, preindustrial, modern, and doubled carbon dioxide climates. *J. Geophys. Res.- Atmos.*, **111 (D10)**, doi:10.1029/2005jd006653.

Maiman, T. H., 1960: Stimulated optical radiation in ruby. *Nature*, **187 (4736)**, 493–494, doi:10.1038/187493a0.

Mallet, M., P. Tulet, D. Serça, F. Solmon, O. Dubovik, J. Pelon, V. Pont, and O. Thouron, 2009: Impact of dust aerosols on the radiative budget, surface heat fluxes, heating rate profiles and convective activity over West Africa during March 2006. *Atmos. Chem. Phys.*, **9 (18)**, 7143–7160, doi:10.5194/acp-9-7143-2009.

Mamouri, R.-E., and A. Ansmann, 2016: Potential of polarization lidar to provide profiles of CCN- and INP-relevant aerosol parameters. *Atmos. Chem. Phys*, **16 (9)**, 5905–5931, doi:10.5194/acp-16-5905-2016.

Marsham, J. H., D. J. Parker, C. M. Grams, B. T. Johnson, W. M. F. Grey, and A. N. Ross, 2008: Observations of mesoscale and boundary-layer scale circulations affecting dust transport and uplift over the Sahara. *Atmos. Chem. Phys.*, **8 (23)**, 6979–6993, doi:10.5194/acp-8-6979-2008.

Martin, J. H., M. Gordon, and S. E. Fitzwater, 1991: The case for iron. *Limnol. Oceanogr.*, **36 (8)**, 1793–1802, doi:10.4319/lo.1991.36.8.1793.

Mayer, B., 2009: Radiative transfer in the cloudy atmosphere. *Eur. Phys. J. Conf.*, **1**, 75–99, doi:10.1140/epjconf/e2009-00912-1.

Mayer, B., and A. Kylling, 2005: Technical note: The libRadtran software package for radiative transfer calculations - description and examples of use. *Atmos. Chem. Phys.*, **5 (7)**, 1855–1877, doi:10.5194/acp-5-1855-2005.

McClung, F. J., and R. W. Hellwarth, 1962: Giant optical pulsations from ruby. *J. Appl. Phys.*, **33 (3)**, 828–829, doi:10.1063/1.1777174.

Mech, M., E. Orlandi, S. Crewell, F. Ament, L. Hirsch, M. Hagen, G. Peters, and B. Stevens, 2014: HAMP - the microwave package on the High Altitude and LOng range research aircraft (HALO). *Atmos. Meas. Tech.*, **7 (12)**, 4539–4553, doi:10.5194/amt-7-4539-2014.

Medeiros, B., L. Nuijens, C. Antoniazzi, and B. Stevens, 2010: Low-latitude boundary layer clouds as seen by CALIPSO. *J. Geophys. Res.-Atmos.*, **115**, doi:10.1029/2010JD014437.

Meng, L., H. W. Gao, Y. Yu, X. H. Yao, Y. Gao, C. Zhang, and L. Fan, 2017: A new approach developed to study variability in North African dust transport routes over the Atlantic during 2001–2015. *Geophys. Res. Lett.*, **44 (19)**, doi:10.1002/2017gl074478.

Messager, C., D. J. Parker, O. Reitebuch, A. Agusti-Panareda, C. M. Taylor, and J. Cuesta, 2009: Structure and dynamics of the Saharan atmospheric boundary layer during the West African monsoon onset: observations and analyses from the research flights of 14 and 17 July 2006. *Q. J. R. Meteorol. Soc.*, **136 (S1)**, 107–124, doi:10.1002/qj.469.

Mie, G., 1908: Beiträge zur Optik trüber Medien, speziell kolloidaler Metallösungen. *Ann. Phys.*, **330 (3)**, 377–445, doi:10.1002/andp.19083300302.

Mishchenko, M. I., L. D. Travis, R. A. Kahn, and R. A. West, 1997: Modeling phase functions for dustlike tropospheric aerosols using a shape mixture of randomly oriented polydisperse spheroids. *J. Geophys. Res.-Atmos.*, **102 (D14)**, 16 831–16 847, doi:10.1029/96jd02110.

Murayama, T., H. Okamoto, N. Kaneyasu, H. Kamataki, and K. Miura, 1999: Application of lidar depolarization measurement in the atmospheric boundary layer: Effects of dust and sea-salt particles. *J. Geophys. Res.-Atmos.*, **104 (D24)**, 31 781–31 792, doi:10.1029/1999jd900503.

Naumann, A. K., B. Stevens, C. Hohenegger, and J. P. Mellado, 2017: A conceptual model of a shallow circulation induced by prescribed low-level radiative cooling. *J. Atmos. Sci.*, **74 (10)**, 3129–3144, doi:10.1175/jas-d-17-0030.1.

NOAA National Centers for Environmental Information, 2020: State of the Climate: Global Climate Report for Annual 2019. published online January 2020, retrieved on May 20, 2020 from https://www.ncdc.noaa.gov/sotc/global/201913.

Nousiainen, T., 2009: Optical modeling of mineral dust particles: A review. *J. Quant. Spectrosc. Ra.*, **110 (14-16)**, 1261–1279, doi:10.1016/j.jqsrt.2009.03.002.

Nuijens, L., I. Serikov, L. Hirsch, K. Lonitz, and B. Stevens, 2014: The distribution and variability of low-level cloud in the North Atlantic trades. *Q. J. Roy. Meteor. Soc.*, **140 (684)**, 2364–2374, doi:10.1002/qj.2307.

Nuijens, L., and B. Stevens, 2012: The influence of wind speed on shallow marine cumulus convection. *J. Atmos. Sci.*, **69 (1)**, 168–184, doi:10.1175/jas-d-11-02.1.

Nuijens, L., B. Stevens, and A. P. Siebesma, 2009: The environment of precipitating shallow cumulus convection. *J. Atmos. Sci.*, **66 (7)**, 1962–1979, doi:10.1175/2008JAS2841.1.

Okin, G. S., N. Mladenov, L. Wang, D. Cassel, K. K. Caylor, S. Ringrose, and S. A. Macko, 2008: Spatial patterns of soil nutrients in two Southern African savannas. *J. Geophys. Res.-Biogeosci.*, **113 (G2)**, n/a–n/a, doi:10.1029/2007jg000584.

Painter, T. H., A. P. Barrett, C. C. Landry, J. C. Neff, M. P. Cassidy, C. R. Lawrence, K. E. McBride, and G. L. Farmer, 2007: Impact of disturbed desert soils on duration of mountain snow cover. *Geophys. Res. Lett.*, **34 (12)**, doi:10.1029/2007gl030284.

Papayannis, A., and Coauthors, 2008: Systematic lidar observations of Saharan dust over Europe in the frame of EARLINET (2000–2002). *J. Geophys. Res.*, **113 (D10)**, doi:10.1029/2007jd009028.

Patadia, F., E.-S. Yang, and S. A. Christopher, 2009: Does dust change the clear sky top of atmosphere shortwave flux over high surface reflectance regions? *Geophys. Res. Lett.*, **36 (15)**, doi:10.1029/2009gl039092.

Polavarapu, R., and G. Austin, 1979: A review of the GARP atlantic tropical experiment (gate). *Atmos. Ocean*, **17 (1)**, 1–13, doi:10.1080/07055900.1979.9649047.

Prospero, J. M., 2002: Environmental characterization of global sources of atmospheric soil dust identified with the NIMBUS 7 total ozone mapping spectrometer (TOMS) absorbing aerosol product. *Rev. Geophys.*, **40 (1)**, doi:10.1029/2000rg000095.

Prospero, J. M., and T. N. Carlson, 1972: Vertical and areal distribution of Saharan dust over the western equatorial North Atlantic Ocean. *J. Geophys. Res*, **77 (27)**, 5255–5265, doi:10.1029/JC077i027p05255.

Prospero, J. M., and P. J. Lamb, 2003: African droughts and dust transport to the Caribbean: climate change implications. *Science*, **302 (5647)**, 1024–1027, doi:10.1126/science.1089915.

Prospero, J. M., W. M. Landing, and M. Schulz, 2010: African dust deposition to Florida: Temporal and spatial variability and comparisons to models. *J. Geophys. Res.*, **115 (D13)**, doi:10.1029/2009jd012773.

Pruppacher, H. R., and J. D. Klett, 2010: *Microphysics of Clouds and Precipitation*. Springer Science + Business Media B.V, Dordrecht.

Raman, C. V., and K. S. Krishnan, 1928: A new type of secondary radiation. *Nature*, **121 (3048)**, 501–502, doi:10.1038/121501c0.

Reid, J. S., 2002: Dust vertical distribution in the Caribbean during the Puerto Rico Dust Experiment. *Geophys. Res. Lett.*, **29 (7)**, doi:10.1029/2001gl014092.

Sakai, T., T. Nagai, Y. Zaizen, and Y. Mano, 2010: Backscattering linear depolarization ratio measurements of mineral, sea-salt, and ammonium sulfate particles simulated in a laboratory chamber. *Appl. Opt.*, **49 (23)**, 4441, doi:10.1364/ao.49.004441.

Sakai, T., N. Orikasa, T. Nagai, M. Murakami, T. Tajiri, A. Saito, K. Yamashita, and A. Hashimoto, 2014: Balloon-borne and Raman lidar observations of Asian dust and cirrus cloud properties over Tsukuba, Japan. *J. Geophys. Res.-Atmos.*, **119 (6)**, 3295–3308, doi:10.1002/2013jd020987.

Sassen, K., 2005: *Lidar: Range-Resolved Optical Remote Sensing of the Atmosphere*. Springer, New York, 19-42 pp., doi:10.1007/b106786.

Schepanski, K., I. Tegen, M. C. Todd, B. Heinold, G. Bönisch, B. Laurent, and A. Macke, 2009: Meteorological processes forcing Saharan dust emission inferred from MSG-SEVIRI observations of subdaily dust source activation and numerical models. *J. Geophys. Res.*, **114 (D10)**, doi: 10.1029/2008jd010325.

Schillinger, M., D. Morancais, F. Fabre, and A. J. Culoma, 2003: ALADIN: the lidar instrument for the AEOLUS mission. *Sensors, Systems, and Next-Generation Satellites VI*, H. Fujisada, J. B. Lurie, M. L. Aten, and K. Weber, Eds., SPIE, doi:10.1117/12.463024.

Seifert, P., and Coauthors, 2010: Saharan dust and heterogeneous ice formation: Eleven years of cloud observations at a central european EARLINET site. *J. Geophys. Res.*, **115 (D20)**, doi: 10.1029/2009jd013222.

Shao, Y., and Coauthors, 2011: Dust cycle: an emerging core theme in Earth system science. *Aeolian Res.*, **2 (4)**, 181–204, doi:10.1016/j.aeolia.2011.02.001.

Siebert, H., and Coauthors, 2013: The fine-scale structure of the trade wind cumuli over Barbados - an introduction to the CARRIBA project. *Atmos. Chem. Phys*, **13 (19)**, 10 061–10 077, doi: 10.5194/acp-13-10061-2013.

Sorjamaa, R., and A. Laaksonen, 2007: The effect of water adsorption on cloud drop activation of insoluble particles: a theoretical framework. *Atmos. Chem. Phys.*, **7 (24)**, 6175–6180, doi: 10.5194/acp-7-6175-2007.

Stamnes, K., S.-C. Tsay, W. Wiscombe, and K. Jayaweera, 1988: Numerically stable algorithm for discrete-ordinate-method radiative transfer in multiple scattering and emitting layered media. *Appl. Opt.*, **27 (12)**, 2502, doi:10.1364/ao.27.002502.

Stein, A. F., R. R. Draxler, G. D. Rolph, B. J. B. Stunder, M. D. Cohen, and F. Ngan, 2015: NOAA's HYSPLIT atmospheric transport and dispersion modeling system. *B. Am. Meteorol. Soc.*, **96 (12)**, 2059–2077, doi:10.1175/BAMS-D-14-00110.1.

Stevens, B., H. Brogniez, C. Kiemle, J.-L. Lacour, C. Crevoisier, and J. Kiliani, 2017: Structure and dynamical influence of water vapor in the lower tropical troposphere. *Surv. Geophys.*, **38 (6)**, 1371–1397, doi:10.1007/s10712-017-9420-8.

Stevens, B., and Coauthors, 2019: A high-altitude long-range aircraft configured as a cloud observatory - the NARVAL expeditions. *B. Am. Meteorol. Soc.*, **100 (6)**, 1061–1077, doi: 10.1175/bams-d-18-0198.1.

Synge, E., 1930: A method of investigating the higher atmosphere. *The London, Edinburgh, and Dublin Philosophical Magazine and Journal of Science*, **9 (60)**, 1014–1020, doi:10.1080/14786443008565070.

Tegen, I., P. Hollrig, M. Chin, I. Fung, D. Jacob, and J. Penner, 1997: Contribution of different aerosol species to the global aerosol extinction optical thickness: estimates from model results. *J. Geophys. Res.-Atmos*, **102 (D20)**, 23 895–23 915, doi:10.1029/97jd01864.

Tesche, M., A. Ansmann, D. Müller, D. Althausen, R. Engelmann, V. Freudenthaler, and S. Groß, 2009a: Vertically resolved separation of dust and smoke over Cape Verde using multiwavelength Raman and polarization lidars during Saharan Mineral Dust Experiment 2008. *J. Geophys. Res.*, **114 (D13)**, doi:10.1029/2009jd011862.

Tesche, M., and Coauthors, 2009b: Vertical profiling of Saharan dust with Raman lidars and airborne HSRL in southern Morocco during SAMUM. *Tellus B*, **61 (1)**, 144–164, doi:10.1111/j.1600-0889.2008.00390.x.

Textor, C., and Coauthors, 2006: Analysis and quantification of the diversities of aerosol life cycles within AeroCom. *Atmos. Chem. Phys.*, **6 (7)**, 1777–1813, doi:10.5194/acp-6-1777-2006.

Toledano, C., and Coauthors, 2019: Sun photometer retrievals of Saharan dust properties over Barbados during SALTRACE. *Atmos. Chem. Phys.*, **19 (23)**, 14 571–14 583, doi:10.5194/acp-19-14571-2019.

Tsamalis, C., A. Chédin, J. Pelon, and V. Capelle, 2013: The seasonal vertical distribution of the Saharan air layer and its modulation by the wind. *Atmos. Chem. Phys.*, **13 (22)**, 11 235–11 257, doi:10.5194/acp-13-11235-2013.

Turner, J., 1973: *Buoyancy effects in fluids*. University Press, Cambridge England.

Tuve, M. A., E. A. Johnson, and O. R. Wulf, 1935: A new experimental method for study of the upper atmosphere. *Terr. Magn. Atmos. Electr.*, **40 (4)**, 452–454, doi:10.1029/TE040i004p00452.

Twohy, C. H., and Coauthors, 2017: Saharan dust, convective lofting, aerosol enhancement zones, and potential impacts on ice nucleation in the tropical upper troposphere. *J. Geophys. Res.-Atmos.*, **122 (16)**, 8833–8851, doi:10.1002/2017jd026933.

Twomey, S., 1974: Pollution and the planetary albedo. *Atmos. Environ. (1967)*, **8 (12)**, 1251–1256, doi:10.1016/0004-6981(74)90004-3.

Twomey, S., 1977: The influence of pollution on the shortwave albedo of clouds. *J. Atmos. Sci.*, **34 (7)**, 1149–1152, doi:10.1175/1520-0469(1977)034⟨1149:tiopot⟩2.0.co;2.

Villanueva, D., B. Heinold, P. Seifert, H. Deneke, M. Radenz, and I. Tegen, 2020: The day-to-day co-variability between mineral dust and cloud glaciation: a proxy for heterogeneous freezing. *Atmos. Chem. Phys.*, **20 (4)**, 2177–2199, doi:10.5194/acp-20-2177-2020.

Walser, A., 2017: On the Saharan air layer aerosol and its role as a reservoir of cloud condensation nuclei. Ph.D. thesis, Ludwig-Maximilians-Universität München.

Waterman, P. C., 1971: Symmetry, unitarity, and geometry in electromagnetic scattering. *Phys. Rev. D*, **3**, 825–839, doi:10.1103/PhysRevD.3.825.

Weinzierl, B., and Coauthors, 2017: The Saharan Aerosol Long-Range Transport and Aerosol-Cloud-interaction experiment: overview and selected highlights. *B. Am. Meteorol. Soc.*, **98 (7)**, 1427–1451, doi:10.1175/BAMS-D-15-00142.1.

Wendisch, M., D. Müller, D. Schell, and J. Heintzenberg, 2001: An airborne spectral albedometer with active horizontal stabilization. *J. Atmos. Ocean. Tech.*, **18 (11)**, 1856–1866, doi:10.1175/1520-0426(2001)018⟨1856:aasawa⟩2.0.co;2.

Wiegner, M., S. Groß, V. Freudenthaler, F. Schnell, and J. Gasteiger, 2011: The May/June 2008 Saharan dust event over Munich: Intensive aerosol parameters from lidar measurements. *J. Geophys. Res.-Atmos.*, **116 (D23)**, doi:10.1029/2011jd016619.

Wiegner, M., and Coauthors, 2009: Numerical simulations of optical properties of Saharan dust aerosols with emphasis on lidar applications. *Tellus B*, **61 (1)**, 180–194, doi:10.1111/j.1600-0889.2008.00381.x.

Winker, D. M., and Coauthors, 2010: The CALIPSO mission: A global 3D view of aerosols and clouds. *Bull. Am. Meteor. Soc.*, **91 (9)**, 1211–1229, doi:10.1175/2010BAMS3009.1.

Wirth, M., A. Fix, P. Mahnke, H. Schwarzer, F. Schrandt, and G. Ehret, 2009: The airborne multi-wavelength water vapor differential absorption lidar WALES: system design and performance. *Appl. Phys. B*, **96 (1)**, 201–213, doi:10.1007/s00340-009-3365-7.

Wong, S., and A. E. Dessler, 2005: Suppression of deep convection over the tropical North Atlantic by the Saharan air layer. *Geophys. Res. Lett.*, **32 (9)**, doi:10.1029/2004gl022295.

Wong, S., A. E. Dessler, N. M. Mahowald, P. Yang, and Q. Feng, 2009: Maintenance of lower tropospheric temperature inversion in the Saharan air layer by dust and dry anomaly. *J. Clim.*, **22 (19)**, 5149–5162, doi:10.1175/2009jcli2847.1.

Woodward, S., D. L. Roberts, and R. A. Betts, 2005: A simulation of the effect of climate change-induced desertification on mineral dust aerosol. *Geophys. Res. Lett.*, **32 (18)**, doi:10.1029/2005gl023482.

Yi, B., C. N. Hsu, P. Yang, and S.-C. Tsay, 2011: Radiative transfer simulation of dust-like aerosols: uncertainties from particle shape and refractive index. *J. Aerosol Sci.*, **42 (10)**, 631–644, doi:10.1016/j.jaerosci.2011.06.008.

Yu, H., and Coauthors, 2015: The fertilizing role of African dust in the Amazon rainforest: A first multiyear assessment based on data from Cloud-Aerosol Lidar and Infrared Pathfinder Satellite Observations. *Geophys. Res. Lett.*, **42 (6)**, 1984–1991, doi:10.1002/2015gl063040.

Zhao, T. L., S. L. Gong, X. Y. Zhang, A. Abdel-Mawgoud, and Y. P. Shao, 2006: An assessment of dust emission schemes in modeling east Asian dust storms. *J. Geophys. Res.*, **111 (D5)**, doi:10.1029/2004jd005746.

Zhu, A., V. Ramanathan, F. Li, and D. Kim, 2007: Dust plumes over the Pacific, Indian, and Atlantic oceans: climatology and radiative impact. *J. Geophys. Res.*, **112 (D16)**, doi:10.1029/2007jd008427.